PRECISE POINT POSITIONING AUGMENTATION FOR VARIOUS GRADES OF GLOBAL NAVIGATION SATELLITE SYSTEM HARDWARE

JOHN AGGREY

A DISSERTATION SUBMITTED TO THE FACULTY OF GRADUATE STUDIES
IN PARTIAL FULFILLMENT OF THE REQUIREMENTS FOR THE DEGREE OF
DOCTOR OF PHILOSOPHY

GRADUATE PROGRAM IN EARTH AND SPACE SCIENCE AND ENGINEERING
YORK UNIVERSITY
TORONTO, ONTARIO

OCTOBER 2019

ABSTRACT

The next generation of low-cost, dual-frequency, multi-constellation GNSS receivers, boards, chips and antennas are now quickly entering the market, offering to disrupt portions of the precise GNSS positioning industry with much lower cost hardware and promising to provide precise positioning to a wide range of consumers. The presented work provides a timely, novel and thorough investigation into the positioning performance promise. A systematic and rigorous set of experiments has been carried-out, collecting measurements from a wide array of low-cost, dual-frequency, multi-constellation GNSS boards, chips and antennas introduced in late 2018 and early 2019. These sensors range from dual-frequency, multi-constellation chips in smartphones to stand-alone chips and boards. In order to be comprehensive and realistic, these experiments were conducted in a number of static and kinematic benign, typical, suburban and urban environments.

In terms of processing raw measurements from these sensors, the Precise Point Positioning (PPP) GNSS measurement processing mode was used. PPP has become the defacto GNSS positioning and navigation technique for scientific and engineering applications that require dm- to cm-level positioning in remote areas with few obstructions and provides for very efficient worldwide, wide-array augmentation corrections. To enhance solution accuracy, novel contributions were made through atmospheric constraints and the use

of dual- and triple-frequency measurements to significantly reduce PPP convergence period. Applying PPP correction augmentations to smartphones and recently released low-cost equipment, novel analyses were made with significantly improved solution accuracy.

Significant customization to the York-PPP GNSS measurement processing engine was necessary, especially in the quality control and residual analysis functions, in order to successfully process these datasets. Results for new smartphone sensors show positioning performance is typically at the few dm-level with a convergence period of approximately 40 minutes, which is 1 to 2 orders of magnitude better than standard point positioning. The GNSS chips and boards combined with higher-quality antennas produce positioning performance approaching geodetic quality. Under ideal conditions, carrier-phase ambiguities are resolvable. The results presented show a novel perspective and are very promising for the use of PPP (as well as RTK) in next-generation GNSS sensors for various application in smartphones, autonomous vehicles, Internet of things (IoT), etc.

DEDICATION

To Mom, Dad, Prissy, Annabelle, Maame, Kofi, Shonni and Ewurabena.

ACKNOWLEDGEMENTS

Flight number EK 0241 is probably the most important and memorable flight in my life. It was the trip that spearheaded my journey into GNSS navigation. From the scorching heat of Ghana to the rich diversity of Toronto, it has been truly a life changing experience. Without a doubt, my research work would not have been possible without the opportunity offered to me by Dr. Sunil Bisnath. I am especially indebted to him for being supportive of my career goals and working actively to provide me with all the avenues to pursue those goals. As my supervisor and mentor, he has taught me more than I could ever give him credit for here. He has shown me, by his example, what a good scientist (and person) should be.

I am really grateful to all of those with whom I have had the pleasure to work with during this and other related projects. Each of the members of my Dissertation Committee has provided me with extensive professional guidance and taught me a great deal about scientific research. I would especially like to thank Dr. Spiros Pagiatakis and Dr. Jian-Guo Wang for all the insightful guidance towards the successful execution of my research. My sincere thanks also go to my Dissertation committee. Dr. Suelynn Choy, Dr. Kevin Gingerich and Dr. Ryan Orszulik provided insightful comments, encouragement and of course, the hard questions, that made my defence a memorable and fun one.

My family away from home have been my colleagues with whom I shared wonderful experiences and stressful times together. From all the group lunches to late night work to beat deadlines, it has been awesome to work with my colleagues who have become more than friends. Thanks to Garrett Seepersad, Maninder Gill, Sudha Vana, Nacer Naciri, Junchan Lee, Surabhi Guruprasad, Siddharth Dave, Ganga Shinghal, Ding Yi, Sihan Yang Narin Gavili Kilane and John Bagshaw. Special thanks to Garrett for being a brother and awesome in all aspects of my research. His contributions, both personally and research-wise, have been invaluable.

Nobody has been more important to me in the pursuit of this degree than the members of my family. I would like to thank my parents; whose love and guidance are with me in whatever I pursue. They are the ultimate role models. Most importantly, I wish to thank my loving and supportive wife, Priscilla, and my daughter Annabelle who is just about to graduate from furniture walking.

This PhD journey has been an amazing experience. I would like to thank everyone, including all those I may have missed here, for all the support and kindness shown to me.

TABLE OF CONTENTS

LIST OF TABLES

LIST OF FIGURES

LIST OF ACRONYMS

AC	Analysis Centers
AR	Ambiguity Resolution
ANTEX	Antenna Exchange Format
ASPRS	American Society for Photogrammetry and Remote sensing
C/A code	Coarse/Acquisition code
C/N_0	Carrier-to-noise-density ratio
CDMA	Code Division Multiple Access
CSAC	Chip Scale Atomic Clock
BeiDou	China's satellite system
CSRS-PPP	Canadian Spatial Reference System-Precise Point Positioning
DCB	Differential Code Bias
DOY	Day of year
ECEF	Earth-Centred, Earth-Fixed
FCB	Fractional Code Bias
FDMA	Frequency Division Multiple Access
FOC	Full Operational Capability
Galileo	European satellite navigation system
GLONASS	Russian satellite navigation system
GNSS	Global Navigation Satellite System
GPS	Global Positioning System
GPST	GPS Time
GREC	GPS (G), GLONASS (R), Galileo (E), BeiDou (C)
ICB	Inter-frequency Channel Bias
IGS	International GNSS Service
IHO	International Hydrographic Organization
IMU	Inertial Measurement Unit
INS	Inertial Navigation System
IRC	Integer Recovery Clocks
ITRF	International Terrestrial Reference Frame
MEMS	Microelectromechanical systems
N, E, U	North, East and Up components
NRCan	Natural Resources of Canada
NRTK	Network RTK

ppm	parts per million
PPP	Precise Point Positioning
PPP-AR	Precise Point Positioning Ambiguity Resolution
PPP-ICAR	Precise Point Positioning Ionospheric Constrained Ambiguity Resolution
PPP-RTK	PPP and Real-Time Kinematic integration
RF	Radio frequency
RFID	Radio-frequency Identification
RHCP	Right Hand Circularly Polarized
RINEX	Receiver INdependent EXchange
rms	root mean square
RTK	Real-Time Kinematic
SNR	Signal-to-noise Ratio
ZPD	Zenith path delay

CHAPTER 1 INTRODUCTION TO MULTI-GNSS AND MULTI-FREQUENCY PRECISE POINT POSITIONING

The inception of navigation dates back to the very early days of mankind. The early exploration of new territories prompted the need to locate and ascertain one's location and destination. Memorizing landscapes and landmarks was necessary for survival. Maritime transportation fuelled the necessity for accurate positioning as there was a loss of directional sense on the high seas. The lack of terrestrial marks and poor visibility made for dire consequences in the event of a disaster or loss of way. This positioning need led to the genesis of positioning techniques. The story of positioning has a strong correlation with the history of instrument development. Before the discovery of radio conduction, the innate desire to communicate over very long distances was already envisioned by the fifth century. However, the launch of Sputnik (Dickson 2001), by the then Soviet Union, was the starting point for satellite navigation systems. Transit (Stansell 1978) and Tsyklon (Li 1996) systems, deployed by United States and Soviet Union, respectively, soon followed. These first-generation systems were based on Doppler shift measurements which would require a very high number of launched satellites to provide users with 365-day and 24-hour reliable coverage for three-dimensional positioning. Though it was possible and feasible to attain, the alternative of using time-based measurements was sought as the solution to increase terrestrial average and increase positional accuracy. The use of atomic clocks on satellites produced the second

generation of the satellite navigation system. Multiple constellations of satellites currently exist, each classified as a Global Navigation Satellite System (GNSS) and transmitting time-based measurements. Four GNSSs are currently either nearing full operational capability (FOC) or in FOC status – Global Positioning System (GPS) (USA) (U.S. Coast Guard Navigation Center 2015; GPS.gov 2017; NASA 2017), Globalnaya Navigazionnaya Sputnikovaya Sistema (GLONASS) (Russian Federation) (Eissfeller et al. 2007; Urlichich et al. 2010, 2011; Federal Space Agency 2015), Galileo (European Union) (Hein 2005; European GNSS Agency 2015, 2017; European Space Agency 2015) and BeiDou (People's Republic of China) (China Satellite Navigation Office 2012; IGS 2017; CSNO TARC 2018). Currently, there are three Regional Navigation Satellite Systems (RNSS) which are localized over specific regions of the earth: Indian Regional Navigation Satellite System (IRNSS, also called NavIC) (Department of Space 2011; Nadarajah et al. 2015; Indian Space Research Organization 2017), Japanese Quasi-Zenith Satellite System (QZSS) (Seynat et al. 2004; Inaba 2009; Ishijima et al. 2009; Murai 2014) and phase 2 of BeiDou (Montenbruck et al. 2012; Sun et al. 2012). These RNSSs are complimentary to GNSS and further increase the number of satellites in their intended coverage regions.

1.1 The evolution of GNSS infrastructure

The facilitation, interoperability and compatibility among all available satellite navigation systems is a key concern that requires a level of coordination among governments and agencies. The aim of such collaboration is to protect and promote open service

applications which will be beneficial to general communities. This coordination has led to a level of standardization in the adoption of current and modernized GNSS signals with compatible frequency band and modulation plans. The resultant goal is to facilitate a commonality in the design of multi-GNSS receiver chipsets and antennas for end users. Presented in Figure 1.1 are the operational GNSS and IRNSS healthy satellites in orbit.

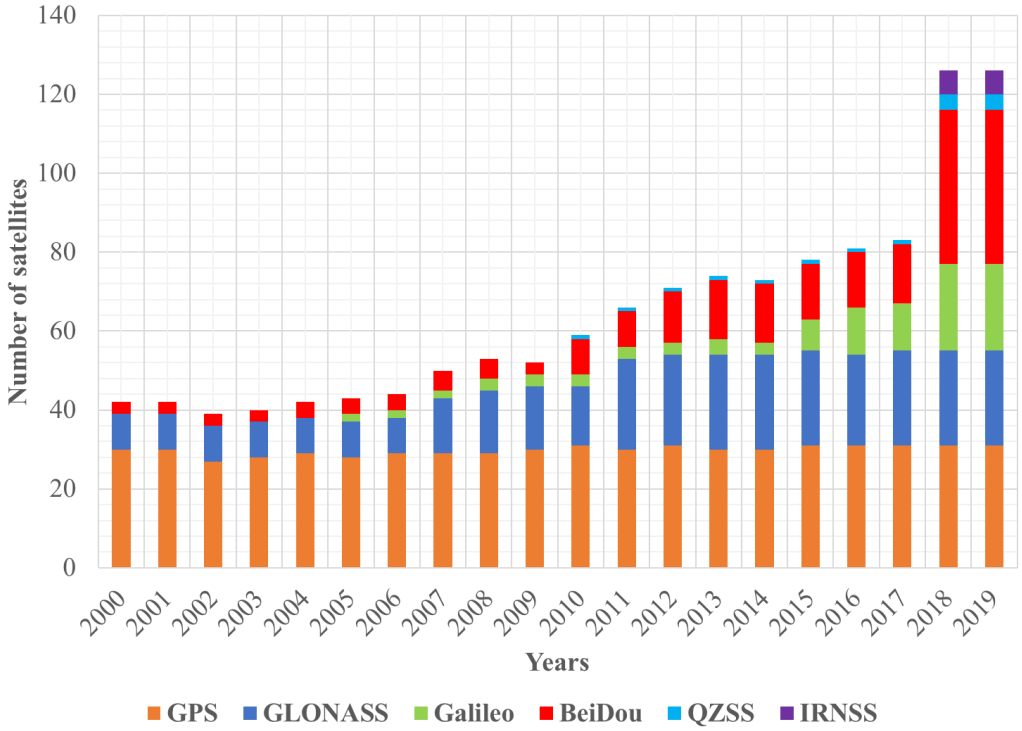

Figure 1.1: Operational GNSS and RNSS satellites. Number of satellites presented excludes those which are under commissioning, testing and failed launches (European GNSS Supervisory Authority 2017; European Space Agency 2019; Zak 2019; National Coordination Office for Space-Based Positioning, Navigation, and Timing 2019).

It is interesting to observe the increasing number of GNSS satellites over the past two decades. Such proliferation promises reliability, integrity and enhanced accuracy levels for positioning irrespective of the technique.

Between 2018 and 2019, there was a significant 30% increase in the number of satellites, primarily due to Galileo, BeiDou and QZSS launches. The extensive use of GNSS in most current location-based applications worldwide has deepened the resolve of participating governments to improve and modernize constellations towards the common goal of interoperability. Specific services are intended to be provided through dedicated signals for the global community. For instance, a level of restricted access to governmental services is intended to be made available to the public. Such services include Galileo Public Regulated Service (PRS) or GPS Standard Positioning Service (SPS). Other services which may be provided for free or for a fee include Galileo High-Accuracy Service (HAS), QZSS L6 and BeiDou short messaging service (Wang et al. 2015; Fernandez-Hernandez et al. 2018; Cabinet Office, Government Of Japan 2019a).

The current GNSS infrastructure is constantly changing. By 2020, BeiDou and Galileo are planning on reaching FOC, while GPS and GLONASS continue to engage in various modernization schemes for enhanced performance. For instance, the U.S. has deployed new satellites, GPS III, since the beginning of 2018 with the L1C signal which is identical to Galileo's EI signal feature (Cameron 2019; Crews and Betz 2019). In addition to that, the L1 legacy signal as well as the L2C and L5 will also be broadcasted resulting in the worldwide

availability of four GPS signals. The transmission and usage of L2C is meant to replace the codeless and semi-codeless GPS access by 2020. These codeless and semi-codeless signals were intended for receivers to track without the need of encryption keys for the pseudorandom generation and modulation of the replica signals (Hein 2017).

GLONASS launched the first generation of GLONASS-K satellite on 26th February 2011. The satellites transmit Code-Division Multiple Access (CDMA) signals instead of the Frequency Division Multiple Access (FDMA) technique which had been used to previously design GLONASS signal transmission. It is planned that the next generation of satellites will be based on the GLONASS KM and K2 satellite prototype intended for launch after 2020. These satellites will feature Orbit Determination and Time Synchronization (ODTS) technologies, as well as improvement in clock stability (Urlichich et al. 2011; Federal Space Agency 2015).

To provide a global service by 2020, a third generation BeiDou satellite system (BeiDou-phase 3) is currently being planned for launch with the aim of obtaining a 35-satellite constellation. It is expected that the completed and final system will transmit signals at the B1, B2 and B3 frequencies. These frequencies are similar to the E1/L1, E5/L5 and E6 frequencies of Galileo and GPS, respectively. The purpose of sharing close frequency bands and waveforms with GPS and Galileo is to maintain interoperability among the GNSSs. With the inclusion of regional BeiDou phases of operational satellites, the global constellation of BeiDou would be the largest to exist. Two main services will be provided only by the regional

system: Short Message Service (SMS) and Wide Area Differential Service (Liu 2013; China National Administration of GNSS and Applications 2019).

Galileo aims to reach FOC by 2020 and thus continues the deployment of satellites to realize its goal. By August of 2018, the Galileo constellation included 26 orbiting satellites with 17 being fully operational. Being the first GNSS constellation featuring a Search and Rescue (SAR) service with a return link for users in distress, Galileo additionally provides services based on the E1/E5 bands. The provision of Navigation Message Authentication (NMA), an encrypted navigation signal on E6 and Signal Authentication Service (SAS) are also among the unique capabilities offered to end users. The functionalities of NMA and SAS are intended to provide the first protection level against the spoofing of GNSS users (Fernández-Hernández et al. 2016; European Space Agency 2019).

QZSS is currently a 4-satellite constellation consisting of three Inclined Geosynchronous Orbit (IGSO) satellites and one geostationary (GEO) satellite. The purpose of its infrastructure is to provide visibility constantly from all the Asia-Oceanic regions. By 2023, it is planned that QZSS will have a 7-satellite constellation augmenting GPS coverage over Japan's urban canyons as well as enhancing performance, accuracy and reliability. QZSS is anticipated to provide a host of services to the public end user including exploitations of QZSS data links (for instance, Satellite Report for Disaster and Crisis Management), Centimetre Level Augmentation Service (CLAS), Sub-metre Level Augmentation Service

(SLAS), a future Public Regulated Service and an SBAS Transmission Service (GPS World Staff 2018; Cabinet Office, Government Of Japan 2019a, b).

The successful launch of NavIC-1L on April 12, 2018 spearheaded India's goal of having a 7-satellite operational constellation. The coverage of NavIC extends 1500 km around India and aims to extend the number of satellites from seven to eleven to expand the coverage regions. It transmits on the L5 (1176.45 MHz) and S band (2492.028 MHz) frequencies and currently offers a Standard Positioning Service and a Precision Service (Indian Space Research Organization 2017; Ma et al. 2019).

1.2 Overview of PPP

Precise Point Positioning (PPP) is an augmented point positioning approach that uses un-differenced, dual-frequency pseudorange and carrier-phase observations along with precise satellite orbit and clock products to produce decimetre- to sub-centimetre-level positioning (Zumberge et al. 1997; Héroux et al. 2004). Positioning techniques such as relative GPS positioning, Real-Time Kinematic (RTK) and Network RTK require the use of more than one receiver. In contrast, PPP, is a cost-effective technique, requires a single user GNSS receiver with no additional local GNSS infrastructure. Static and kinematic data processing can be done using the PPP technique either in post-processing or real-time mode (Kouba and Héroux 2001; Chen and Gao 2005; Leandro 2009).

In conventional PPP, the combination of satellite positions and clocks errors to obtain a few centimetres of accuracy with ionospheric-free (ionospheric effect has been mitigated) pseudorange and carrier-phase observations, requires the accounting of some error effects that are not considered in Standard Positioning Service (SPS). The GPS SPS is a positioning and timing service provided by way of ranging signals broadcasted on the GPS L1 frequency. The L1 frequency, transmitted by all satellites, contains a coarse/acquisition (C/A) code ranging signal, with a navigation data message, that is available for civil, commercial, and scientific use (US DoD 2001). Figure 1.2 compares the approaches of SPS and PPP. SPS requires metre-level, real-time satellite orbit and clock information from GNSS satellites. Ionospheric refraction error is mitigated through ionosphere-free linear combinations (Odijk 2003). However, single-frequency users adopt various models to account for the ionospheric error (Klobuchar 1987, 1996; Shi et al. 2012). The troposphere is accounted for by using mapping function and models for wet and dry troposphere (e.g., Collins 1999). Through epoch-wise least squares estimation, all of this information is combined with C/A-code pseudorange measurements to produce metre-level user position estimates (Bisnath and Collins 2012). PPP utilizes the same receiver tracking information in SPS but combines it with centimetre-level precise orbit and clock information and additional error modelling and filtering to obtain decimetre- to millimetre-level user position estimates.

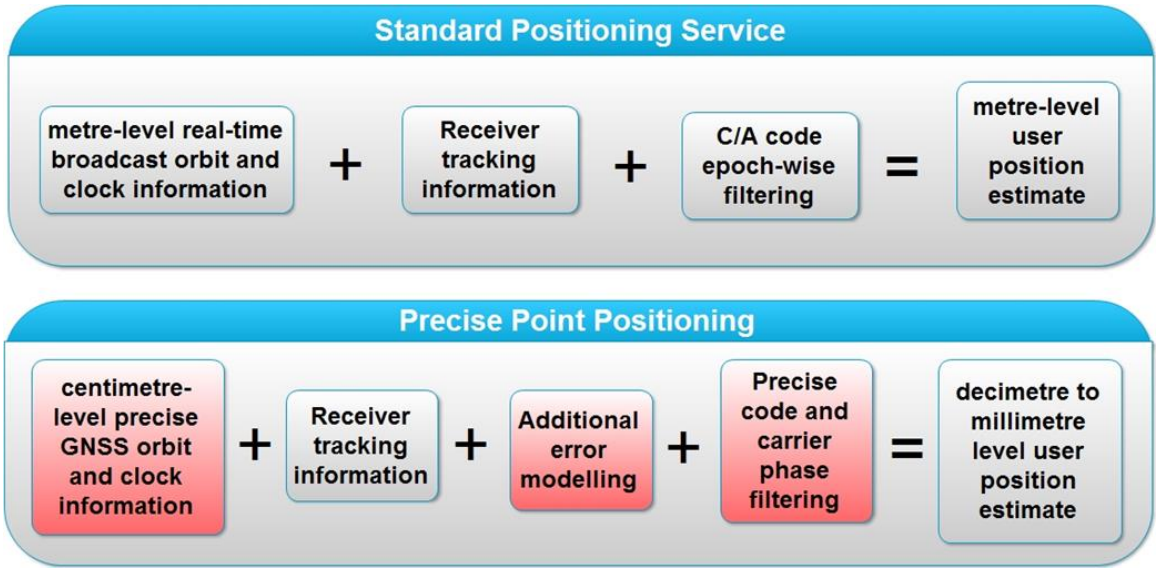

Figure 1.2: SPS in comparison to PPP (Aggrey 2015)

Given that all relevant PPP errors have either been modelled or estimated, the conventional un-differenced observation equations can be written as (Wells et al. 1999):

$$P_{L_i}^{GNSS} = \rho^i + c(\partial t^s - \partial t_r) + d_{trop} + d_{ion,L_i} + b_{Pr_i}^{L_i} + b_P^{L_i,s_j} + d_{multi\left(P_{L_i}\right)} + \varepsilon\left(P_{L_i}^{GNSS}\right) \quad 1.1$$

$$\Phi_{L_i}^{GNSS} = \rho^i + c(\partial t^s - \partial t_r) + d_{trop} - d_{ion,L_i} + b_{\Phi r_i}^{L_i} + b_\Phi^{L_i,s_j} + \lambda_{L_i}, N_{L_i} + d_{multi\left(\Phi_{L_i}\right)} + \varepsilon\left(\Phi_{L_i}^{GNSS}\right) \quad 1.2$$

The terms in equation 1.1 and 1.2 are:

$P_{L_i}^{GNSS}$ Pseudorange measurement on L1 or L2 (m)

$\Phi_{L_i}^{GNSS}$	Carrier-phase measurement on L1 or L2 (m)
ρ^i	Geometric range (m)
c	Speed of light (m/s^{-1})
∂t^s	Satellite clock error (sec)
∂t_r	Receiver clock offset (sec)
d_{ion,L_i}	Ionospheric delay (m)
d_{trop}	Tropospheric delay (m)
$b_{Pr_i}^{L_i}, b_{\Phi r_i}^{L_i}$	Receiver equipment bias for pseudorange and carrier-phase measurements, respectively (m)
λ_{L_i}	Wavelength of L1 or L2 carrier waves (m)
N_{L_i}	Unknown cycle ambiguity term on L1 or L2 carrier-phases (cycles)
$d_{multi\left(\Phi_{L_i}\right)}$	Carrier-phase multipath on L1 or L2 (m)
$d_{multi\left(P_{L_i}\right)}$	Pseudorange multipath (m)
$\varepsilon\left(P_{L_i}^{GNSS}\right)$	Pseudorange measurement noise (m)
$\varepsilon\left(\Phi_{L_i}^{GNSS}\right)$	Carrier-phase measurement noise (m)

By linearizing equations 1.1 and 1.2 through the relation of the unknown quantities and the observations, equation 1.3 is obtained:

$$A\delta + W - V = 0 \qquad 1.3$$

Where

A	Design matrix
δ	Estimated corrections to unknown quantities
W	Pre-fit misclosure vector
V	Residual vector

The design matrix (A) is the partial derivatives of the observation equations with respect to the unknown parameters (x) which primarily are the receiver station 3D position (X, Y, Z), receiver clock offset (∂t_r), tropospheric zenith path delay (zpd), carrier-phase ambiguities and hardware biases. The design matrix is given as follows:

$$A = \begin{bmatrix} \frac{\partial \rho_i^{j=1}(t)}{\partial X_i^j} & \frac{\partial \rho_i^{j=1}(t)}{\partial Y_i^j} & \frac{\partial \rho_i^{j=1}(t)}{\partial Z_i^j} & \frac{\partial \rho_i^{j=1}(t)}{\partial t_i} & \frac{\partial \rho_i^{j=1}(t)}{\partial zpd} & 0 & 0 \ldots & 0 \\ \frac{\partial \Phi_i^{j=1}(t)}{\partial X_i^j} & \frac{\partial \Phi_i^{j=1}(t)}{\partial Y_i^j} & \frac{\partial \Phi_i^{j=1}(t)}{\partial Z_i^j} & \frac{\partial \Phi_i^{j=1}(t)}{\partial t_i} & \frac{\partial \Phi_i^{j=1}(t)}{\partial zpd} & \frac{\partial \Phi_i^{j=1}(t)}{\partial N_{if,1}} & 0 \ldots & 0 \\ \vdots & \vdots & \vdots & \vdots & \vdots & 0 & 0 \ldots & 0 \\ \frac{\partial \rho_i^{j=n}(t)}{\partial X_i^j} & \frac{\partial \rho_i^{j=n}(t)}{\partial Y_i^j} & \frac{\partial \rho_i^{j=n}(t)}{\partial Z_i^j} & \frac{\partial \rho_i^{j=n}(t)}{\partial t_i} & \frac{\partial \rho_i^{j=n}(t)}{\partial zpd} & 0 & 0 \ldots & 0 \\ \frac{\partial \Phi_i^{j=n}(t)}{\partial X_i^j} & \frac{\partial \Phi_i^{j=n}(t)}{\partial Y_i^j} & \frac{\partial \Phi_i^{j=n}(t)}{\partial Z_i^j} & \frac{\partial \Phi_i^{j=n}(t)}{\partial t_i} & \frac{\partial \Phi_i^{j=n}(t)}{\partial zpd} & 0 & 0 \ldots & \frac{\partial \Phi_i^{j=n}(t)}{\partial N_{if,n}} \end{bmatrix} \quad 1.4$$

The misclosure vector represents the differences between the pseudorange or carrier-phase observations and the computed pseudoranges and carrier-phases determined through the functional model. The misclosure vector elements are determined by the following equations:

$$W_{P_{L_{if}}} = P_{L_{if}} - \rho_i - c\partial t^s + c\partial t_r - T_{zpd} \quad 1.5$$

$$W_{\Phi_{L_{if}}} = \Phi_{L_{if}} - \rho_i - c\partial t^s + c\partial t_r - T_{zpd} - \lambda_{L_{if}} N_{L_{if}}^j \quad 1.6$$

$$W = \begin{bmatrix} W_{P_{L_{if}}}^{j=1} \\ W_{\Phi_{L_{if}}}^{j=1} \\ \vdots \\ W_{P_{L_{if}}}^{j=n} \\ W_{\Phi_{L_{if}}}^{j=n} \end{bmatrix} \quad 1.7$$

The weight matrix for stationary receivers is given as:

$$P_l = \begin{bmatrix} 1 & & & & \\ & 100^2 & & & \\ & & \ddots & & \\ & & & 1 & \\ & & & & 100^2 \end{bmatrix} \quad 1.8$$

The weight coefficient matrix with respect to the estimated parameters is given as:

$$P_x = C_x^{-1} \quad 1.9$$

where C_x is the a priori variance-covariance matrix.

$$X^T = \begin{bmatrix} x & y & z & dt & zpd & N_{j=1,nsat}^{j} \end{bmatrix} \quad 1.10$$

$$\Delta x = (A^T P_l A + P_x)^{-1} A^T P_l W \quad 1.11$$

$$\widehat{X} = x^o + \Delta x \quad 1.12$$

Given that the carrier-phase observations are about 100 times more precise than the pseudorange measurements, the weight matrix of the observations (P_l) is applied as shown in equation 2.8. Using the sequential least-squares approach weighted with a priori weighted constraints (P_x) of the state terms X^T, the unknown parameter estimates (Δx), as computed in equations 1.11 and 1.12. $\widehat{X}$ and x^o represents the corrected state terms and initial state terms, respectively, for a given epoch.

Precise positioning and navigation become an asset in remote areas where reference stations are not available. In recent years, Collins et al. (2008) determined the plausibility of using real-time PPP technique in the determination and monitoring of seismic activities by resolving PPP non-integer ambiguities. By assessing the performance of PPP, it is possible to

further extend to other scientific applications such as satellite clock error estimation, satellite pseudorange bias, pseudorange multipath estimation and ionospheric delay estimation (Leandro 2009). As more visible satellites and observations are made available by the advancement and modernization of various satellite constellations, a combined use of various satellite systems in PPP is expected to improve the positioning accuracy, reliability and solution convergence period.

1.3 Overview of York GNSS PPP software development

The York GNSS PPP software is a scalable and modular GNSS PPP processor written in C++ using Visual Studio in the Microsoft.NET platform. The usage of C++ in developing the GNSS PPP processor makes it not only platform-independent but also enhances re-usability. A total of over 60,000 lines of C++ code have been written by the York GNSS Laboratory, with 11 solution projects, over 100 classes, over 450 functions and over 8,000 lines of MATLAB code for the analysis and plotting of results (Seepersad 2012; Aggrey 2015). This overview section highlights the various development stages of the GNSS PPP software, detailed object-oriented architecture and the author's contribution to its development.

Figure 1.3 illustrates the software architecture of York GNSS PPP software. It consists of five main segments: data input, error correction, sequential least-squares module, parameter output and real-time modules. The user is required to specify processing parameters and input

files. All provided data are read and stored in internally defined structures before data-handling checks are performed. These data-handling checks constitute the data pre-processing module and involve making sure that all necessary satellite data are available, and that bad data are rejected. The correction module depends on user-required data supplied in the form of an observation file, precise satellite orbits and clocks, ANTEX file and ocean loading coefficients. The corrected observation data are passed through the sequential filtering module where position estimates as well as other parameters are obtained. The output parameter segment is intended for the purpose of evaluation and result analysis.

The author contributed significantly to the development of the YorkU PPP engine. Figure 1.4 highlights the collaborative and unique contributions made by the author to the architectural development of the software. These contributions have centred on improving the position performance of the software while taking advantage of available multi-frequency signals. A later objective was to focus more on low-cost chipsets in smartphones and current available mass-market low-cost receivers.

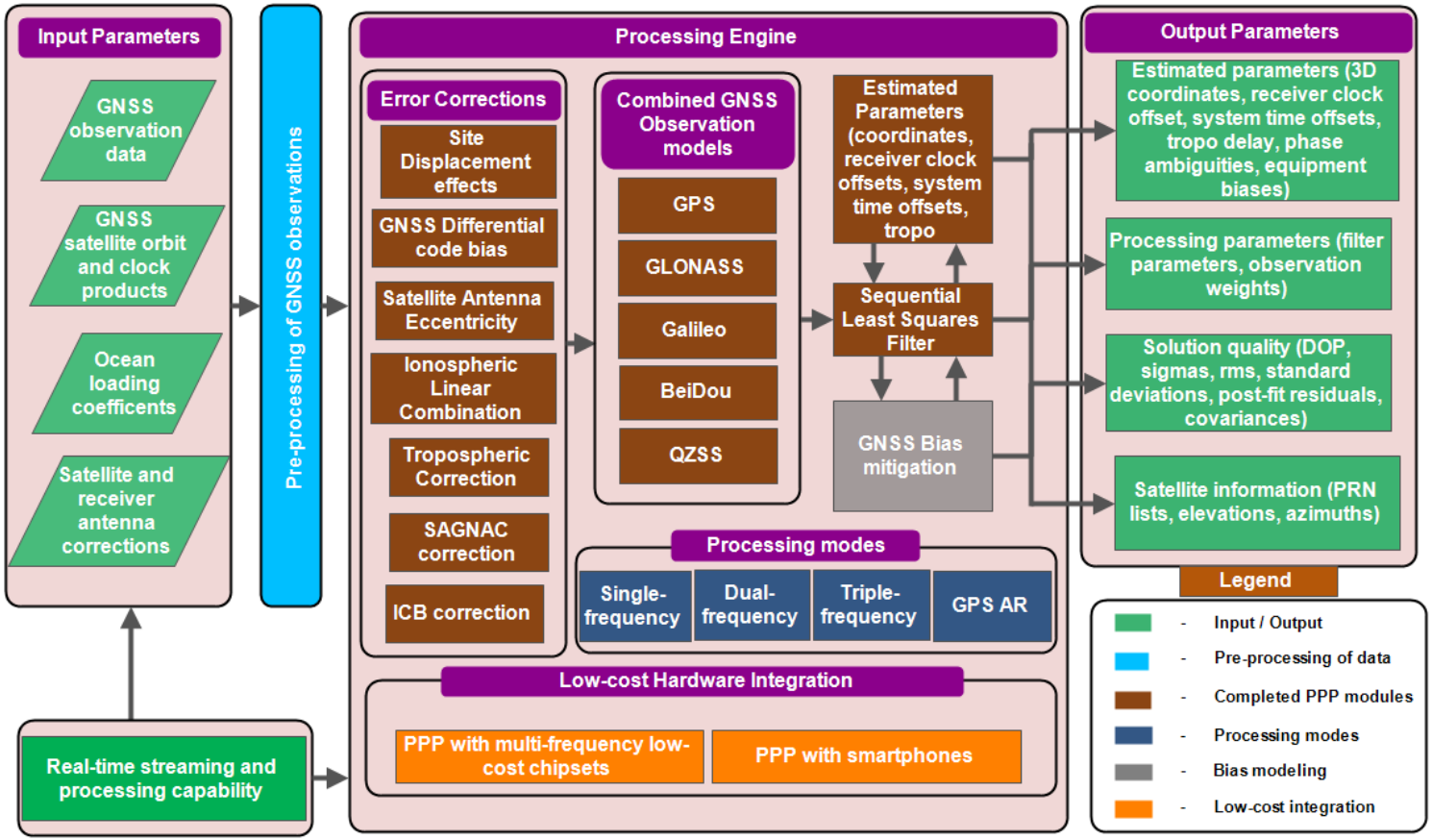

Figure 1.3: Current architecture of York GNSS PPP processing engine

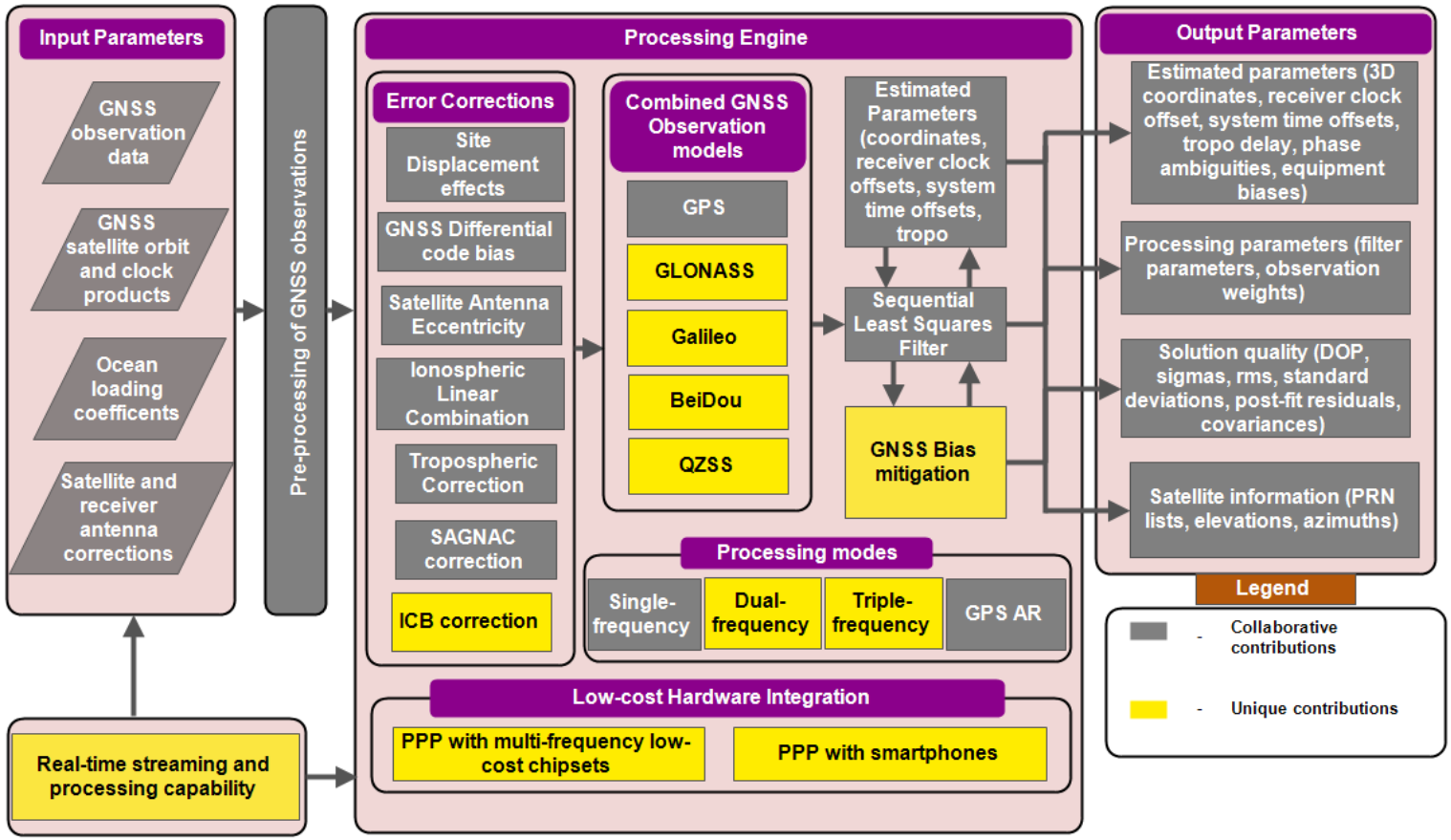

Figure 1.4: Collaborative and unique contributions of the author to the York GNSS PPP processing engine

The York GNSS PPP software currently supports post-processing and real-time streaming of GPS, GLONASS, Galileo, BeiDou and QZSS data. The fundamental unit of the software is a function, which contains program code to execute a specific task depending on user-defined inputs. A class of functions constitute a group of functions aimed towards a particular task. A cluster of classes of functions constitute a namespace. These namespaces are then managed through designed solution projects with the purpose of multi-threading which enhances memory management and real-time simulations. Structuring the software enhances scalability, modularization and processing speed of the software.

1.4 Problem statement

There is currently a demand for better positional accuracy with respect to low-cost hardware in various GNSS user markets. Prominent examples include the automotive market and cellular technology applications which currently require decimetre-level of accuracy or better, using mass-market hardware components. To address these needs, various components have been developed as part of this study to satisfy both geodetic-grade applications and low-cost hardware. Various error modelling and improvement in solution quality developed as part of this study are intended to improve the accuracy standards with the integration of PPP processing into low-cost equipment.

Problem 1: Dual-frequency PPP still remains impractical for many real-time applications due to a relatively long initial convergence period. The introduction of a fully operational third frequency promised faster convergence and almost instantaneous integer resolution of ambiguities. However, the expectation of triple-frequency PPP has, so far, not been met with reliable quick fixing of float carrier-phase ambiguities. The key research question intended to be answered include:

- *What are the challenges and methods available for quickly attaining accurate position initialization for float PPP solutions?*
- *How much do triple-frequency measurements help in the first few minutes of PPP convergence before the resolution of ambiguities?*

Problem 2: Another objective of this study is to analyze the performance of PPP convergence and initialization while stochastically constraining the atmosphere. One specific objective of this study is to review the performance of dual- and triple-frequency PPP solutions using uncombined measurements. The research question to be answered is whether there is any significant benefit in constraining the atmosphere, specifically the ionospheric parameter, in dual- and triple-frequency PPP processing? The goal of this study is to answer the question concerning the level of significance of any improvement noticed with atmospheric parameter estimation versus using a priori atmospheric knowledge. Some of the related questions intended to be answered include:

- *Is there any equivalence or differences between combined and uncombined PPP approaches for dual- and triple-frequency measurement processing?*
- *How comparable is atmospheric constrained uncombined multi-GNSS PPP to RTK performance?*
- *In terms of solution accuracy and convergence, currently how close is PPP to RTK performance?*

Problem 3: It has now become a standard approach to use the strength of the raw measurements through the uncombined PPP processing approach without the need for ionospheric-free linear combinations. One key benefit with this approach is gaining access to estimated slant ionospheric delays, which can be used as a priori information for constraining position solutions (Aggrey and Bisnath 2017a). As a follow-up to problem 2, it is well known that using a priori ionospheric information reduces PPP solution initial convergence period, whether such information is obtained from individual stations or from a global or regional network (Banville et al. 2014). However, there are key concerns about how effective these global or regional ionospheric products are. The third objective of this research contribution is to provide a detailed assessment of the available ionospheric products and how they affect PPP solution convergence and initialization. Some key questions which are intended to be addressed include:

- *Is there any equivalence or differences between combined and uncombined PPP approaches for dual- and triple-frequency measurement processing?*
- *Is atmospheric constrained, uncombined, multi-GNSS PPP nearly comparable to the RTK approach? In terms of solution accuracy and convergence, currently how far away are we from RTK performance?*

Though there has been a great deal of research into ionospheric modelling and its effect on navigation, there has not been detailed analysis in defining the impact on multi-GNSS PPP in light of modernized and current signals or processing modes. This research presents an in depth of analysis while, presenting answers to these important questions.

Problem 4: As the accuracy of float PPP without ambiguity resolution or atmospheric a priori information is independent of baseline lengths, improving its convergence and performance is necessary if it is to be considered as a good alternative to the RTK technique. Atmospheric constraining in PPP with the aim of improving the solution accuracy and quality needs to be addressed.

There is a level of progression which can be noticed from the age of dual-frequency multi-GNSS processing through the usage of triple-frequency measurements to the application of atmospheric constraints. Latitudinal correlation between atmospheric products and PPP accuracy will be addressed. The performance

of atmospheric-constrained PPP-AR solutions will also be investigated. Specifically, the following key questions are to be answered:

- *What is the magnitude of improvements observed from the usage of traditional dual-frequency measurements to triple-frequency PPP processing with atmospheric constraints?*
- *What are the inherent challenges when constraining PPP solutions with atmospheric corrections either functionally or stochastically?*
- *What is the significance of PPP-AR in multi-GNSS PPP atmospheric constrained solution?*
- *Finally, what are the key challenges left in obtaining near-instantaneous PPP convergence akin to RTK data processing?*

Problem 5: With the recent access to raw GNSS measurements on Android smartphone devices, it is necessary to investigate the role PPP can play in enhancing solution accuracy. All tested devices had the capability of tracking either three or four GNSS constellations. Two of the tested devices had a dual-frequency tracking capability. The key research questions to be answered are:

- *What is the typical positioning performance when using the raw measurements from smartphones in multi-GNSS PPP processing either in static or kinematic scenarios?*

- *Given the limitation that the hardware components of the smartphones present, what integrity measures can be implemented to enhance the usage of the raw measurements?*
- *What is the best performance that can be achieved with multi-GNSS PPP given normal usage of the smartphones by the user?*

Problem 6: The recent market releases of state-of-the-art low-cost receivers capable of tracking multi-GNSS signals offers a glimpse into the potential level of improvement in the user solution accuracy. However, there are key research questions that need to be addressed:

- *What is the performance of current low-cost receiver sensors?*
- *Given the quality of observations of relative low-cost sensors in contrast to geodetic grade receivers, what adaptive measurement weighting can be used to enhance the solution performance?*
- *Through multi-GNSS PPP processing, what performance metrics can the end user adopt as a guide when it comes to low-cost receiver applications?*

1.5 Novelty, contributions and significance of this dissertation

This research focuses on developing algorithms and models for the combined and uncombined observables of GNSS PPP satellite navigation constellations using dual- and triple-frequency, undifferenced code and carrier phase observations and assessing

the performance. This work contributes to the knowledge shared by other researchers, either in the academic or industrial fields of the GNSS community. These works from other researches will be contextually addressed in the subsequent chapters. The following goals are intended to be achieved:

1. Assessment of the performance of PPP from combining and uncombining data from multiple constellations with regards to the positional accuracy for both static and real-time applications.
2. Implementation of PPP models and algorithms in software development.
3. Estimation or modelling of GNSS equipment biases.
4. Reduction of convergence period.
5. Applying geodetic grade corrections to low-cost hardware through PPP processing.

In summary, the rationale for the research includes:

- Better PPP performance due to redundant measurements, improved geometry and more signals.
- Improvement in the estimation of float carrier-phase ambiguities for easier resolution to integer ambiguities.
- Better solution quality and enhancing PPP performance through the estimation and usage of ionospheric and tropospheric corrections.

- Integration of PPP processing with low-cost hardware to achieve decimetre-level accuracy.

1.6 Dissertation outline

Chapter 2 draws attention to the challenges and methods available for quickly attaining accurate position initialization for float PPP solutions, while analyzing the intricacies of issues that have to be dealt with in doing so. This chapter concentrates on the first few minutes of PPP convergence in dual- and triple-frequency scenarios to analyze and contribute to improvements of the float solution before the resolution of ambiguities.

Chapter 3 analyzes the performance of PPP convergence and initialization while stochastically constraining the atmosphere. One specific objective of this chapter is to review the performance of dual- and triple-frequency PPP solutions using uncombined measurements. The research question to be answered is whether there is any significant benefit in constraining the atmosphere, specifically the ionospheric parameter, in dual- and triple-frequency PPP processing?

Chapter 4 provides insight into the conceptual analyses of atmospheric GNSS PPP constraints with ambiguity resolution. Dual- and triple-frequency scenarios were investigated. For both dual- and triple-frequency PPP processing, the significance of GIM and tropospheric products in processing is not obvious in the quality of the

solution after a few hours. However, constraining the atmosphere improves PPP initialization and solution convergence in the first few minutes of processing. The general research question to be answered in this chapter is whether there is any significant benefit in constraining the atmosphere in multi-frequency PPP? A key related question is: Regarding time and position accuracy, how close are we to RTK performance in the age of multi-GNSS PPP-AR?

Chapter 5 evaluates the feasibility of achieving improved positioning accuracy with raw GNSS measurements from recently released smartphones. Using PPP as the processing mode, positioning accuracy and performance of selected newly available devices are analyzed. These devices include the Xiaomi Mi8, Google Pixel 3, Huawei Mate 20 and Samsung Galaxy S9. All tested devices had the capability of tracking either three or four GNSS constellations, and the first and third track two frequencies. To enable smartphone data processing, various customizations had to be made, both conceptually and in software design.

Chapter 6 investigates the performance of recent state-of-the-art receiver chipsets using multi-GNSS PPP in assessing the solution and measurement quality of these sensors. The receivers examined in this chapter include: the Piksi Multi Module, Unicorecomm Nebulas II and U-blox F9 sensors. Static and kinematic scenarios were considered with detailed measurement, solution accuracy and residual analyses made with reference to geodetic-grade receivers.

Finally, Chapter 7 summarizes all the findings and provides recommendations for research in the near future.

CHAPTER 2 ANALYSIS OF MULTI-GNSS TRIPLE-FREQUENCY PRECISE POINT POSITIONING INITIALIZATION

With an increase in the number of satellite systems, redundant measurements, and improved satellite orbit and clock products, the initial convergence period of dual-frequency GNSS Precise Point Positioning (PPP) borders on tens of minutes to achieve an accuracy of a few centimetres. However, dual-frequency PPP still remains impractical for many real-time applications due to this relatively long convergence period. The introduction of a fully operational third frequency promised faster convergence and almost instantaneous integer resolution of ambiguities. However, the expectation of triple-frequency PPP has, so far, not been met with reliable quick fixing of float carrier-phase ambiguities due to limited number of satellites (Wang and Rothacher 2013). The objective of this work is to draw attention to the challenges and methods available for quickly attaining accurate position initialization for float PPP solutions, while analyzing the intricate issues that have to be dealt with in doing so. This chapter concentrates on the first few minutes of PPP convergence in dual- and triple-frequency scenarios to analyze and contribute to improvements of the float solution before the resolution of ambiguities.

2.1 Introduction to uncombined triple-frequency PPP

Improving initial convergence period has been one of the most challenging and popular areas of research in PPP. With the increasing number of satellites and the addition of more frequencies, one potential solution is to make use of triple-frequency measurements. However, over a 24-hour period, the improvement offered by triple-frequency PPP is only marginal compared to the dual-frequency approach. For time sensitive applications, the minimal improvement offered may be insignificant in terms of accuracy, but the third frequency does add reliability to the solution (Henkel and Günther 2010; Elsobeiey 2014). It is therefore imperative to address, analyse and improve PPP convergence period in the first few minutes with the available multi-GNSS frequency measurements. A further approach to improve convergence is through constraining the ionosphere in PPP data processing. Ionospheric-constrained PPP has been shown to improve solution accuracy and convergence by 30% through the use of un-combined GNSS observables and uncalibrated phase delay products (e.g., Li et al. 2013b). This approach will be addressed in Chapters 3 and 4.

There are currently 35 BeiDou, 12 GPS Block IIF and 21 Galileo satellites transmitting a third frequency, but not all of them are continuously visible and capable of being tracked by receiver stations (Laurichesse and Blot 2016). Rather, there are currently, on average, 15 visible satellites transmitting a third frequency over the Asia-Pacific region. Triple-frequency PPP with GPS, Galileo and BeiDou offers various

flavours of measurements that strengthen PPP solution quality and initial convergence period. Plans are underway for the launch of GLONASS-K2 satellites in 2019 that will transmit an L3 signal and bridge the compatibility gap with other GNSSs by switching from Frequency Division Multiple Access (FDMA) to Code-Division Multiple Access (CDMA) (Urlichich et al. 2011). To achieve the goal of faster initial PPP solution convergence, current research has been focused on the application of external atmospheric information (Collins et al. 2012; Banville et al. 2014; Laurichesse and Blot 2016) and the use of the extra widelane provided by third frequency measurements (Geng and Bock 2013; Li et al. 2013a; Tang et al. 2014; Elsobeiey 2014; Laurichesse and Blot 2016; Gayatri et al. 2016). However, little emphasis has been placed on how different observable and constellation weighting schemes affect the initialization of triple-frequency PPP float solutions.

Conventionally, ionosphere-free linear combination is used to eliminate the first order ionospheric effect in PPP processing (Zumberge et al. 1997; Bisnath and Gao 2009). Assuming two measurements, pseudorange (M_i) and carrier-phase (M_j), at frequencies f_i and f_j, respectively, the ionosphere-free combination (M_{ij}) is given by:

$$M_{ij} = \alpha_{ij} M_i + \beta_{ij} M_j \qquad 2.1$$

where

$$\alpha_{ij} = \frac{f_i^2}{f_i^2 - f_j^2} \tag{2.2}$$

$$\beta_{ij} = 1 - \alpha_{ij} = -\frac{f_j^2}{f_i^2 - f_j^2} \tag{2.3}$$

Considering triple-frequency GNSS measurements (M_k) with the third frequency represented as f_k, ionosphere-free linear combinations can be expressed in a matrix format as shown below:

$$L_{IF} = \begin{bmatrix} M_{ij} \\ M_{ik} \\ M_{jk} \end{bmatrix} = \begin{bmatrix} \alpha_{ij} & \beta_{ij} & 0 \\ \alpha_{ik} & 0 & \beta_{ik} \\ 0 & \alpha_{jk} & \beta_{jk} \end{bmatrix} \begin{bmatrix} M_i \\ M_j \\ M_k \end{bmatrix} = F.L_0 \tag{2.4}$$

Assuming the GNSS measurements are uncorrelated and have the same a priori standard deviation, the variance-covariance matrix of the uncombined measurements (C_{l_0}) can be written as:

$$C_{l_0} = \begin{bmatrix} \sigma_i^2 & 0 & 0 \\ 0 & \sigma_j^2 & 0 \\ 0 & 0 & \sigma_k^2 \end{bmatrix} \tag{2.5}$$

Applying the law of error propagation, the variance-covariance matrix of the combined ionosphere-free linear combination involving three frequencies can be represented as:

$$C_{l_{IF}} = FC_{l_0}F^T = \sigma_0^2 \begin{bmatrix} \alpha_{ij}^2 + \beta_{ij}^2 & \alpha_{ij}\alpha_{ik} & \beta_{ij}\alpha_{jk} \\ \alpha_{ij}\alpha_{ik} & \alpha_{ik}^2 + \beta_{ik}^2 & \beta_{ik}\beta_{jk} \\ \beta_{ij}\alpha_{jk} & \beta_{ik}\beta_{jk} & \alpha_{jk}^2 + \beta_{jk}^2 \end{bmatrix} \quad 2.6$$

Expanding on equations 1.1 and **1.2**, the observation model equations can be augmented considering pseudorange $P_{L_i}^{mn}$and carrier-phase $\Phi_{L_i}^{mn}$ from satellite m to station n.

$$P_{L_i}^{mn} = \rho^{mn} + \frac{k}{f_{L_i}^2} + M_w^{mn} ZPD^m + c(\partial t^m - \partial t^n) + c\left(D_{P_{Li}}^m - D_{P_{Li}}^n\right) + \varepsilon\left(P_{L_i}^{mn}\right) \quad 2.7$$

$$\varphi_{L_i}^{mn} = \rho^{mn} - \frac{k}{f_{L_i}^2} + M_w^{mn} ZPD^m + c(\partial t^m - \partial t^n) + c\left(UPD_{\varphi_{Li}}^m - UPD_{\varphi_{Li}}^n\right) + \frac{c}{f_{Li}} N_{Li} + \varepsilon\left(\varphi_{L_i}^{mn}\right) \quad 2.8$$

Where

ρ^{mn}	Geometric distance between station and satellite.
$\frac{k}{f_{L_i}^2}$	First order ionospheric delay.
$M_w^{mn} ZPD^m$	Wet component of the tropospheric delay where $ZPD^m$is the tropospheric zenith delay. M_w^{mn} represents the elevation-dependent mapping function.
c	Speed of light.

$\partial t^m, \partial t^n$	Station and satellite clock biases, respectively.
$D^m_{P_{Li}}, D^n_{P_{Li}}$	Pseudorange delays for frequency f_{Li} for station and satellite, respectively.
$UPD^m_{\varphi_{Li}}, UPD^n_{\varphi_{Li}}$	Uncalibrated carrier-phase delays for frequency f_{Li} for station and satellite, respectively.
N_{Li}	Integer carrier-phase ambiguity for frequency f_{Li}.
$\varepsilon\left(P^{mn}_{L_i}\right), \varepsilon\left(\varphi^{mn}_{L_i}\right)$	Noise, multipath and unmodelled instrumental errors for pseudorange and carrier-phase measurements for station and satellite, respectively.

Considering equation 2.1 for frequencies f_i and f_j, the ionosphere-free pseudorange and carrier-phase observables can be written as:

$$P^{mn}_{ij} = \rho^{mn} + M^{mn}_w ZPD^m + c\left(\partial t^m_{ij} - \partial t^n_{ij}\right) + \varepsilon\left(P^{mn}_{ij}\right) \quad 2.9$$

$$\varphi^{mn}_{ij} = \rho^{mn} + M^{mn}_w ZPD^m + c\left(\partial t^m_{ij} - \partial t^n_{ij}\right) + a^{mn}_{ij} + \varepsilon\left(\varphi^{mn}_{ij}\right) \quad 2.10$$

Where ∂t^m_{ij} and ∂t^n_{ij} being station and satellite ionosphere-free clock terms, can be expressed as:

$$dt^m_{ij} = dt^m + \alpha_{ij} D^m_{P_i} + \beta_{ij} D^m_{P_j} = dt^m + D^m_{P_{ij}} \quad 2.11$$

$$dt^n_{ij} = dt^n + \alpha_{ij} D^n_{P_i} + \beta_{ij} D^n_{P_j} = dt^n + D^n_{P_{ij}} \quad 2.12$$

From equation 2.10, the non-integer ambiguity term a_{ij}^{mn} results from α_{ij} and β_{ij} and receiver and satellite hardware delays, can be further expanded as:

$$a_{ij}^{mn} = \alpha_{ij}\left(\frac{c}{f_i}N_i + cUPD_{\varphi_i}^{m} - cD_{P_i}^{m} - cUPD_{\varphi_i}^{n} + cD_{P_i}^{m}\right) + \beta_{ij}\left(\frac{c}{f_j}N_j + cUPD_{\varphi_j}^{m} - cD_{P_j}^{m} - cUPD_{\varphi_j}^{n} + cD_{P_j}^{m}\right) \quad 2.13$$

Focusing on GPS L1/L2 and L1/L5 measurements, given the L5 third frequency, the functional observation models for the three frequencies, can be written as:

$$P_{L1/L2}^{mn} = \rho^{mn} + M_w^{mn}ZPD^m + c\left(\partial t_{L1/L2}^{m} - \partial t_{L1/L2}^{n}\right) + \varepsilon\left(P_{L1/L2}^{mn}\right) \quad 2.14$$

$$\varphi_{L1/L2}^{mn} = \rho^{mn} + M_w^{mn}ZPD^m + c\left(\partial t_{L1/L2}^{m} - \partial t_{L1/L2}^{n}\right) + a_{L1/L2}^{mn} + \varepsilon\left(\varphi_{L1/L2}^{mn}\right) \quad 2.15$$

$$P_{L1/L5}^{mn} = \rho^{mn} + M_w^{mn}ZPD^m + c\left(\partial t_{L1/L2}^{m} - \partial t_{L1/L2}^{n}\right) + b_{L1/L5}^{mn} + \varepsilon\left(P_{L1/L5}^{mn}\right) \quad 2.16$$

$$\varphi_{L1/L5}^{mn} = \rho^{mn} + M_w^{mn}ZPD^m + c\left(\partial t_{L1/L2}^{m} - \partial t_{L1/L2}^{n}\right) + b_{L1/L5}^{mn} + a_{L1/L5}^{mn} + \varepsilon\left(\varphi_{L1/L5}^{mn}\right) \quad 2.17$$

Where $\partial t_{L1/L2}^{n}$ represent the satellite clocks associated with the ionosphere-free L1/L2 combination. The new term $b_{L1/L5}^{mn}$ represent a lumped effect of receiver and satellite inter-frequency biases. Throughout this chapter, $b_{L1/L5}^{mn}$ will be referred to as the L5 equipment bias. The L5 bias can be decomposed into the following:

$$b_{L1/L5}^{mn} = c\left(\partial t_{L1/L5}^{m} - \partial t_{L1/L5}^{n} - \partial t_{L1/L2}^{m} + \partial t_{L1/L2}^{n}\right) = b_{L1/L5}^{m} - b_{L1/L5}^{n} \quad 2.18$$

The use L1/L5 measurements in PPP processing necessitates the mitigation of L5 equipment biases and L5 ambiguity term ($a_{L1/L5}^{mn}$).

The first objective of this work is to examine the estimation of L5 equipment delays with respect to L1 and L2 measurements, emphasizing their characteristics and the provision of explanations for the unique trends observed in these quantities. GPS Block IIF satellites exhibit L5 equipment delay variations over time which correlates to the periodic characteristics observed. The L5 equipment delays are temperature and elevation dependent, which are compounded by the eclipsing of the satellites as the illumination of the Sun varies (Montenbruck et al. 2011). The L5 bias corrections provided by Centre national d'études spatiales (CNES) are applied to triple-frequency float solutions to analyse the impact the corrections have on the user solution. As a second objective, the need for realistic weighting of observations between satellite constellations and how this stochastic modelling affects positioning accuracy in the first few minutes is investigated. In terms of measurements and satellite constellations, three weighting schemes are investigated to see the impact they would have on triple-frequency float solutions.

2.2 Three constellation, triple-frequency measurement analysis

The L1 and L2 dual-frequency ionosphere-free linear combination has been the convention for GNSS PPP processing for quite a number of years (Zumberge et al.

1997; Héroux et al. 2001; Chen and Gao 2005; Leandro et al. 2011). However, there is a gradual transition being made from dual- to triple-frequency measurement processing, which has ushered in renewed research activity to enhance PPP solution quality. Shown in Figure 2.1 is the GNSS frequency spectrum in the L-band for GPS, GLONASS, Galileo and BeiDou.

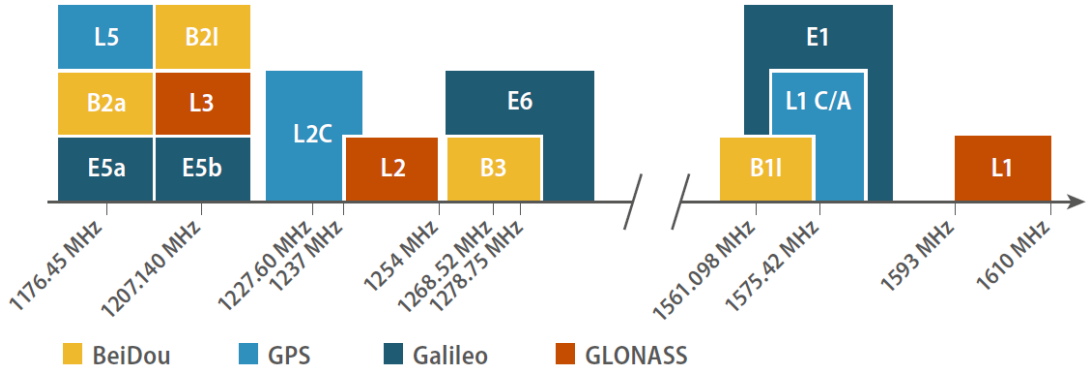

Figure 2.1: GNSS frequency spectrum in the L-band (Source: European GNSS Agency 2018)

With the deployment of GPS Block IIF satellites, the L5 signal is not only intended as a third frequency carrier phase measurement, but also for safety of life (SoL) service (Hofmann-Wellenhof et al. 2007; Jan 2010). In the same vein as shown in Figure 2.1, Galileo and BeiDou currently operate on the E1/E5a/E5b and B1/B2/B3 carriers, respectively, allowing for triple-frequency PPP amongst all three satellite constellations. Similar to GPS's L5, Galileo's E6 carrier is also intended for SoL applications. The major differences between the GNSSs lie in signal design and

structure. However, to facilitate receiver manufacturing and data processing, the GNSSs signals are designed to be interoperable, including that different ionospheric-free combinations can be formed. The issue of interoperability is improved given the close ranges in the frequency bands shared by the three constellations on their third frequencies (Schönemann et al. 2011; Fairhurst et al. 2001). The RINEX 3 format (Gurtner and Estey 2007) offers a plethora of carrier frequencies and code modulations of different "flavours" on GNSS satellite constellations with three frequencies, as summarized in Table 2.1. These "flavours" represent the different observations that can be obtained from the frequency bandwidths of available GNSSs.

GNSS	Frequency	Number of	
		Codes	Phases
GPS	L1	20	22
	L2		
	L5		
GLONASS	G1	4	4
	G2		
Galileo	E1	19	19
	E5		
	E6		
BeiDou	B1	9	9
	B2		
	B3		

Table 2.1: Frequencies and number of observables for each GNSS satellite constellation (Gurtner and Estey 2007)

Though the increase in the number of measurements from dual-frequency to triple-frequency constellations is considered very good, it presents challenges in how to combine the different observable flavours to obtain the best solution quality for PPP data processing. Observable selection inadvertently plays a role in PPP processing given that some observable flavour selections are better than others. Table 2.2 shows the selection strategy employed for RINEX 3 PPP processing in the York PPP engine and throughout this chapter. This selection strategy was put together by the author and implemented in the York PPP engine as a scientific contribution.

The prioritization of the observables here is based on the GNSS channel or type of code modulation. Channels with anti-jamming and anti-spoofing capabilities were weighted more than observables from less capable channels. For instance, the C1W observable is preferred over C1P because of its anti-spoofing and Z-tracking capabilities. As shown in Table 2.2, the PPP user is faced with the challenge of appropriately selecting observables for data processing given the different combinations that can be made based on preference. It must be noted that the selection strategy outlined in Table 2.2 is the internal standard followed in the YorkU-PPP engine (Seepersad 2012; Aggrey 2015).

	RINEX 2 observables	RINEX 3 observables	
		Default choice	Alternative
GPS	P1	C1W	C1P→C1X→C1L→C1S
	P2	C2W	C2P → C2X → C2L → C2S
	P3*	C5X	
	C1	C1C	
	C2	C2C	
	L1	L1W	L1P→L1X→L1L→L1S
	L2	L2W	L2P→L2X→L2L→L2S
	L5	L5X	
GLONASS	P1	C1P	
	P2	C2P	
	C1	C1C	
	C2	C2C	
	L1	L1P	L1C
	L2	L2P	L2C
Galileo	P1	C1X	CIC→C1B→C1A
	P2	C6X	C6C→C6B→C6A
	P3*	C8X	C8Q→C8I→C7X→C7Q→C7I→C5X→C5Q →C5I
	L1	L1X	LIC→L1B→L1A
	L2	L6X	L6C→L6B→L6A
	L3*	L8X	L8Q→L8I→L7X→L7Q→L7I→L5X→L5Q →L5I
BeiDou	P1	C2X	C2Q→C2I or C1I
	P2	C7X	C7Q→C7I
	P3*	C6X	C6Q→C6I
	L1	L2X	L2Q→L2I or L1I
	L2	L7X	L7Q→L7I
	L3*	L6X	L6Q→L6I

Table 2.2: Strategy for observable selection where P3 and L3 denotes precise code and phase measurement on the third frequency. *Third frequency observables not included in the RINEX 2 format.

The emphasis lies in the possible user choice of observables to process and its potential impact on the positioning results. The user also has the flexibility of assigning other choices of observables in case the default choice is not available, as shown in Table 2.2. It is well known that different receiver types track different GNSS signals. According to the receiver type used, there is dependence between the choice of observables and the receiver which would affect the solution quality obtained.

Figure 2.2 shows the horizontal and vertical positioning error components for station GMSD in Nakatane, Japan detailing the marginal benefit that the float triple-frequency PPP solution has over its dual-frequency counterpart. The site GMSD was selected because its results reflect the typical results seen for all other stations processed (which will be specified later in this chapter). Post-processed orbits and clock products obtained from the Multi-GNSS Experiment (MGEX) campaign were used (Rizos et al. 2013). In the dual-frequency case, the standard L1/L2, E1/E2, B2/B3 ionosphere-free linear combinations were formed for GPS, Galileo and BeiDou satellites, respectively. Ionosphere-free linear combinations were formed for L1/L5, E1/E5 and B2/B3 signals in the triple-frequency case for GPS, Galileo and BeiDou satellite systems, respectively. Graphically (see Figure 2.2) and statistically (see Table 2.3), the third frequency produces only a few millimetres positioning improvement over a day. It must be noted that the L1/L2/L5, E1/E2/E5 and B1/B2/B3 biases were

not accounted for in the results shown for site GMSD – more on these biases later in the chapter.

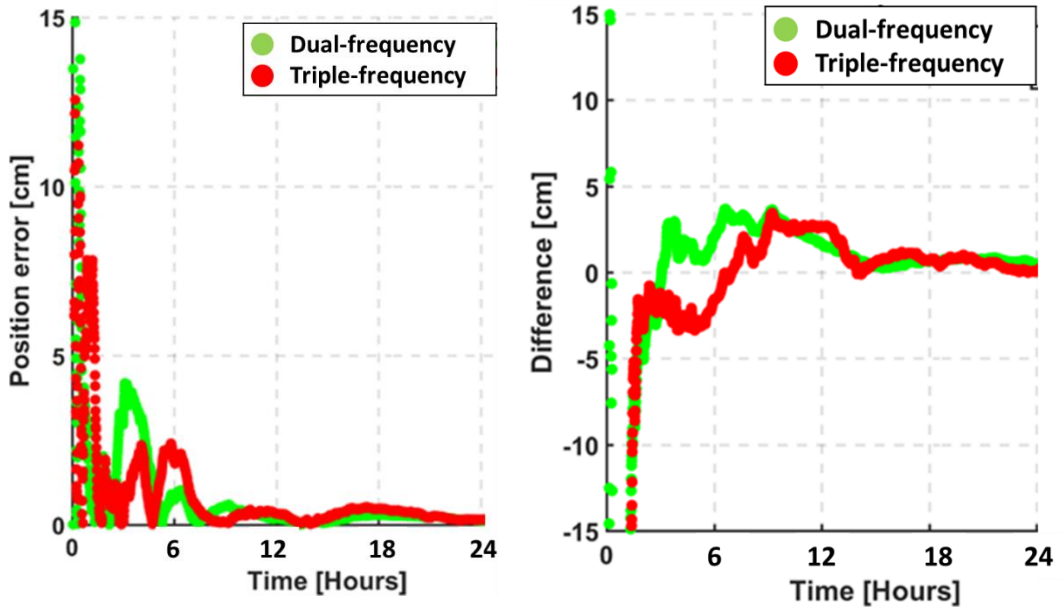

(a) Horizontal positioning error (b) Vertical error component

Figure 2.2: Site GMSD DOY 83 of 2016 located in Nakatane, Japan, illustrating the differences between the "float" solutions. All units are in centimetres and different axis limits are utilized for horizontal and vertical subplots.

		Dual-frequency (in cm)	Triple-frequency (in cm)
Std dev	**E**	0.36	0.22
	N	0.08	0.12
	U	0.15	0.41
Bias	**E**	-1.06	-1.49
	N	0.17	0.38
	U	-0.49	0.01
Rms Error	**E**	1.45	1.52
	N	0.21	0.33
	U	0.59	0.58

Table 2.3: Statistics of dual- and triple-frequency float PPP solutions for the site GMSD in 2016 for DOY 83 located in Nakatane, Japan.

The primary reason why triple-frequency offers so little position improvement is due to the fact that additional measurements are introduced with similar geometry as the dual-frequency measurements. The remaining unmodelled effects are time varying error sources such as multipath and ionosphere, which require a priori knowledge or averaging through time to reduce their effects (Hofmann-Wellenhof et al., 2007). Another reason is the presence of unmodelled hardware delays introduced by the addition of a third frequency (Tegedor and Øvstedal 2014). Shown in Figure 2.3 are the pseudorange residuals, as a function of elevation angle, for dual- and triple-frequency PPP float solutions for the site GMSD located in Nakatane from DOY 83, 2016. Though such dependence is expected as seen in Figure 2.3 (a), it was necessary to draw attention to the difference that characterizes both the dual- and triple-

frequency scenarios. As seen in Figure 2.3 (b), the triple-frequency pseudorange residuals have more inherent unmodelled errors as compared to the dual-frequency case. A few factors could potentially contribute to this phenomenon. Bearing in mind the use of a third frequency, inter-frequency channel biases between the linear combinations formed could be a contributing factor (Tegedor and Øvstedal 2014; Montenbruck et al. 2017). The L1/L5, E1/E5 and B1/B3 linear combinations were formed for GPS, Galileo and BeiDou float PPP solutions, respectively. These inter-system, inter-frequency biases coupled with other correlated hardware biases appear in the post-fit residuals as evidenced in Figure 2.3 and Figure 2.4.

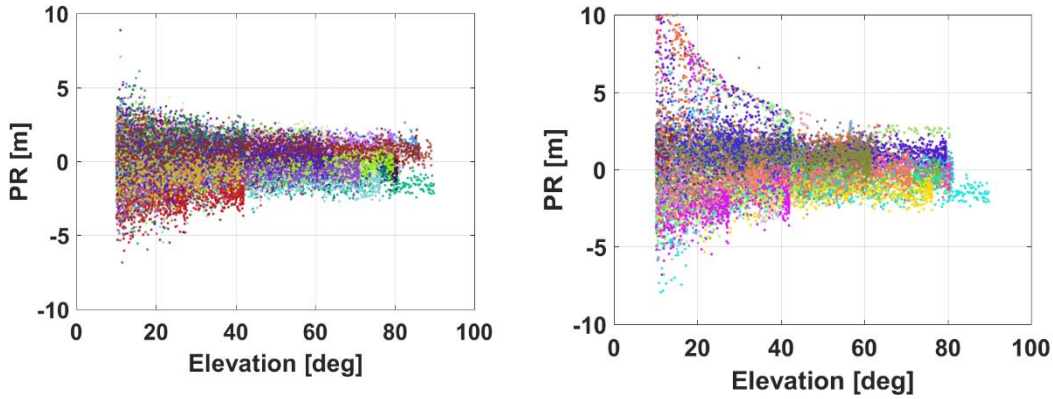

(a) Dual-frequency (b) Triple-frequency

Figure 2.3: Pseudorange post-fit residuals elevation dependence for GMSD in 2016 for DOY 83.

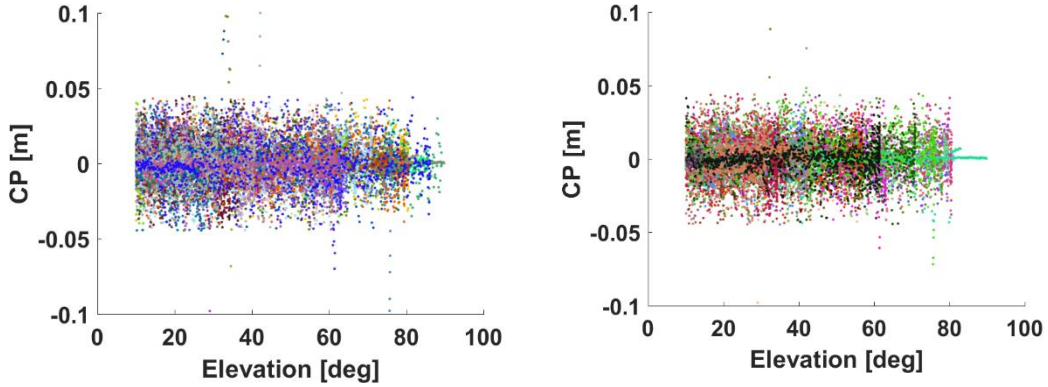

(a) Dual-frequency (b) Triple-frequency

Figure 2.4: Carrier-phase post-fit residuals elevation dependence for GMSD in 2016 for DOY 83.

Though the carrier-phase residuals for the triple-frequency solution are biased as well, the magnitude of the biases are at the millimetre level (Tegedor and Øvstedal 2014) which is not noticeable in Figure 2.4b. Resolving ambiguities on the third frequencies become challenging due to the possible absorption of hardware delays by the carrier-phase cycle ambiguities.

Over a 24-hour period, it has been shown here that the benefit of triple-frequency PPP is very marginal. However, the question of how triple-frequency measurements impact PPP solution initialization is still a valid one, prompting further investigation. Is the impact of triple-frequency in PPP float initialization as marginal as it is over a 24-hour period? To probe further, 20 global multi-GNSS stations were

selected for processing to find probable answers and arrive at logical conclusions. Figure 2.5 shows the global distribution of the 20 stations selected for the experiment.

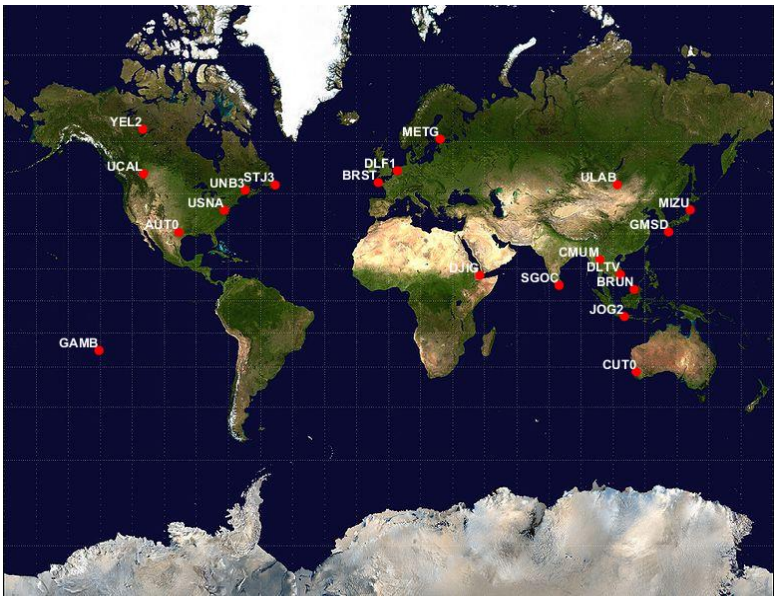

Figure 2.5: Map of globally distributed stations

The impact of triple-frequency PPP was investigated using the 20 distributed global stations with multi-GNSS capabilities. Results are presented for GPS (G) + GLONASS (R) + Galileo (E) + BeiDou (C) dual- and triple-frequency PPP float solutions. The definition of PPP initialization used here is quite different from convergence period. There was no restriction placed on the steady state of the solutions either spatially or temporally. Irrespective of the magnitude of the horizontal errors, the impact of how triple-frequency float PPP solutions are affected within a specified time period, is the prime objective of the experiment. Figure 2.6 shows the result of

dual- and triple-frequency PPP solutions of 20 stations within 5, 10, 15, 20, 25, and 30-minute initialization periods.

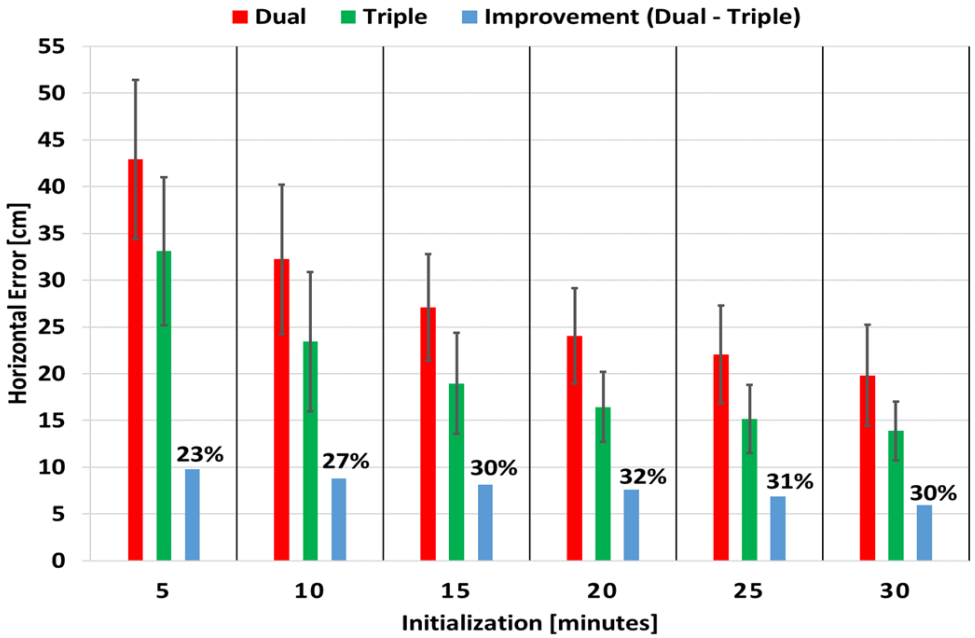

Figure 2.6: Dual- and triple-frequency PPP solutions of 20 stations within a 30-minute initialization period. Blue bars show the difference between dual- and triple-frequency solutions and labelled as percentages. Error bars represent 1 sigma uncertainty.

As shown in Figure 2.6, the obvious question of whether triple-frequency measurements help in initialization is answered: Yes. The associated question is how significant is the improvement of triple-frequency measurements in comparison to dual-frequency PPP solutions? In the first 5 minutes, there is an improvement of 23% in the triple-frequency PPP solutions in comparison to the dual-frequency float solutions equating to a 10 cm error reduction. However, a 27% improvement is seen

in 10 minutes when compared to the 5-minute threshold. If a 10-minute convergence is defined for a decimetre threshold, the level of improvement seen for triple-frequency measurements become irrelevant especially for real-time or high accuracy applications. However, it must be clarified that the issue of relevance in the level of improvement in triple-frequency PPP float solutions tend to become subjective depending on the rigidness in defining convergence. In terms of PPP float solution initialization however, without factoring in a strict definition of convergence, triple-frequency measurements do improve the solution significantly.

2.3 L5 bias estimation and correction analysis

Since the first launch of the SVN62 with the transmission of the L5 signal on 28th March 2010, the PPP community has been dealing with the bias that exists between the L1, L2 and L5 frequencies for GPS. According to Montenbruck et al. (2011), the L5 biases are caused by the effects of temperature fluctuations, which appear as variations in the periodicity of the signal. These observed periodic changes depend on the elevation of the Sun with respect to the satellite's orbital plane. Given these periodicities, it was suggested that a linear-plus-periodic model function would be applicable in the modelling of the time variations between the L1, L2 and L5 signals. The validity of the proposed model, tested over an 8-month period showed an rms of 1 cm.

The significance of the L5 bias has not yet prompted a correction format from IGS. However, work has already begun in defining a SINEX bias format (Laurichesse and Blot 2016; Laurichesse, 2015). The proposed format is an expansion on the MGEX differential code biases (DCB), which specifically provides the user with the bias affecting the raw observables on the signals. This approach relieves the user from taking into account the complexities of the computations and modelling done at the IGS Analysis Centers to estimate the biases. The benefit in providing the corrections comes in fixing the ambiguities in PPP-AR, as well as giving the user the flexibility of forming linear combinations using the specific observable bias corrections in either float or fixed solutions.

Currently, CNES offers the bias SINEX corrections as a free service (Laurichesse and Blot 2016; Laurichesse, 2015). These corrections were applied in the previously presented triple-frequency float PPP solutions with the aim of investigating any improvement in the initialization of the solutions. Figure 2.7 shows the results for triple-frequency float PPP solutions of the 20 stations with and without the bias corrections applied only for GPS L5 pseudorange and carrier-phase observables.

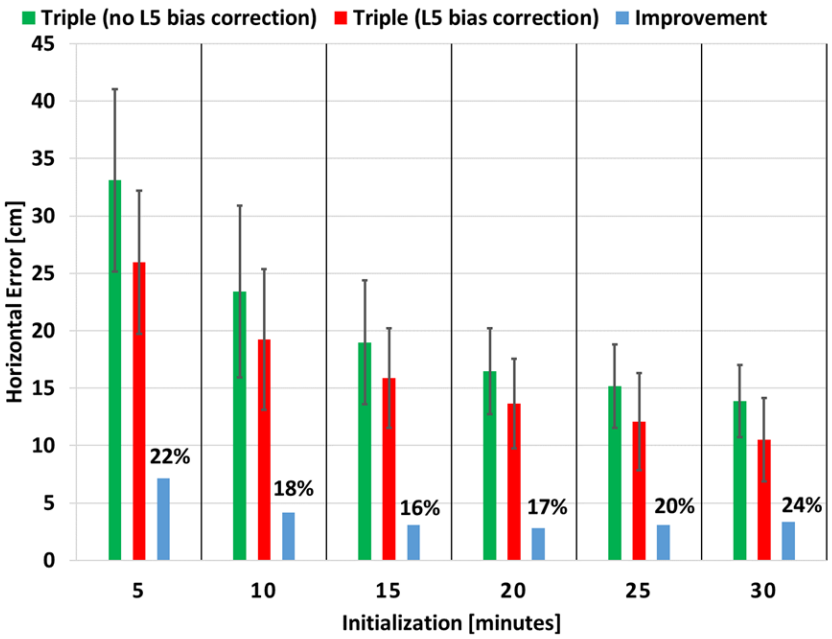

Figure 2.7: Triple-frequency PPP solutions of 20 stations within a 5, 10 and 15 minute initialization periods with and without L5 bias correction. Error bars represent 1 sigma uncertainty. GPS, GLONASS, Galileo and BeiDou satellites were processed.

There was a 22% improvement in the first 5 minutes compared to the triple-frequency results without the L5 bias correction applied. However, the level of improvement is not significant for its impact to be seen over time considering that the ambiguities are not being fixed (Tegedor and Øvstedal, 2014). It is expected and has been proven ((Laurichesse 2015; Laurichesse and Blot 2016) that in a PPP-AR scenario, the level of improvement will be higher than seen in the float solution case.

Figure 2.8 shows the level of improvements observed when the triple-frequency solutions, corrected for L5 biases, were compared to the dual-frequency solutions.

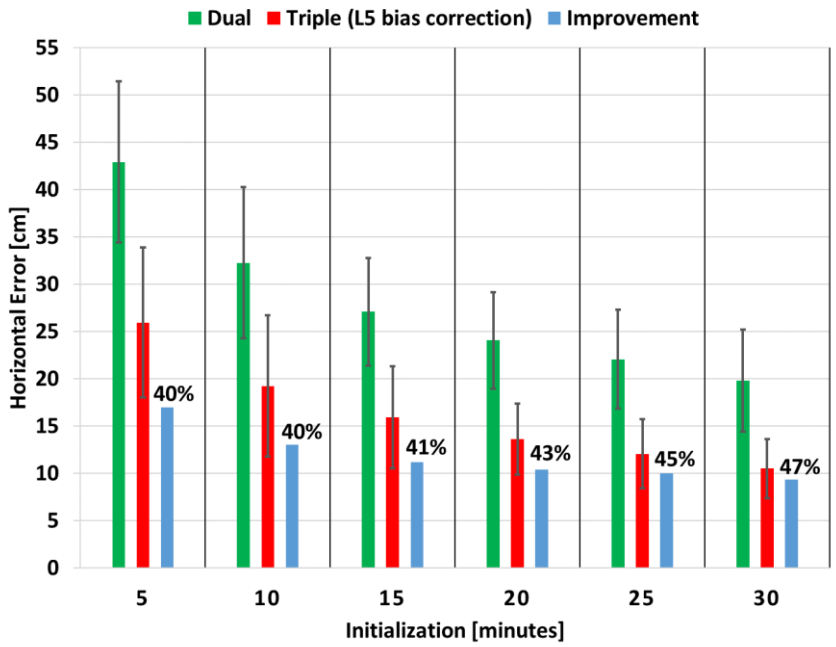

Figure 2.8: Dual- and triple-frequency PPP solutions of 20 stations within a 5, 10 and 15 minute initialization periods. Triple freqency solutions have L5 bias corrections applied. Error bars represent 1 sigma uncertainty. GPS, GLONASS, Galileo and BeiDou satellites were processed.

The first 5 minutes showed a 40% improvement in the PPP initialization of the triple-frequency solutions, in comparison to the dual-frequency. Over a period of 30 minutes, an average of 42% improvement was observed. These improvements are significant as they portray how triple-frequency measurements, corrected for inherent biases, can contribute to PPP initialization and convergence. The results presented in Figure 2.7 and Figure 2.8 are novel and significant contributions in comparison to published research work. Elsobeiey (2014) showed that the usage of triple-frequency

combinations could improve the PPP convergence by about 10%. Using simulated triple-frequency measurements, Tegedor and Øvstedal (2014) further showed the characteristics of GPS L5 biases and their consistency over days. The results presented in this section augment these published ones by showing the performance progression for dual- and triple-frequency uncombined PPP initializations for multiple stations considering various time stamps while mitigating the L5 biases.

2.4 Effects of different stochastic weighting schemes

It is well known that the reliability of estimated parameters in a least squares approach depends on realistic functional as well as stochastic modelling. The mathematical relationship between GNSS measurements and estimated parameters is defined by the functional model; whereas, the covariance matrix sheds light on the stochastic or statistical properties of the measurements. Hence, it is necessary to define realistic weighting schemes without neglecting temporal and spatial correlations that might exist between the measurements and their sources (Amiri-Simkooei et al. 2015; Luo et al. 2009). With four GNSSs, the choice of prioritizing one GNSS over another could potentially affect the solution quality. As an experiment, various weights were applied for each GNSS with priority given to GPS over all the others due to the quality of measurements and orbit and clock products. Given that GLONASS pseudorange measurements are noisier than all the others and the quality of the orbit and clock products tend to be worse than GPS, less weight is given to these GLONASS

observables (Hadas and Bosy 2015). The interesting factor then lies with Galileo and BeiDou weighting ratios and how they impact triple-frequency PPP solution initialization. Both Galileo and BeiDou were weighted less than GPS because they are relatively new constellations and the quality of their clocks and orbit products are not as accurate as those of GPS (e.g., Tegedor et al. 2014). Table 4 provides realistic weighting schemes for each GNSS based on a much larger array of experimental weighting schemes. W_G represents the pseudorange and carrier-phase weights allocated for GPS, which are a function of the satellite elevation, as well as orbit and clock uncertainties.

Weighting scheme	GPS	GLONASS	Galileo	BeiDou
Scheme 1	Equal weights			
Scheme 2	W_G	$\frac{1}{2}W_G$	W_G	W_G
Scheme 3	W_G	$\frac{1}{2}W_G$	$\frac{3}{4}W_G$	$\frac{3}{4}W_G$

Table 2.4: Realistic weighting schemes applied to GPS, GLONASS, Galileo and BeiDou triple-frequency PPP float solutions.

The dual- and triple-frequency float PPP results presented so far utilized weighting scheme 2 of Table 2.4. Schemes 1 and 3 were investigated with the purpose of finding out how those schemes affect PPP initialization. It must be noted that various permutations could be made to obtain various other schemes but in the scope of these experiments, only three were addressed. Figure 2.9 shows the results of using

schemes 1 and 3 in comparison to scheme 2. The results are somewhat counterintuitive to the initial assumptions, as one would expect that Scheme 3 may have provided the most accurate positioning solution. However, for the datasets processed, these are the results obtained.

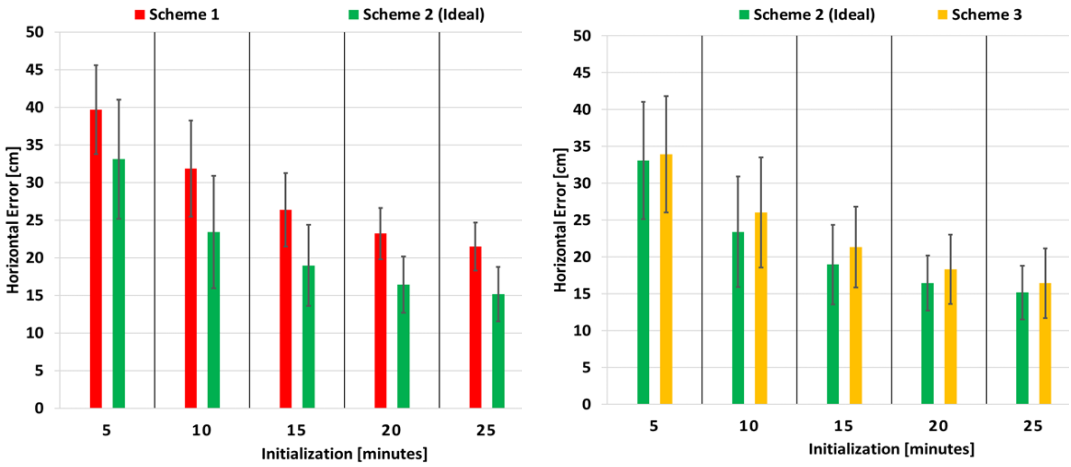

(a) (b)

Figure 2.9: Results for 3 different weighting schemes comparison of 20 stations. (a) Ideal scheme against scheme 1 (b) Ideal scheme against scheme 3. Error bars represent 1 sigma uncertainty.

Investigating further, various weighting schemes between GNSS observable types for each satellite constellation was tested. Though the choice of applying various weights to the observables did not deviate significantly from the GNSS-based weights, the purpose was to observe the effect that specific observable weighting had on PPP solutions and initialization. Based on the observable type, realistic proportions of weights were applied as summarized in Table 2.5. It must be noted that the flavour of

observable type was not taken into consideration given the added complexity it would add to the matrix of appropriate weight assignment. However, it is intended and recommended that further investigation be done. GLONASS and BeiDou observables were down weighted because they contribute the most to the equipment bias budget. As shown in Table 2.5, W_Φ, W_P represent weights applied to carrier-phases and pseudoranges, respectively.

	Scheme1		**Scheme 2**	
	Carrier-phase	**Pseudorange**	**Carrier-phase**	**Pseudorange**
GPS	W_Φ	W_P	W_Φ	W_P
GLONASS	W_Φ	$\frac{1}{2}W_P$	W_Φ	$\frac{1}{2}W_P$
Galileo	W_Φ	W_P	W_Φ	W_P
BeiDou	W_Φ	W_P	$\frac{1}{2}W_\Phi$	$\frac{1}{2}W_P$

Table 2.5: Realistic weighting schemes applied to GPS, GLONASS, Galileo and BeiDou triple-frequency PPP float solutions based on observable type.

Figure 2.10 shows the results of two observable weighting schemes applied to triple-frequency PPP processing and their effect on PPP initialization. The potential of un-modelled inter-frequency hardware biases showing in the post-fit residuals and ambiguity parameters runs high especially with GLONASS and BeiDou. The schemes presented are not meant to be interpreted as the only possible schemes, but rather paint a picture of how observable type weighting affects PPP initialization.

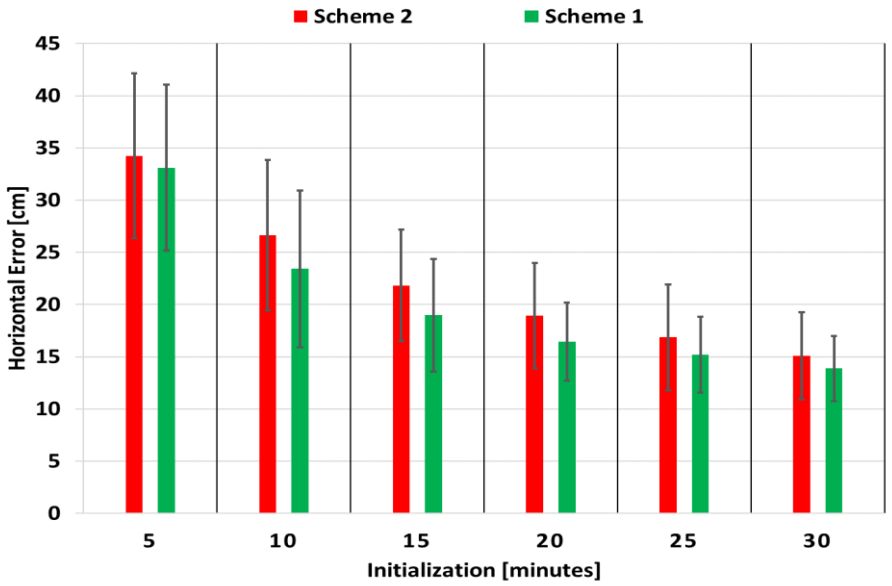

Figure 2.10: Results for 2 different observable type weighting schemes comparison of 20 stations. Error bars represent 1 sigma uncertainty.

As shown in Figure 2.10, scheme 1 only showed marginal improvement over scheme 2. Down-weighting the pseudorange and carrier-phase measurements of BeiDou had no significant effect on PPP initialization in triple-frequency processing mode. The results are obviously indicative that different weighting schemes do affect PPP float solution initialization, whether GNSS-based or observable-type-based. The actual question here is how optimal a weighting scheme should be, given that there are many possible schemes. For instance, Kazmierski et al. (2018) investigated equal and signal noise weighting schemes with regards to dual-frequency measurements from all available GNSSs. The results presented in this section collaborates the marginal

improvements noticed in Kazmierski et al. (2018). Taking a step further, the contributions provided in this section investigated triple-frequency measurements using satellite elevation weighting.

Though the differences between the schemes are only a magnitude of centimetres to millimetres, there are short comings. The schemes investigated in this section are all satellite elevation-dependent, which down-weights observables at low elevations. A problem arises in data processing when there is limited number of observations with low elevation conditions that gets down weighted and possibly rejected.

2.5 Summary

It is concluded that the addition of the third frequency does impact PPP float solution initialization significantly. Improvements of 23% and 27% were observed for the first 5 and 10-minute period, respectively, where the issue of quick convergence is critical. Though results were shown for float solutions, it is anticipated that by resolving ambiguities, the level of improvement should significantly increase. Emphasis was placed on the GPS L5 bias in terms of how its application could potentially aid in PPP float solutions. The CNES SINEX bias format was applied and results show 22% and 18% improvement in the first 5 and 10 minutes, respectively. Given that the ambiguities were not fixed, this level of improvement was expected. It was also shown that by applying different weighting schemes, the triple-frequency

float solutions are impacted in the first few minutes. For constellation-based weighting, down-weighting GLONASS but maintaining equal weights for GPS, Galileo and BeiDou showed a few centimetre-level of improvement compared to when Galileo and BeiDou were down weighted. Observable weighting showed GLONASS pseudorange being down weighted with equal weights for Galileo, GPS and BeiDou. The results were better than further down-weighting GLONASS and Beidou observables.

Future work will focus on the estimation constraining of the ionospheric term, to make use of a priori ionospheric information and its impacts on triple-frequency PPP solution quality. By constraining atmospheric parameters, it is expected that PPP solution accuracy and initialization would improve as evidenced in various research with dual-frequency measurements. Other avenues to improve PPP solutions involve the resolution of float ambiguities either through partial or both wide-lane and narrow-lane fixing. Further investigation would be conducted on the effect BeiDou geostationary (GEO) satellites have on PPP solutions in comparison to BeiDou medium earth orbit (MEO) satellites.

CHAPTER 3 IMPROVING MULTI-GNSS FLOAT PPP CONVERGENCE WITH ATMOSPHERIC CONSTRAINTS

The general objective of this study is to analyze the performance of PPP convergence and initialization while stochastically constraining the effects of atmospheric refraction. One specific objective of this study is to review the performance of dual- and triple-frequency PPP solutions using uncombined measurements. The research question to be answered is whether there is any significant benefit in constraining the atmosphere, specifically the ionospheric refraction, in dual- and triple-frequency PPP processing? This chapter begins by introducing a brief overview of combined and uncombined PPP processing and the key benefits of adopting the uncombined processing approach. Using dual- and triple-frequency observables, the efficacy of ionospheric constraints is demonstrated.

3.1 Introduction

As highlighted in Chapter 2, conventional GPS and GNSS Precise Point Positioning (PPP) processing makes use of the dual-frequency, ionosphere-free linear combination (Zumberge et al. 1997; Héroux et al. 2001; Chen and Gao 2005; Leandro et al. 2011). However, PPP implementation has changed from the usage of dual-

frequency measurements to a triple-frequency approach (Hofmann-Wellenhof et al. 2007; Jan 2010; Schönemann et al. 2011; Fairhurst et al. 2001). Opportunities and challenges are both presented with modernized GPS, GLONASS, Galileo and BeiDou constellations when solution accuracy, reliability and integrity become the focus (Henkel and Günther 2010; Elsobeiey 2014). Some prominent areas demanding attention in the quest to enhance PPP performance are convergence and initialization (Seepersad and Bisnath 2012, 2014a, b). Accounting for the challenges of PPP convergence and initialization are key to improving solution quality for various applications. Previous research contributions have improved the solution quality in dual- and triple-frequency PPP either through linear combinations or by uncombining the raw measurements (Pengfei et al. 2011; Zhang et al. 2013; Odijk et al. 2016; Liu et al. 2017). However, the question of and answer to how close PPP is to Real-Time Kinematic (RTK) performance is still blurry. The uncombined PPP approach implies the estimation of ionospheric delay parameters which can further be strengthened through a priori ionospheric knowledge (Collins et al. 2012; Ge et al. 2012; Banville et al. 2014; Laurichesse and Blot 2016). The extra widelane provided by third frequency measurements is expected to enable faster initial PPP solution convergence (Geng and Bock 2013; Li et al. 2013a; Tang et al. 2014; Elsobeiey 2014; Laurichesse and Blot 2016; Gayatri et al. 2016). However, there are currently no available sources of products for extra widelane ambiguity resolution.

The positioning performance for both geodetic and low-cost receivers has been shown to improve with Global Ionospheric Maps (GIMs) which are produced by, e.g., the International GNSS Service (IGS) (Schaer et al. 1998). Given that GIM is based on phase-smoothed code observations, the DCB information provided in the IONEX file is only beneficial to code-only, single-frequency receivers. For dual-frequency PPP processing, the significance of GIM in processing is not obvious in the quality of the solution as compared to complete elimination of the ionosphere through linear combination. Using GIM and localized regional ionospheric corrections, performance assessments are provided for dual- and triple-frequency multi-GNSS PPP solutions. Various research contributions have highlighted the benefit of applying ionospheric corrections to improve solution accuracy. Using ionospheric corrections for single-frequency GPS data from a Continuously Operating Reference Stations (CORS) network, Odijk et al. (2011) showed that PPP-RTK integer ambiguity resolution is feasible using a low-cost receiver. Banville et al. (2014) also showed that the convergence period of PPP can be reduced with GIM while resolving ambiguities. The level of improvement in convergence seen in the horizontal components was nearly 50% as compared to resolving ambiguities alone without using ionospheric corrections from GIM.

The goal of this study is to answer the question concerning the level of significance of any improvement noticed with atmospheric parameter estimation

versus using a priori atmospheric knowledge. Some of the related questions intended to be answered include: (1) Is there any equivalence or differences between combined and uncombined PPP approaches for dual- and triple-frequency measurement processing? (2) Is atmospheric constrained, uncombined, multi-GNSS PPP nearly comparable to the RTK approach? And (3) In terms of solution accuracy and convergence, currently how far away are we from RTK performance?

3.2 Overview of combined and uncombined multi-GNSS PPP

Uncombined PPP processing, based on raw observations, is gradually becoming the norm as an alternative to iono-free (combined) PPP solutions. The advantages it provides include flexibility in processing current and future GNSS constellations, while avoiding noise amplification from linear combinations. The resultant benefit is the ability to extract the ionospheric delays. Using GPS only in PPP processing, the use of raw measurements has been shown to have better performance in positioning and atmospheric modelling (Zhang et al. 2011, 2013). A single-frequency model was also proposed by Shi et al. (2012) to improve the estimation of ionospheric delays in PPP processing. A general GPS/GLONASS/BeiDou/Galileo model was presented by Lou et al. (2016) for PPP single- and dual-frequency processing using raw measurements and using GIM as an a priori constraint. Furthermore, PPP-RTK models which are based on uncombined raw measurements have been analyzed with respect to parameter estimation in a network (Teunissen et al. 2010; Zhang et al. 2011; Odijk

et al. 2016). Thus, there is an apparent move towards standardization of the uncombined PPP approach in multi-GNSS processing. However, it must be pointed out that there is limited research regarding this approach and hence it deserves further probing. Shown in equation 3.1 and 3.2 are simplified uncombined raw measurement functional model representations with respect to a satellite m and a receiver n.

$$P_{L_i}^{mn} = \rho^{mn} + \partial t^m - \partial t^n + M_w^{mn} ZPD^m + I_{L_i}^{mn} - b_{L_i}^m + b_{L_i}^n + \varepsilon\left(P_{L_i}^{mn}\right) \qquad 3.1$$

$$\varphi_{L_i}^{mn} = \rho^{mn} + \partial t^m - \partial t^n + M_w^{mn} ZPD^m - I_{L_i}^{mn} - \frac{c}{f_{Li}} N_{Li} + \varepsilon\left(\varphi_{L_i}^{mn}\right) \qquad 3.2$$

where

$P_{L_i}^{mn}, \varphi_{L_i}^{mn}$	Pseudorange and carrier-phase observations, respectively, from satellite m to receiver n.
ρ^{mn}	Geometric range between the satellite and receiver antennas.
$\partial t^m, \partial t^n$	Receiver and satellite clock errors, respectively, in seconds.
$M_w^{mn} ZPD^m$	Tropospheric zenith path delay scaled by mapping function.
$I_{L_i}^{mn}$	Slant ionospheric delay on GNSS signal.
c	Speed of light.
N_{Li}	Carrier-phase ambiguity including satellite and receiver phase instrumental delays and initial fractional phase bias.

$b_{L_i}^m, b_{L_i}^n$ Satellite and receiver instrumental delays due to the transmitting and receiving hardware, respectively.

$\varepsilon\left(P_{L_i}^{mn}\right), \varepsilon\left(\varphi_{L_i}^{mn}\right)$ Combination of observation noise and multipath effect for pseudorange and carrier-phase observations, respectively.

Considering a least squares solution, presenting the functional model in an uncombined representation allows for scalability and is user intuitive. Though the use of combined measurements presents simplicity in the design of filters, from the software development point of view, it is beneficial to have options for both modes of data processing. Presented in equations 3.3 and 3.4 are the transformation matrices that can be used to transform measurements between combined and uncombined representations, considering two frequencies f_1 and f_2.

From uncombined to combined:

$$\begin{bmatrix} P_{IF}^{mn} \\ \varphi_{IF}^{mn} \end{bmatrix} = \begin{bmatrix} \frac{\mu_2}{\mu_2 - \mu_1} & \frac{-\mu_2}{\mu_2 - \mu_1} & 0 & 0 \\ 0 & 0 & \frac{\mu_2}{\mu_2 - \mu_1} & \frac{-\mu_2}{\mu_2 - \mu_1} \end{bmatrix} \begin{bmatrix} P_1^{mn} \\ P_2^{mn} \\ \varphi_1^{mn} \\ \varphi_2^{mn} \end{bmatrix} \quad 3.3$$

Where μ_i is the frequency dependent coefficient, given as $\mu_i = \frac{f_1^2}{f_i^2}$.

From combined to uncombined:

$$\begin{bmatrix} P_1^{mn} \\ P_2^{mn} \\ \varphi_1^{mn} \\ \varphi_2^{mn} \end{bmatrix} = \begin{bmatrix} \frac{f_1 - f_2}{f_1} & 0 \\ 0 & \\ -\frac{f_1 - f_2}{f_2} & \frac{f_1 + f_2}{f_1} \\ 0 & \frac{f_1 + f_2}{f_2} \end{bmatrix} \begin{bmatrix} P_{IF}^{mn} \\ \varphi_{IF}^{mn} \end{bmatrix} \qquad 3.4$$

The above representations can easily be expanded to include as many frequencies as needed. The analyses presented for subsequent sections involves both dual- and triple-frequency measurements in both combined and uncombined modes of processing. Hence, there was the need for the York PPP engine to be expanded to include uncombined triple-frequency parametrization. Equation 3.5 presents a simplified representation of the triple-frequency parametrization for uncombined multi-GNSS measurements.

$$\begin{bmatrix} P_1^{mn} \\ P_2^{mn} \\ P_3^{mn} \\ \varphi_1^{mn} \\ \varphi_2^{mn} \\ \varphi_3^{mn} \end{bmatrix} = \begin{bmatrix} \overbrace{1 \quad 1}^{Receiver} & & \overbrace{\qquad\qquad\qquad\qquad}^{Satellite} \\ 1 \quad 1 & 1 & \mu_1 \\ 1 \quad 1 & 1 & \mu_2 \\ 1 \quad 1 & 1 & \mu_3 \\ 1 \quad 1 & 1 & -\mu_1 \quad 1 \\ 1 \quad 1 & 1 & -\mu_2 \quad\quad 1 \\ 1 \quad 1 & \underbrace{1}_{Constellation} & -\mu_3 \quad\quad\quad 1 \end{bmatrix} \begin{bmatrix} \rho^{mn} \\ ZPD^m \\ dt^m \\ \delta t^n \\ I_i^{mn} \\ \lambda_1 N_i \\ \lambda_2 N_i \\ \lambda_3 N_i \end{bmatrix} \qquad 3.5$$

Where $\lambda_i = \frac{c}{f_i}$

By linearizing the observations equations presented compactly in equation 3.5 around the a priori parameters and observations, it becomes the matrix form of equation 1.3 (see Chapter 1).

3.3 Combined and uncombined multi-GNSS PPP analysis: Dual- and Triple-frequency processing.

As already discussed, the key advantage for uncombining the raw measurements in PPP is to gain access to the ionospheric delay. This distinction is important because it offers an avenue to re-initialize the solution in the event of possible data gaps and cycle-slips and offers the chance to tighten up the convergence threshold through ionospheric constraining. With respect to satellite geometry, there is no added advantage of the uncombined over the combined approach either in dual- or triple-frequency measurement processing because there is no change in the number of satellites or the satellite geometry.

Presented in Figure 3.1 is the horizontal and vertical positioning error components for station NNOR in Australia detailing the similarity in terms of positioning accuracy between the uncombined and combined dual- and triple-frequency measurement processing. The point of how equivalent the two measurement processing approaches are, is further reinforced in Table 3.1 with the rms of the site processing. It can be observed that the difference between the combined and

uncombined measurement processing for both dual- and triple-frequency PPP was just a few millimetres.

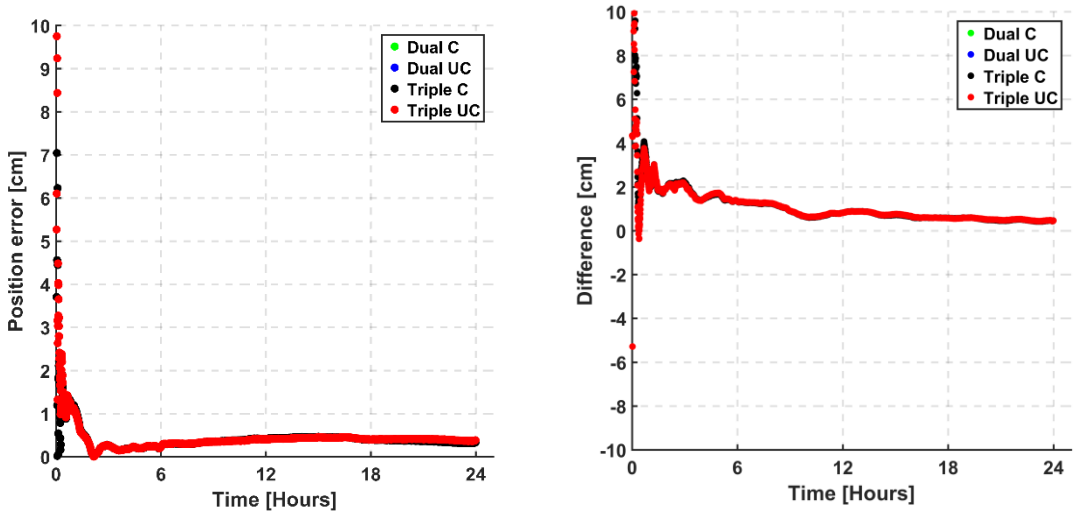

(a) (b)

Figure 3.1: Site NNOR DOY 32 of 2016 located in Australia, illustrating (a) horizontal and (b) vertical components for (1) Dual-frequency combined – "Dual C"; (2) Dual-frequency uncombined – "Dual UC"; (3) Triple-frequency combined – "Triple C"; and (4) Triple-frequency uncombined – Triple UC".

	Combined		Uncombined	
rms (mm)	**Dual**	**Triple**	**Dual**	**Triple**
Horizontal	9	9	5	5
3D	10	10	7	7

Table 3.1: Statistics of dual- and triple-frequency float PPP solutions for the site NNOR in 2016 for DOY 32 for both combined and uncombined PPP processing.

The site NNOR was selected because its results reflect the average results seen for all other stations processed. Post-processed orbits and clock products obtained from the Multi-GNSS Experiment (MGEX) campaign were used (Rizos et al. 2013). In the dual-frequency combined PPP case, the standard L1/L2, E1/E2, B2/B3 ionosphere-free linear combinations were formed for GPS, Galileo and BeiDou satellite systems, respectively. Ionosphere-free linear combinations were formed for L1/L5, E1/E5 and B2/B3 signals in the triple-frequency case for GPS, Galileo and BeiDou satellite systems, respectively. As graphically observed in Figure 3.1, the combined and uncombined approaches for both dual- and triple-frequency measurements processing are identical.

The key point to note is how similar the approaches are in terms of the behaviour of the horizontal and vertical components. As shown in Figure 3.1, the combined and uncombined dual-frequency PPP results align well with the triple-frequency combined at the centimetre level of accuracy. This similarity is expected given that both the combined and uncombined are mathematically meant to produce similar results without the estimation or elimination of additional biases or errors.

Shown in Figure 3.2 and Table 3.2 are the residuals for both dual- and triple-frequency PPP float solutions and statistics, respectively, for the site NNOR processing. Results shown here are meant to be a comparison of both the combined and uncombined approaches in measurement processing.

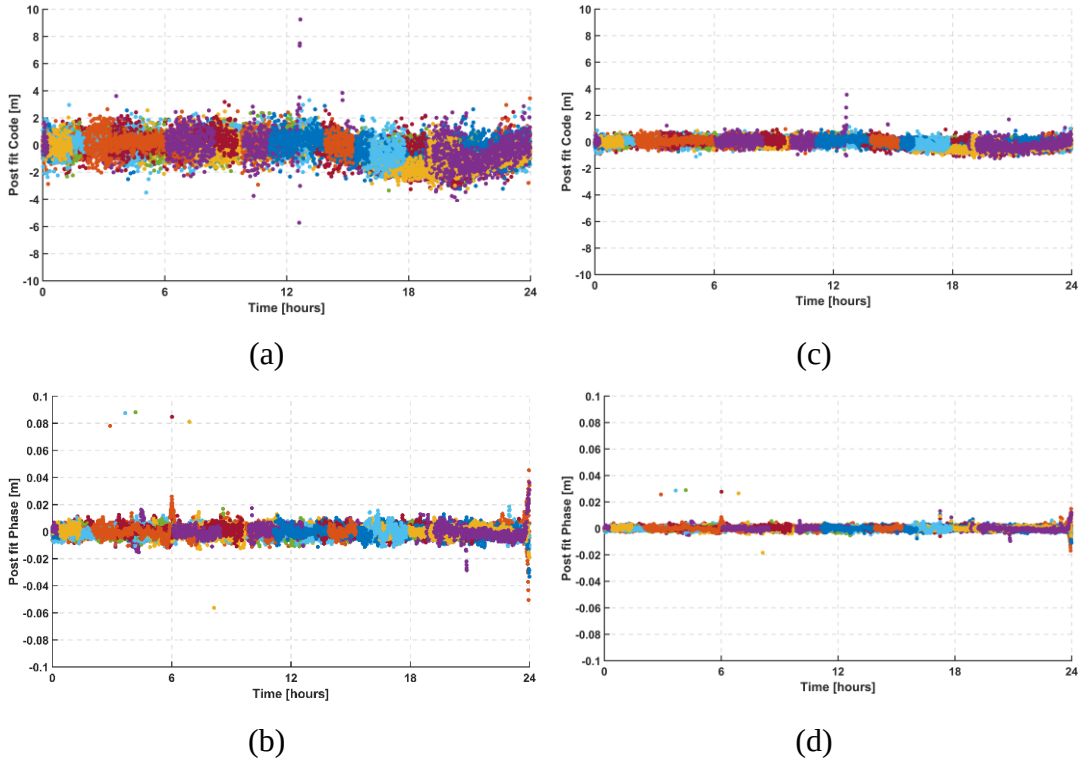

Figure 3.2: Pseudorange and carrier-phase post-fit residuals for NNOR in 2016 for DOY 32. Results are shown for dual combined (figures 2a, b) and dual uncombined (figures 2c, d).

	Combined		Uncombined	
	Pseudorange	**Carrier-phase**	**Pseudorange**	**Carrier-phase**
rms (cm)	68.8	0.4	22.9	0.2

Table 3.2: Pseudorange and carrier-phase post-fit residuals (in cm) for NNOR in 2016 for DOY 32. Results are shown for both combined and uncombined dual-frequency measurement processing.

As presented in Figure 3.2, the residual characteristics for dual-combined as well as implied triple-combined measurement processing approaches are similar due to the

linear combination of the measurements coupled with the amplification of the noise. Triple-frequency residuals are not shown here because they are similar to the dual-frequency case. Similarly, dual- and triple-uncombined are quite indicative of the benefit of uncombining the raw measurements. The noise in the uncombined residuals as shown in Figure 3.2c and Figure 3.2d is reduced as compared to the combined approach in Figure 3.2a and b. This reduction is because the formation of linear ionospheric combinations in the combined approach amplifies the noise. However, this noise amplification is not observed in the uncombined approach given there is no need for linear combinations. In summary, from the perspective of position accuracy, both combined and uncombined modes are equivalent but the uncombined provides an added advantage of less noisy residual characteristics.

3.4 **Overview of Global Ionospheric Maps**

Ionospheric delay models are generated from dual-frequency GNSS observations made with terrestrial networks which are beneficial for both ionosphere study and precise GNSS positioning. Using regional or global scales of network stations, ionosphere delay models can be generated which are dependent and correspond to the scope of coverage of the reference networks. A Global Ionospheric Map (GIM) is a typical example and is in the form of spherical harmonic coefficients presented in IONsphere map EXchange (IONEX) format (Schaer et al. 1998). The assumption made is that the electronic density of the atmosphere is concentrated in an

infinitesimally thin atmospheric layer at a fixed height, usually around 350 km, in the global model recovery. With respect to this assumption, the slant ionospheric delays generated from GNSS observations, are expressed by a combination of the vertical total electronic content (VTEC) and a mapping function. The estimations of the coefficients of the spherical harmonic function are used to represent the VTEC (Schaer et al. 1998). The VTEC is mapped to obtain the slant ionospheric delay through a mapping function.

Daily TEC values are provided in the IONEX format ranging from +87.5° to -87.5° in latitude with a spatial resolution of 2.5°. The longitude grid points range from -180° to +180° with a resolution of 5°. On a daily basis, there is a total of 13 TEC maps available with a temporal resolution of 2 hours (Wienia 2008). Given that 1 total electron content unit (TECU) corresponds to 0.163 m range error for a C/A code, the GIM model has an accuracy of 2 – 8 TECU. Using GIM, an accuracy of 2 TECU at grid points can be achieved (Øvstedal 2002; Chen and Gao 2005).

To compute the slant ionospheric delay with respect to a station, various computations have to be done. The sub-ionospheric point must be calculated first since the satellites are observed in the slant direction. It must be noted that the point of interest for which a TEC value is to be estimated is not the location of the receiver, but the location of the sub-ionospheric point as shown in Figure 3.3.

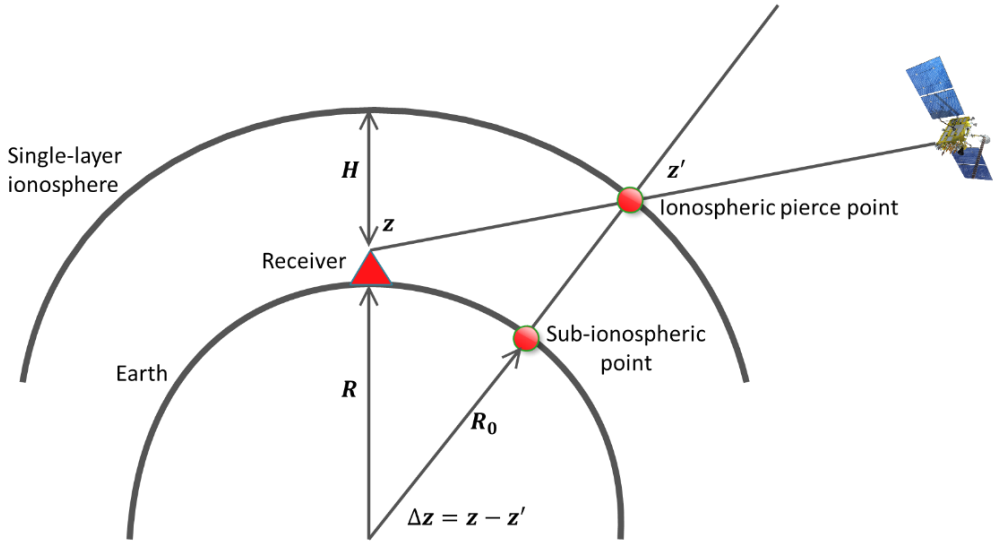

Figure 3.3: Single-layer model (Wienia 2008)

The Ionospheric Pierce point (IPPs) is defined as the intersection of the satellite-receiver line of sight and shell at a given local time. The geocentric spherical coordinates (ϕ, λ) of the sub-ionospheric point can be calculated from the known station coordinates as:

$$\sin z' = \frac{R}{(R+H)} sinz \qquad 3.6$$

$$\emptyset = \sin^{-1}(\sin \emptyset_r \cos(\Delta z) + \cos \emptyset_r + \cos \emptyset_r \sin(\Delta z) \cos \alpha) \qquad 3.7$$

$$\lambda = \lambda_r + \sin^{-1}\left(\frac{\sin(\Delta z) \sin \alpha}{\sin \phi}\right) \qquad 3.8$$

Where

Δz	Spherical distance at the height of the receiver and IPP.
$\emptyset_r$	Receiver latitude.

λ_r	Receiver longitude.
α, z	Azimuth and zenith of the receiver, respectively.

To obtain the TEC value at the user location and time, TEC values are interpolated both in space and time. A 4-point bilinear interpolation is recommended for space while a linear interpolation between two consecutive TEC maps is also recommended for time (Schaer et al. 1998). The VTEC at the sub-ionospheric point (ϕ, λ) and at a universal time *t* can computed as:

$$TEC(\phi, \lambda, t) = \frac{T_{i+1} - t}{T_{i+1} - T_i} TEC(\phi, \lambda, T_i) + \frac{t - T_i}{T_{i+1} - T_i} TEC(\phi, \lambda, T_{i+1}) \qquad 3.9$$

where $T_i \leq t \leq T_{i+1}$

TEC values are provided along the ray path (slant TEC). Given that VTEC is the parameter of interest, an elevation dependent mapping function $F(z)$ is defined, which describes the ratio between the slant TEC and the VTEC required.

$$slantTEC = F(z)VTEC \qquad 3.10$$

where $F(z) = \frac{1}{\sqrt{1 - sin^2 z'}}$

3.4.1 Existing GIM products

The Earth's ionospheric activity has been monitored over the years using mostly GPS, because it offers global coverage, continuity of time, high temporal resolution and low operational cost for geoscience applications (Jin et al. 2006;

Hernández-Pajares et al. 2011). Public services have been set up for monitoring the ionospheric total electron content (TEC) by various Analysis Centers (ACs) such as Centre for Orbit Determination in Europe (CODE), Jet Propulsion Laboratory (JPL), European Space Agency (ESA), and Polytechnic University of Catalonia (UPC). However, there is no uniformity in approaches in the computation of GIM among the ACs (Mannucci et al. 1998). With GLONASS full operational capability and global coverage, ionospheric monitoring capability is further enhanced. It is expected that with Galileo's anticipated 30-satellite constellation and BeiDou's increasing number of satellites, many more ionospheric pierce points will be provided. These future enhancements promise better spatial coverage using denser multi-GNSS observations and improved ionospheric models.

Over the past two decades, VTEC estimates and their associated rms estimates, have been provided, originally for meteorological purposes, to the GNSS community through GIMs. As part of the estimation process, satellite and receiver differential code biases (DCBs)with their rms values, are provided as a by-product. An average of 21 GIM products currently exist. These products are either post-processed, predicted or combined from other ACs and generated from dual-frequency GNSS measurements. Shown in Table 3.3 are the unique current products available to GNSS users. Of interest is the varying numbers of receiver stations and GNSSs used in the generation of the products.

Product	Agency	Type of product	# sites	# satellites	GNSS	Mapping function
c1pg	AIUB	1-day predicted	~120	~56	*GNSS	NONE
c2pg	AIUB	2-day predicted	~120	~56	*GNSS	NONE
carg	AOE	Post-processed (R)	--	--	*MIX	COSZ
casg	AOE	Post-processed (F)	--	--	*MIX	COSZ
codg	AIUB	Post-processed (F)	~259	~56	*GNSS	NONE
corg	AIUB	Post-processed (R)	~118	~55	*GNSS	NONE
e1pg	ESA/ESOC	1-day predicted	--	--	GPS	NONE
e2pg	ESA/ESOC	1-day predicted	--	--	GPS	NONE
ehrg	ESA/ESOC	Post-processed (R)	~231	~54	GPS	NONE
emrg	NRCAN	Post-processed (R)	~351	~29	GPS	MOD
esag	ESA/ESOC	Post-processed (F)	~300	~54	GPS	NONE
esrg	ESA/ESOC	Post-processed (F)	~236	~54	GPS	NONE
igrg	IGS	Post-processed (CR)	~296	0	*MIX	COSZ
igsg	IGS	Post-processed (CF)	~328	~32	*MIX	COSZ
jplg	JPL	Post-processed (F)	~170	~31	GPS	NONE
jprg	JPL	Post-processed (R)	~170	~31	GPS	NONE
u2pg	UPC	Predicted	--	--	GPS	NONE
uhrg	UPC	Post-processed (R)	~259	~31	*MIX	COSZ
upcg	UPC	Post-processed (F)	~272	~31	GPS	NONE
uprg	UPC	Post-processed (R)	~272	~31	GPS	NONE
uqrg	UPC	Post-processed (R)	~255	~31	GPS	COSZ
whug	WHU	Post-processed (F)	~314	~31	GPS	MSLM
*MIX / *GNSS = GPS and GLONASS satellites						

R = rapid, F = final, CR = combined rapid, CF = combined final

Table 3.3: Different existing GIM products available to the PPP user from different ACs (Aggrey 2018).

3.4.2 Methods of GIM constraint application

Though not a novel concept, it is well known that constraining an estimable parameter to a known value in least squares or Kalman filter might aid in the optimization of the estimated solution. Applying atmospheric constraints functionally implies fixing the atmospheric parameters in the functional pseudorange and carrier-phase models. Equation 3.11 and 3.12 illustrate the well-known models with the parameters to be constrained:

$$P_{L_i}^{mn} = \rho^{mn} + \partial t^m - \partial t^n + M_w^{mn} ZPD^m + I_{L_{i,constrained}}^{mn} + \varepsilon\left(P_{L_i}^{mn}\right) \qquad 3.11$$

$$\varphi_{L_i}^{mn} = \rho^{mn} + \partial t^m - \partial t^n + M_w^{mn} ZPD^m - I_{L_{i,constrained}}^{mn} - \frac{c}{f_{Li}} N_{Li} + \varepsilon\left(\varphi_{L_i}^{mn}\right) \qquad 3.12$$

where

$P_{L_i}^{mn}, \varphi_{L_i}^{mn}$ Pseudorange and carrier-phase observations from satellite (m) to receiver (n), respectively.

ρ^{mn} Geometric range between the satellite and receiver antennas.

$\partial t^m, \partial t^n$	Receiver and satellite clock errors, respectively.
$M_w^{mn} ZPD^m$	Tropospheric zenith path delay scaled by mapping function.
$I_{L_{i,constrained}}^{mn}$	Constrained ionospheric delay on the GNSS signal propagated.
N_{Li}	Carrier-phase ambiguity including satellite and receiver phase instrumental delays and initial fractional phase bias
$\varepsilon\left(P_{L_i}^{mn}\right), \varepsilon\left(\varphi_{L_i}^{mn}\right)$	Combination of observation noise, satellite and receiver instrumental delays due to the transmitting and receiving hardware, multipath and unmodelled effects, respectively.

By constraining atmospheric parameters in the functional models, the partial derivatives of these parameters, represented by the design matrix, must be deleted. Though this action eliminates the need to estimate the constrained parameters by using atmospheric products, there is the potential of residual bias in the solution due to time correlated errors.

An easier option presents itself through stochastic constraints. Using the ionospheric delay estimates, as well as their uncertainties provided in the atmospheric products, the covariance matrix can be adjusted to constrain the atmospheric parameters. It is key to note that there is no need to constrain every epoch given the potential of propagating time correlated errors. By constraining only the first epoch

and "freeing" up the process noise to allow the filter to continue estimating the atmospheric parameters, the constraint initially applied should have a beneficial effect in the first few epochs, improving the solution accuracy in PPP processing. In a sequential least-squares implementation, updating and propagating the covariance information, $C\hat{x}$, in the first epoch requires the inclusion of appropriate process noise, $C\varepsilon_{\Delta t}$, assuming a time interval of Δt. This process can be represented by:

$$Px^0 = [C\hat{x} + C\varepsilon_{\Delta t}]^{-1} \tag{3.13}$$

$C\hat{x}$, representing a priori variance-covariance matrix, is given by:

$$C\hat{x} = \begin{bmatrix} \sigma_x^2 & & & & & & \\ & \sigma_y^2 & & & & & \\ & & \sigma_z^2 & & & & \\ & & & \ddots & & & \\ & & & & \sigma_{ZPD}^2 & & \\ & & & & & \ddots & \\ & & & & & & \sigma_{iono,constrained}^2 \end{bmatrix} \tag{3.14}$$

$C\varepsilon_{\Delta t}$, defined as the process noise covariance matrix, is also given by:

$$C\varepsilon_{\Delta t} = \begin{bmatrix} C\varepsilon(x)_{\Delta t} & & & & & & \\ & C\varepsilon(y)_{\Delta t} & & & & & \\ & & C\varepsilon(z)_{\Delta t} & & & & \\ & & & \ddots & & & \\ & & & & C\varepsilon(ZPD)_{\Delta t} & & \\ & & & & & \ddots & \\ & & & & & & C\varepsilon(iono)_{\Delta t,constrained} \end{bmatrix} \tag{3.15}$$

It is imperative to note that the choice of process noise value, as well as atmospheric constraint uncertainty, affects the effectiveness of the filtered solution in the first epochs of processing. To avoid the case of over-constraining, the uncertainties of the GIM delays should be inflated to accommodate any inherent errors in the generation of these ionospheric delays. Concurrently, and in the same vein, it is necessary to choose an appropriate process noise which does not dilute the impact of the uncertainties used as constraints. In other words, a large process noise could lead to under-constraining, while a small process noise value potentially over-constrains depending on the GIM delay uncertainty.

3.5 Impact of GIM constraints in multi-GNSS PPP

To investigate the impact of GIM in multi-GNSS PPP processing in both dual- and triple-frequency uncombined approach, 70 global multi-GNSS stations were selected for processing to find probable answers and arrive at logical conclusions. Figure 3.4 shows the global distribution of the 70 stations selected for the experiment.

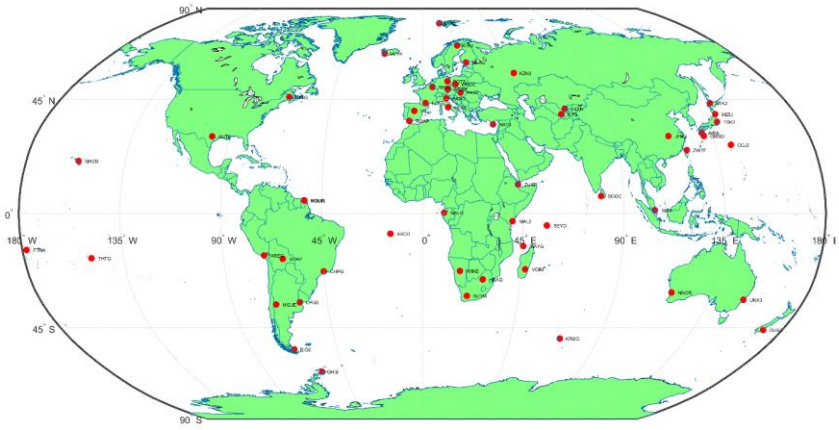

Figure 3.4: Map of globally distributed stations

Figure 3.5 to Figure 3.8 show the first hour of 24-hourly horizontal errors for the 70 stations for 4 different processing modes. The solutions presented are based on GPS + GLONASS + Galileo + BeiDou (GREC). The GIM product used for constraining was IGSG (see Table 3.3) due to its availability for all the days of processing considered. The scenarios processed include (a) Dual GREC PPP (b) Dual GIM constrained GREC PPP (c) Triple GREC PPP and (d) Triple GIM constrained GREC PPP. Also shown are the 68th percentiles for all the processing scenarios. A tight convergence is defined as solutions reaching a horizontal error of 10 cm under 12 minutes, as represented by the black dashed lines. The 68th percentiles therefore represent the percentage of solutions that have 10 cm horizontal error or lower, given the tight convergence threshold defined. It must be noted that only sample solution time series are presented in Figure 3.5 to Figure 3.8 as black lines and does not depict all of the 70 stations processed.

Figure 3.6 and Figure 3.8 demonstrate how the solutions are affected by the influence of ionospheric constraint application in float solutions. It must be noted that the application of ionospheric constraints using GIM generally helps in the first few epochs by reducing the positional errors. The idea is to fast track convergence and quicker initialization by informing the filter with better slant ionospheric information, as explained in the previous section. However, even with the use of GIM as a priori ionospheric information, the filtered positional estimates in the first few epochs are greatly dependent on the pseudorange measurements, which potentially minimizes the efficacy of GIM due to the metre level noise on the pseudoranges. In a float solution case, the solution is further improved through using multi-GNSS measurements in the processing, which helps reduce convergence.

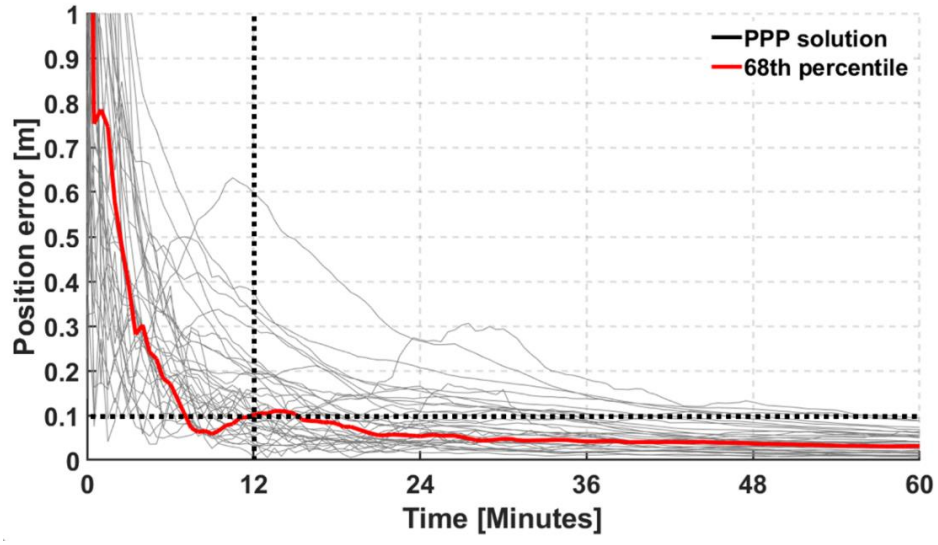

Figure 3.5: Horizontal positional error (hourly) based on 24 hourly solutions for 70 stations for Dual GREC processing mode.

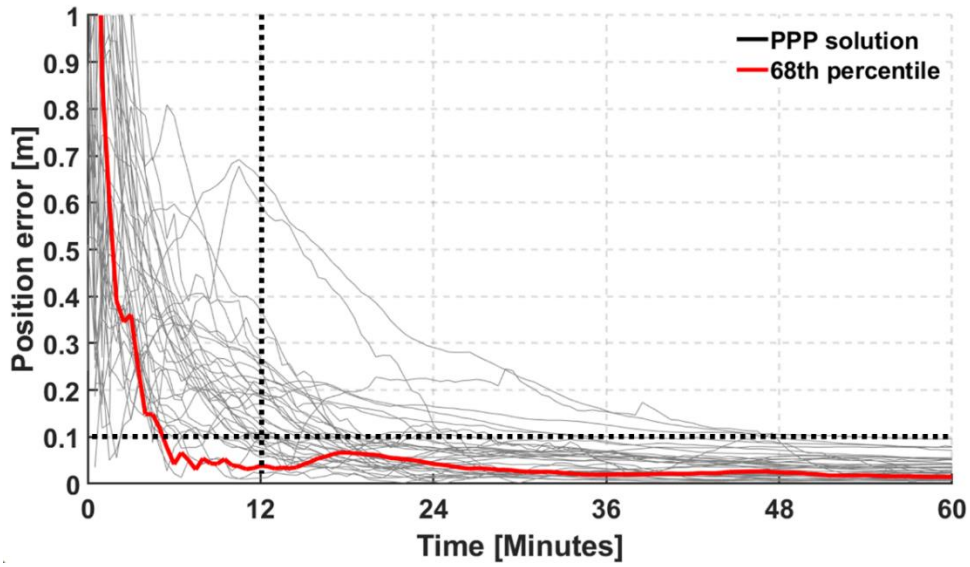

Figure 3.6: Horizontal positional error (hourly) based on 24 hourly solutions for 70 stations for Dual + GIM GREC processing mode.

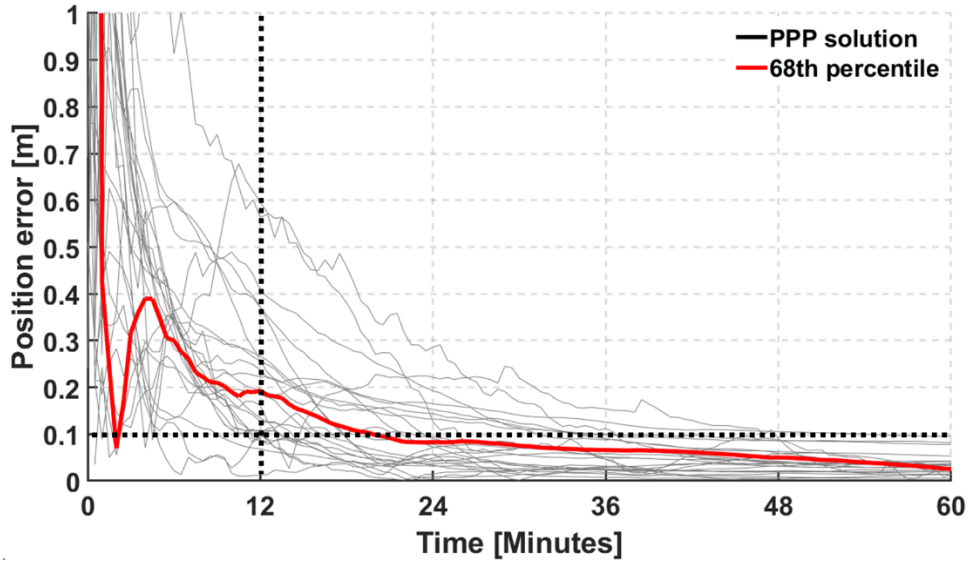

Figure 3.7: Horizontal positional error (hourly) based on 24 hourly solutions for 70 stations for Triple GREC processing mode.

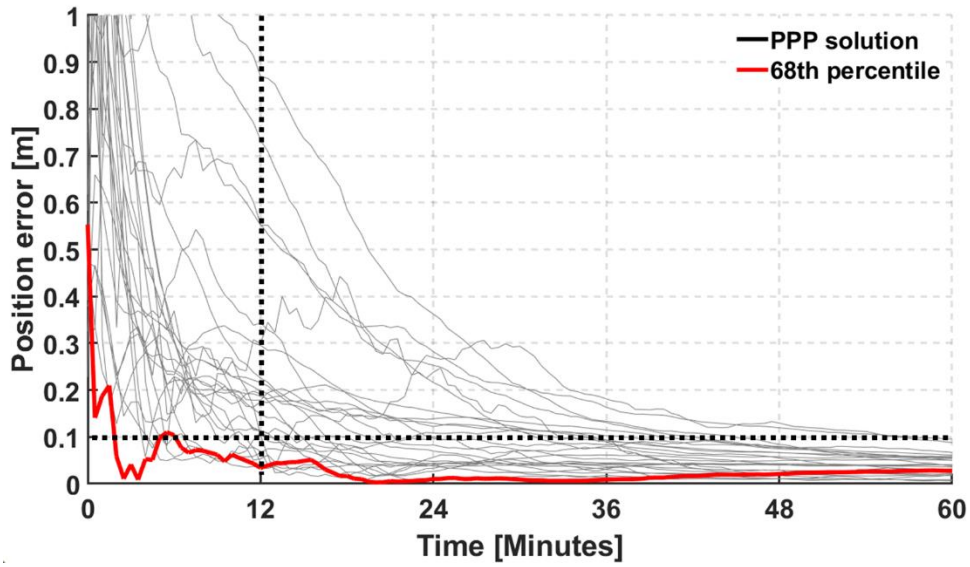

Figure 3.8: Horizontal positional error (hourly) based on 24 hourly solutions for 70 stations for Triple + GIM GREC processing mode.

The 68th percentiles for dual and triple GIM constrained GREC PPP showed quicker convergence under 10 cm horizontal error in 12 minutes as compared to dual- and triple-frequency unconstrained PPP. The kinks observed in the first few minutes of the time series in Figure 3.7 and Figure 3.8 corresponded to poor satellite geometry and reduced number of processed satellites due to residual rejection. Table 3.4 shows the convergence times for dual- and triple-frequency PPP processing with and without the application of GIM for the 68th percentiles of the solutions. Convergence was greatly reduced by 9 and 14 minutes for dual- and triple-frequency PPP solutions with GIM application, respectively. To put these results into perspective, Zhang et al. (2013) investigated ionospheric constraining with the application of IGS GIM and reduced PPP convergence from 16 to 11 minutes, considering dual-frequency data

processing. As shown in Table 3.4, the dual-frequency multi-GNSS PPP analysis with GIM ionospheric constraints showed an improvement in convergence time from 15 to 6 minutes. The triple-frequency PPP convergence showed a significant reduction of convergence to 4 minutes.

	Convergence time (minutes)	
	Dual-frequency	**Triple-frequency**
Without GIM	15	18
With GIM	6	4

Table 3.4: Convergence times for dual- and triple-frequency PPP processing with and without GIM applications for 68th percentile of the solutions.

Figure 3.9, Figure 3.10 and Figure 3.11 show the results for dual- and triple-frequency float PPP solutions of the 70 stations with and without the application of GIM ionospheric delay constraining in an uncombined measurement processing mode. GIM was used in providing a priori ionospheric delays to aid in the improvement of convergence. Results shown in the figures are for the horizontal components. To show the effect of the constraint, three initialization periods were analysed: 5, 10 and 15 minutes. The criteria for the thresholds were chosen to reflect the convergence of the horizontal components to under 10 cm.

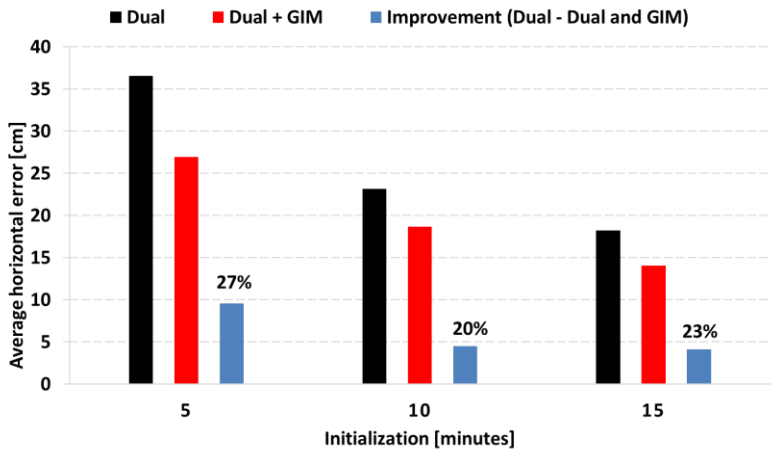

Figure 3.9: Dual-frequency PPP solutions of 70 stations within a 5, 10 and 15-minute initialization periods with and without GIM constraints. Results for horizontal components are shown.

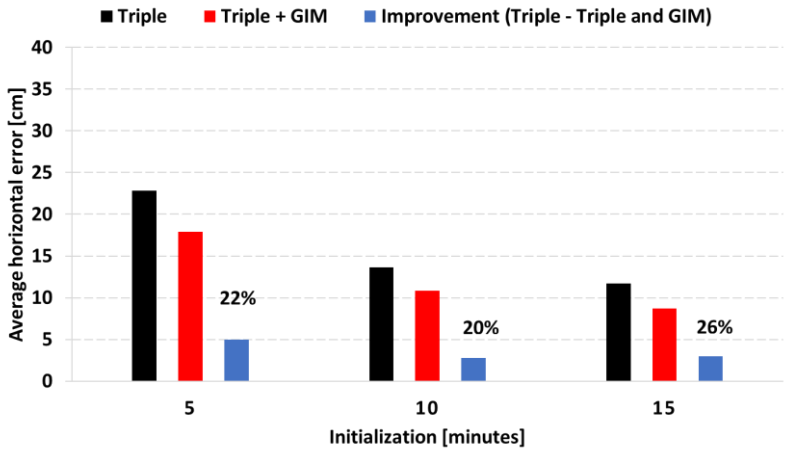

Figure 3.10: Triple-frequency PPP solutions of 70 stations within a 5, 10 and 15-minute initialization periods with and without GIM constraints. Results for horizontal components are shown.

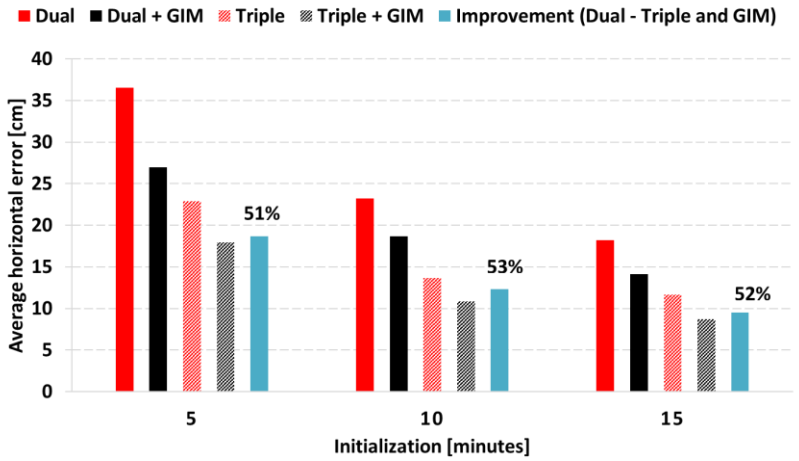

Figure 3.11: Dual- and triple-frequency PPP solutions of 70 stations within a 5, 10 and 15-minute initialization periods with and without GIM constraints. Results for horizontal components are shown.

The results are indicative of the impact GIM has on ionospheric-constrained PPP solutions. As shown in Figure 3.9 and Figure 3.10, there was an average improvement of 27% and 22% when considering initialization periods of 5 minutes. It must be noted that the inherent biases especially for GPS L5 and BeiDou MEO and LEO satellites were not accounted here in order to assess the raw strength of impact of GIM on the solution quality. Considering the poorer quality of BeiDou orbit and clock products, using BeiDou measurements in an uncombined approach does not significantly improve the solution quality. The key significance is the resultant improvement GIM offers to the PPP initialization as evidenced in Figure 3.11. A significant 51% improvement is observed for the first 5 minutes for triple-frequency PPP with GIM

constraints as compared to dual-frequency PPP. 53% and 52% improvement were also observed for the first 10 and 15 minutes, respectively.

3.6 Summary

This chapter presented a unique perspective and analyses in the improvement of PPP convergence and initialization. Various research contributions looked at improving position accuracy of single-frequency PPP solutions with GIM. Novel contributions have been made in this chapter by improving dual- and triple-frequency multi-GNSS PPP with ionospheric corrections used as constraints. The novelty lies in the use of triple-frequency measurements from GPS, Galileo and BeiDou and in the analyses of the results. By constraining the ionosphere with GIM, dual-frequency and triple-frequency PPP solution convergence improved significantly by 60% and 78% when a 10 cm horizontal threshold was considered. Other key research questions were addressed, and these are summarized below:

1. ***Is there any equivalence or differences between combined and uncombined PPP approaches for dual- and triple-frequency measurement processing?***

Results shown in this chapter for combined and uncombined dual- and triple-frequency PPP position accuracy results were equivalent with each other at the millimetre level. This similarity was expected given that both the combined and uncombined were mathematically meant to produce similar results. The key benefit of

the uncombined approach over the combined was observed in the residual analysis. Given there was no need for linear combination of measurements in the uncombined mode, the noise amplification was significantly reduced which was noticeable in the residuals.

2. ***Is atmospheric constrained, uncombined, multi-GNSS PPP nearly comparable to the RTK approach? In terms of solution accuracy and convergence, currently how far away are we from RTK performance?***

An optimistic answer would definitely be yes. However, this response would ignore the significant level of improvement that would be needed to improve PPP solution quality to RTK-like performance. From the issues of slower convergence of PPP to the mitigation of equipment delays, PPP is limited and for that to change would require significant enhancement to PPP algorithms.

The quest to obtain RTK-like performance with PPP has been on-going for years. Though both techniques give high accuracy solutions, RTK takes the lead in terms of solution stability and convergence making it widely used for many high accuracy applications. PPP is currently on a catch-up mission and it is obvious that the technique is gradually making headway. Though RTK achieves instantaneous convergence through the quick resolution of ambiguities, PPP is continuously breaking ground in achieving similar results. Are we there yet? The answer is obviously in the negative. However, it must be pointed out by uncombining the raw measurements, either in dual-

or triple-frequency measurement processing, access is gained to parameters that aid in re-convergence and further assist in getting better solution quality. PPP still has some limitations that are dependent on the quality of the products being used and error mitigation strategies. Will current centimetre level accuracy solutions from PPP get better? The answer depends on enhancing parameterizations and careful accounting of all potential biases in the solutions. We may not be there yet, but we are bridging the gap a few millimetres at a time.

It is concluded that by uncombining and constraining the ionosphere with GIM as a priori information, more than 50% improvement was observed for the first 5, 10 and 15-minute period for triple-frequency PPP in comparison to dual-frequency PPP. This level of improvement is significant for application in which quick convergence is critical. Though results were shown for float solutions, it is expected that by resolving ambiguities, the level of improvement should significantly increase. For future work, it is intended to mitigate time correlated errors to further improve multi-GNSS PPP convergence and initialization. The next chapter further investigates ionospheric constraining while resolving float ambiguities. Further investigations in the next chapter assesses the reliability of ionospheric products considering a sparse network of stations.

CHAPTER 4 LATITUDINAL CORRELATION AND COVERGENCE ANALYSIS OF ATMOSPHERIC PRODUCTS WITH PPP

GNSS positioning performance has been shown to improve with the ingestion of data from Global Ionospheric Maps (GIMs) and tropospheric zenith path delays, which are produced by, e.g., the International GNSS Service (IGS). For both dual- and triple-frequency PPP processing, the significance of GIM and tropospheric products in processing is not obvious in the quality of the solution after a few hours. However, constraining the atmosphere improves PPP initialization and solution convergence in the first few minutes of processing. These constraints and their impact on PPP solutions have been discussed in the previous chapter. However, there are other key research questions that must be addressed which include: (1) What is the impact of different GIM products in multi-GNSS processing? Do all GIM products behave and enhance the solutions at the same rate? (2) By how much do troposphere and ionosphere constraints improve PPP solutions? (3) Is there any regional correlation with respect to GIM products, between the application of the products and PPP solution accuracy? (4) How dense or sparse must a network of stations be when considering regional ionospheric corrections in multi-GNSS PPP? All of these questions have not been explored in relation to PPP, hence the contributions provided

in this chapter provide novelty in the attempt of addressing these key research questions.

4.1 Introduction

Traditionally, the effects of ionospheric and tropospheric refraction are mitigated in the GNSS PPP measurement processing technique using dual- or triple-frequency linear combinations and systematic modelling, respectively (Zumberge et al. 1997; Kouba and Héroux 2001; Urquhart 2009; Henkel and Günther 2010; Li et al. 2016). The purpose of such mitigation hinges on improving PPP convergence and initialization which has been a challenging area of GNSS research. Recent developments and contributions highlight the changing definition of conventional PPP from the use of dual- to triple-frequency measurements. Additional frequencies coupled with expanding satellite constellations have improved reliability and integrity of multi-GNSS PPP solutions (Hofmann-Wellenhof et al. 2007; Elsobeiey and El-Rabbany 2009; Wang and Rothacher 2013; Aggrey and Bisnath 2017b). Thus, the progression towards the improvement of multi-GNSS PPP solution quality and initial convergence is only natural given that measurement strength and satellite geometry are continually being enhanced.

It is well known that by accessing the slant ionospheric information, PPP convergence and initialization can be significantly improved (Odijk 2002, 2003; Cueto

et al. 2007; Rovira-Garcia et al. 2014). The usage of raw observations in uncombined PPP processing is gradually becoming the standard approach as an alternative to ionosphere-free PPP solutions. One key advantage involves the flexibility in processing the observations from all existing GNSS constellations while avoiding noise amplification due to linear combinations (Geng 2010; Teunissen et al. 2010; Zhang et al. 2011; Tu et al. 2017). The consequential benefit is the ability to extract the slant ionospheric delays which can be used to quickly re-initialize the solution. In the context of this chapter, the raw observations from available GNSSs were processed without employing linear combinations to eliminate the first order ionospheric delay, but rather estimated it. Having access to the slant ionospheric terms enabled various analyses to be made in comparison to the a priori ionospheric delays obtained through atmospheric products. For more and detailed information on how to decompose the linear ionospheric combination to its uncombined format in order to estimate the slant ionospheric term, the reader is referred to these research contributions that discusses it at length: (Geng 2010; Collins et al. 2012; Li 2012; Seepersad 2018).

Using a priori estimates from atmospheric products, either from regional or global networks of stations, has shown that it is possible to obtain cm-level accuracy within a few minutes, rather than the typical 20 to 30 minutes of PPP convergence time (Collins and Bisnath 2011; Collins et al. 2012; Yao et al. 2013; Banville 2014; Lou et al. 2016; Liu et al. 2017). Single-frequency ambiguity resolution (AR) has been

a prominent topic demanding innovative solutions due to the relatively long convergence time period (Mervart et al. 2008; Laurichesse et al. 2009; Teunissen et al. 2010; Bertiger et al. 2010). Isolating and resolving ambiguities to integers can be hastened by using a priori atmospheric constraints, which consequentially leads to better accuracy and stability in the position estimates (Geng 2010; Collins and Bisnath 2011; Collins et al. 2012).

The purpose of this study is to use atmospheric constraints with ambiguity resolution and multi-GNSS PPP processing to reduce convergence period. Using RTK performance as the goal, the idea is to compare the improved solutions to RTK accuracy and convergence time. As is well-known, typical RTK performance is correlated and limited to baselines of less than approximately 20 km. Longer baseline lengths prevent certain measurement errors from being effectively cancelled. By mathematically differencing GNSS measurements from multiple receivers, the key objective of relative positioning is to reduce or eliminate error effects. When considering typical RTK positioning performance, the potential delocalization of the ionosphere and troposphere introduces systematic errors which prevents baselines from being extended beyond 20 km if reliable user solutions are to be obtained (Tobias et al. 2011). The scope of this chapter therefore addresses atmospheric constraining in PPP with the aim of improving the solution accuracy and quality.

4.2 **Zenith path delay products**

Using ground-based GNSS information, tropospheric products are generated from IGS ACs. Horizontal gradient components and 5-minute interval estimates of zenith path delay (ZPD) are included in the products. Using over 350 IGS GNSS stations, ZPD estimates are generated and made available daily per site. Precipitable water vapour extracted from estimated ZPDs are included in the products with surface pressure and temperature measurements made at GNSS site locations. Given that the tropospheric products are generated using IGS final satellite orbits and Earth Orientation Parameters (EOP) products, they are therefore available approximately three weeks after the day of observation. Different methodologies are employed in the generation of the IGS combined tropospheric solution which potentially impacts the accuracy of the products. The production and dissemination of these products since inception has been the focus of 3 ACs, namely Jet Propulsion Laboratory (JPL), German Research Centre for Geosciences (GFZ) and United States Naval Observatory (USNO) (Gendt 1998; Schuler 2001; Byun and Bar-Sever 2010; Hackman et al. 2015; Lu et al. 2017; Xu et al. 2018).

Similarly, the ZPDs with standard deviations provided in tropospheric products, can be used in constraining the atmosphere in multi-GNSS PPP solutions. The reason for the addition of a ZPD constraint, considering a sequential least-squares adjustment, is to either improve PPP convergence in the first few minutes or to avoid matrix

inversion singularities, given poor satellite geometry. A fixed ZPD constraint of 20 cm was used for analyses in the results presented for the multi-GNSS PPP processing in this chapter. Given that the ZPD products are made available daily by GNSS site, the choice of a fixed constraint stems from the fact that products were not available for majority of the stations analyzed. Hence, the constraint was empirically chosen based on the consistency of the estimates obtained from the few products made available.

4.3 Ionospheric delay estimation: Slant and GIM delays

A combination of the VTEC and a mapping function express the slant ionospheric delays generated in GIM. The differences between GIM and estimated slant ionospheric delays for particular satellites are depicted in Figure 4.1. As observed in Figure 4.1 (a) to (d), different satellites show metre-level variations between GIM and slant delays in PPP processing, especially within the first few minutes. These observed variations are not only due to different ionospheric estimates but differential code biases as well as unmodelled biases play a major role (Schaer 1999; Øvstedal 2002; Teunissen and Khodabandeh 2015; Nadarajah et al. 2018). These differences were observed to be consistent for all available GNSSs.

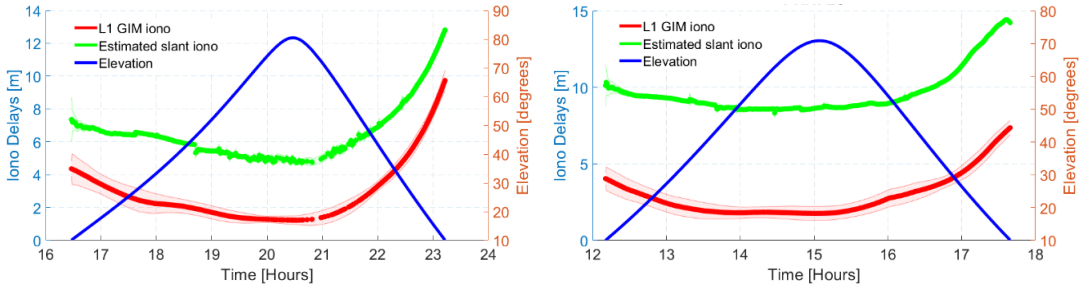

(a) PRN 2 (b) PRN 28

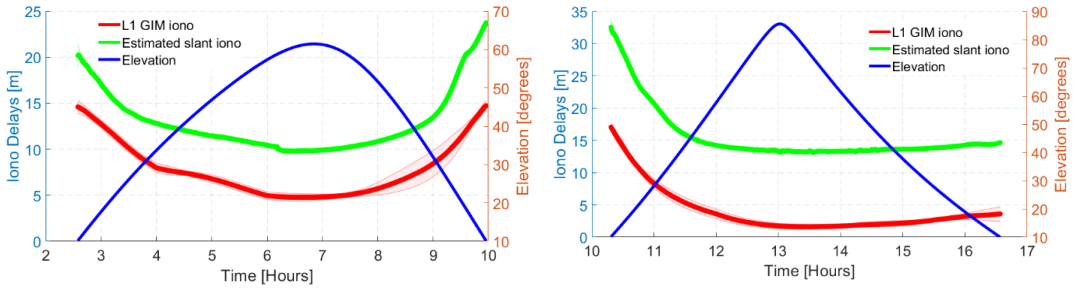

(c) PRN 31 (d) PRN 1

Figure 4.1. Magnitude of L1 GIM and estimated slant ionospheric delays for sample satellites with metre-level variations shown against satellite elevations. Delays are shown for DOY 253, 2018 for GMSD station, located in Japan. Bordered shaded colours represent the uncertainties.

In comparing the GIM and estimated slant delays, a key question presents itself: Considering PPP float and fixed solutions, how precise must the GIM be in order to notice significant improvement in atmospheric constrained solutions? Unfortunately, attempting an answer represents a meander rather than a straight trajectory. Aside from being multi-faceted, the answer is reliant on the method and

models used in the GIM generation (product-wise), how the GIM is used in PPP processing (application-wise), and quality of other GNSS products and observations (quality check). However, there is a level of consistency in the general trend of convergence for both slant and GIM delays. The bordering colours represent the uncertainties of GIM and slant delays, depicting the accuracy of the delays. As expected, given the convergence of the uncertainties of GIM delays, PPP solutions tend to become more optimistic. In the first few minutes, typically, a GIM is beneficial in PPP ionospheric constraining while the noisy pseudorange measurements are the limiting factor in accurately estimating slant ionospheric delays.

Shown in Figure 4.2 and Figure 4.3 are plots of GIM and estimated slant delays with their respective uncertainties. The magnitude of the GIM delays and uncertainties range up to 8 m +/-1 m. This performance is in contrast to the estimated slant delays which ranged up to 10 m +/-0.3 m.

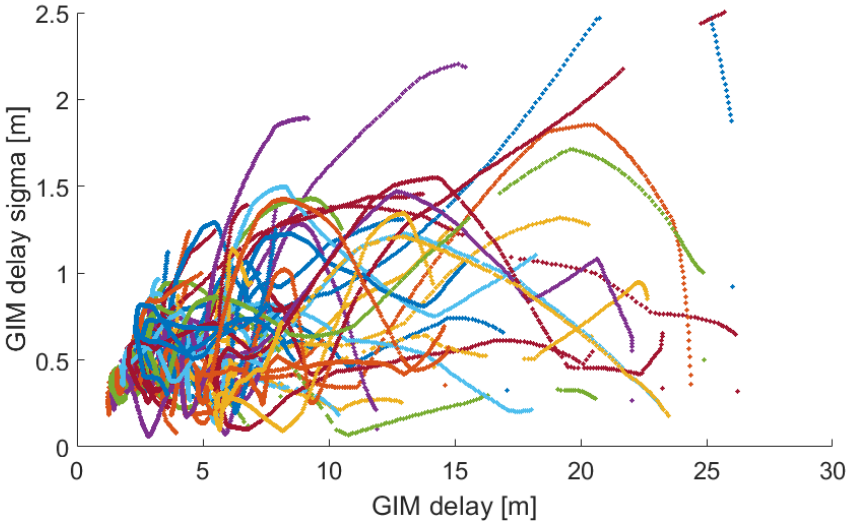

Figure 4.2. GIM delays and their sigmas. Each colour marker point represents a particular satellite. Delays are shown for DOY 253, 2018 for GMSD station, located in Japan.

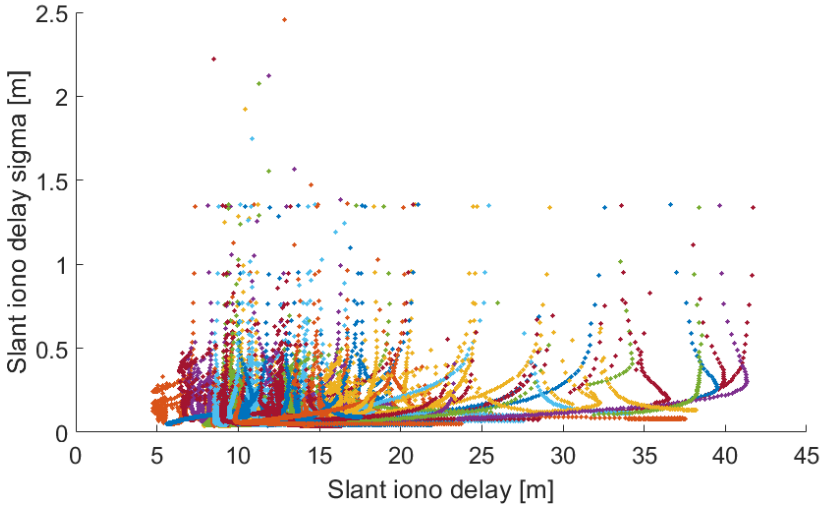

Figure 4.3. Estimated slant delays and their sigmas. Each colour marker point represents a particular satellite. Delays are shown for DOY 253, 2018 for GMSD station, located in Japan.

The pivotal message from these analyses is that the critical minutes during PPP initialization show GIM with realistic ionospheric delays but decimetre-level uncertainties in contrast to the centimetre-level uncertainties for estimated slant delays. The typical slant ionospheric delay is more precise but less accurate, whereas GIM is more accurate but less precise in the first few minutes. This phenomenon elicits the need for an adaptive approach when using either GIM or ZPD product in constraining. The realism of the estimates and uncertainties is key in constraining. Unrealistic estimates and uncertainties could result in either over or under constraining. The observed product / measurement / processing sensitivity prompts urgency for further investigation to achieve an adaptive approach, which will be fully dependent on the GNSS measurements and parameters of the station, rather than just the atmospheric delays and uncertainties.

4.4 Impact of different ionospheric map and tropospheric products on multi-GNSS PPP solutions

To investigate the impact of atmospheric parameter constraints in both dual- and triple-frequency multi-GNSS PPP, ~70 globally distributed MGEX GNSS receiver stations were arbitrarily selected for PPP processing. Figure 4.4 shows the global distribution of stations.

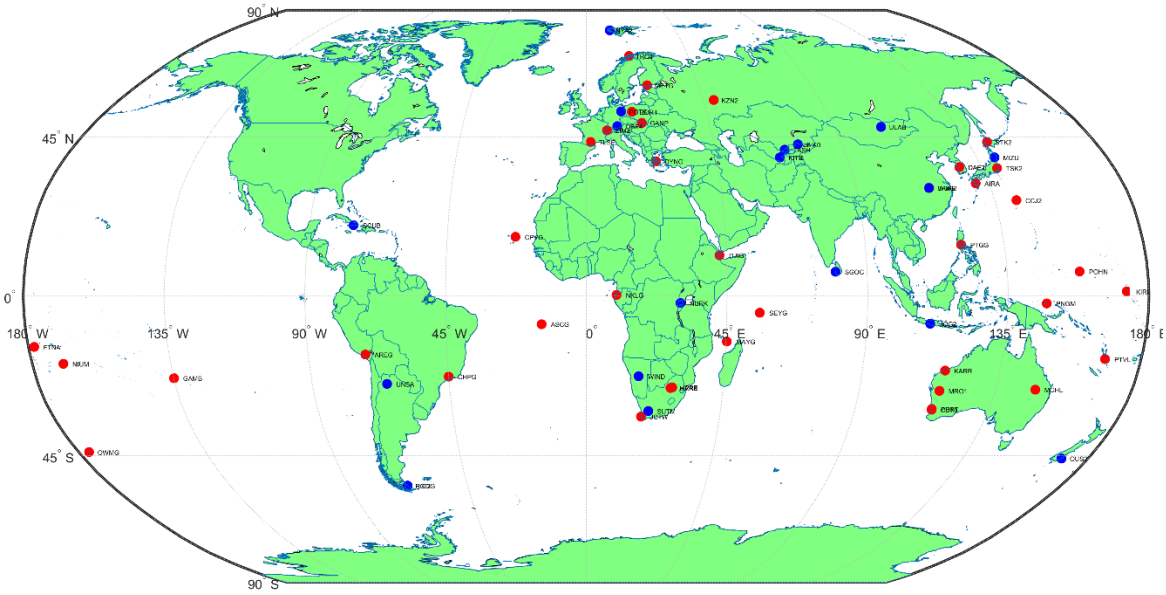

Figure 4.4: Map of global distribution of multi-GNSS stations.

Observations from these stations ranged from DOY 32 to 38 in 2016. To prevent equipment hardware delays impacting the results, the stations were selected based on homogeneity of receiver and antenna types. Table 4.1 shows the number of stations that were grouped between Trimble and Javad receiver and antenna types.

Receiver type	Antenna type	Firmware version(s)	# stations
TRIMBLE NETR9	TRM 59800	4.61, 5.01, 5.1, 5.14, 5.15, 5.2, 5.22, 5.3	44
JAVAD TRE_G3TH DELTA	JAV_RINGANT_G3T	3.6.7	18

Table 4.1: Number of multi-GNSS stations grouped between Trimble and Javad receiver and antenna types.

The locations of these stations are shown in Figure 4.4 with red and blue dots, representing Trimble and Javad receiver stations, respectively. Figure 4.5 shows 1-hour GIM constrained and unconstrained solutions for ALGO station located in Algonquin Park, Canada for DOY 28, 2017. Four flavours of IONEX products were used to assess the performance of GIM constrained solutions in relation to the choice of post-processed or predicted products. The focus was limited to the first initial hour because the benefit of GIM constraining is most noticeable within the first few minutes. Figure 4.5 (a) shows the results when a post-processed product is used. It was observed that there was a 28% improvement in the PPP initialization and convergence as compared to the usage of either predicted products. The 1- and 2-day predicted IONEX products showed an improvement of 8% and 9%, respectively, as compared to the combined product which improved the solution by 30%.

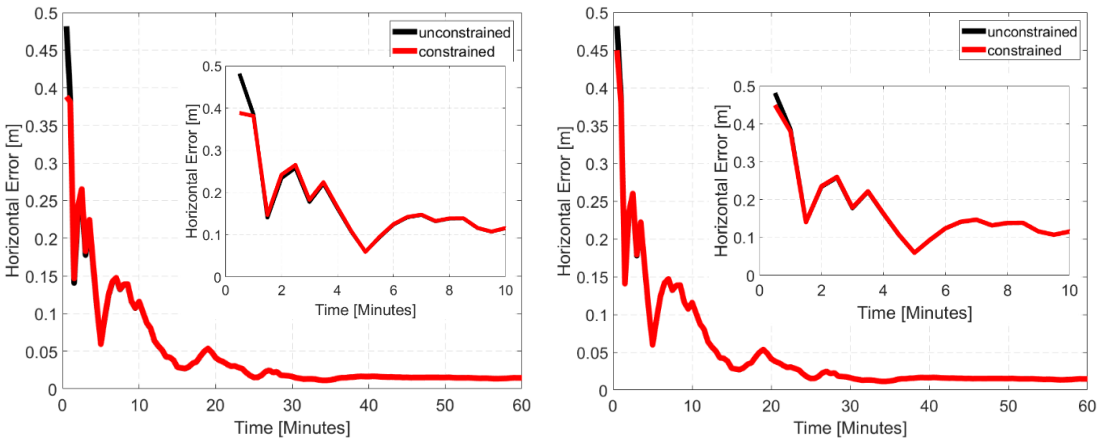

(a) Post-processed (b) 1-day predicted

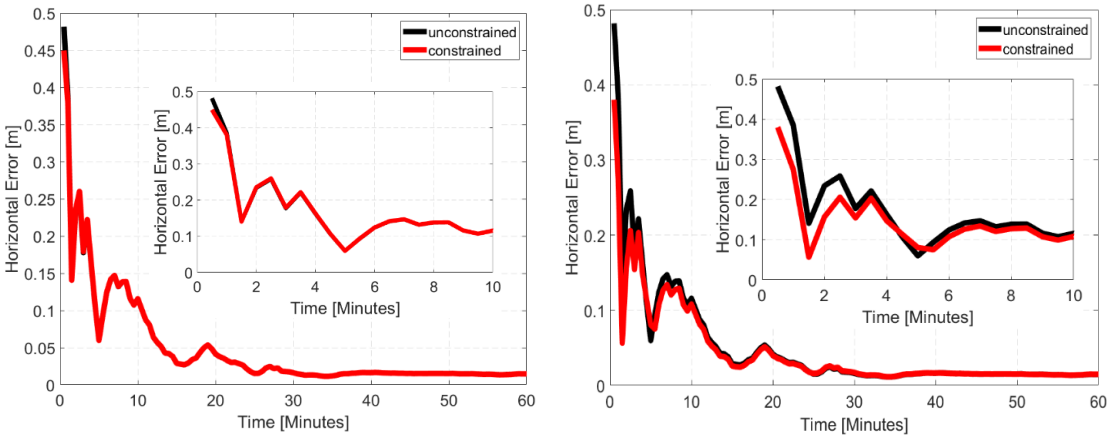

(c) 2-day predicted (d) Combined together from other ACs

Figure 4.5: 1-hour GIM constrained and unconstrained solutions for ALGO station located in Algonquin Park, Canada for DOY 28, 2015.

It must be noted that it is not the aim of this study to advocate one product over another, but rather to point out the effect of choice in the selection of an IONEX product in PPP processing. As shown in Figure 4.5, PPP initialization and convergence are impacted depending on the selection of either post-processed or predicted IONEX product.

Shown in Figure 4.6 are the results of analyses made on how different existing IONEX products affect the performance of ionospheric constraining in multi-GNSS PPP solutions. Using 3 days of 24-hour observations from MGEX multi-GNSS stations mapped out in Figure 4.4, PPP solutions were obtained for both dual- and triple-frequency PPP processing modes. Only post-processed products were used for the sake of uniformity. The idea was to show whether after 24 hours of processing,

PPP convergence was impacted by the kind of product used. A second objective, where ionospheric constraining plays a major role, was to investigate PPP convergence by horizontal error in the first 10 minutes using the different IONEX products. As observed in Figure 4.6(a) and (b), over 24 hours, there are millimetre-level variations between the products in the dual- and triple-frequency positioning results, respectively. A similar trend was observed in the first 10 minutes of PPP convergence, as portrayed in Figure 4.6(c) and (d). However, in the 10-minute scenario, centimetre-level differences could be observed though some of the products still had millimetre range differences. These differences were evident in both the dual- and triple-frequency PPP results as well. It must be clarified that the purpose of these analyses was not to assess the products in terms of processing modes but highlight the influence a choice of product could have on the initial solution convergence.

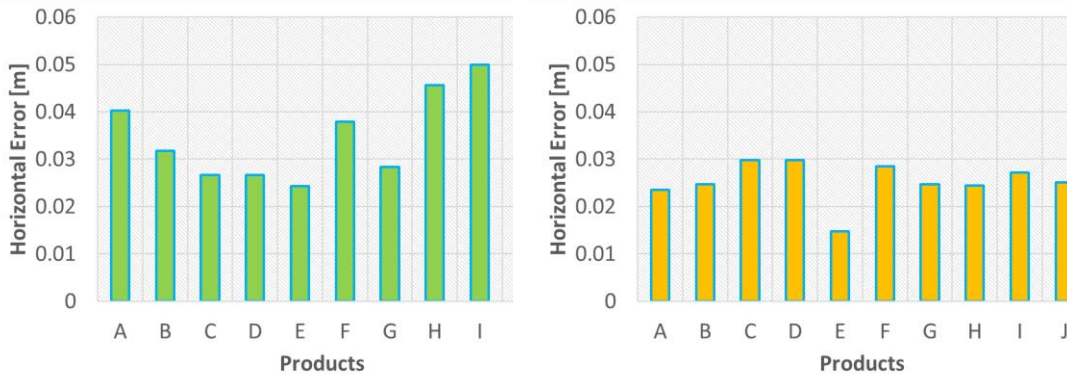

(a) 24-hour convergence: dual-frequency

(b) 24-hour convergence: triple-frequency

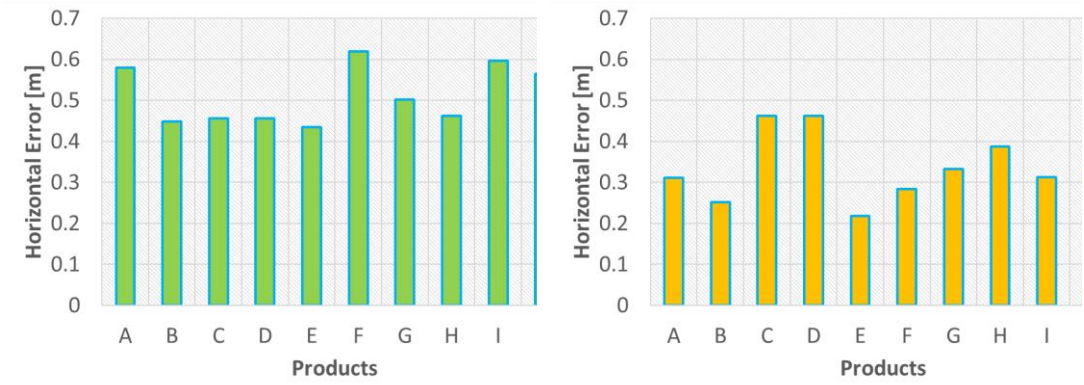

(c) 10 minutes convergence: dual-frequency

(d) 10 minutes convergence: triple-frequency

Figure 4.6: Results of analyses for 24-hour and 10-minute convergence for different existing IONEX products. using 3 days of 24-hour observations from MGEX multi-GNSS stations.

It is necessary to point out that the IONEX product for a particular day represents a snapshot of the ionospheric activity occurring within that time frame. Hence, the results presented are not conclusive for all other days as each day can potentially show different results than those presented for DOY 32 – 34 of 2016. Datasets from 2016 were used in most of the analyses presented in this chapter because of difficulty in obtaining consistent datasets and products from archiving sources. A key intended point is to show that depending on the product used to constrain PPP solutions, especially in the first few minutes, there is the possibility of centimetre-level differences that could be seen. As depicted in Table 3.3, products with higher numbers

of network stations and GNSSs used were observed to better constrain the PPP solutions.

4.5 Latitudinal correlation with ionospheric modelling

To investigate whether there is a correlation between high ionospheric activity and GNSS measurements and how this impacts PPP positioning performance, GNSS stations were strategically selected based on different latitudes. Figure 4.7 shows the distribution of the selected MGEX stations for DOY 32 to 38 of 2016, categorized according to upper, middle and lower latitudes. As stated previously, the receiver-antenna combination of the stations was kept homogeneous to reduce the effect of equipment delays. Red and blue represents Trimble and Javad receivers, respectively. It is well known that high-order ionospheric effect is noticeably at its maximum during the mid-days of local time. Liu et al. (2016) investigated the second-order effect of the ionospheric on static PPP solutions. Results from rms statistics showed that the ionospheric effect on satellite orbits ranged from 11 mm to 24 mm in all tracks. It was observed that different latitudes and station distribution affect the higher order ionospheric delay. Hence, it was concluded that different latitudes played a role in the differences observed in the estimated higher-order ionospheric delays.

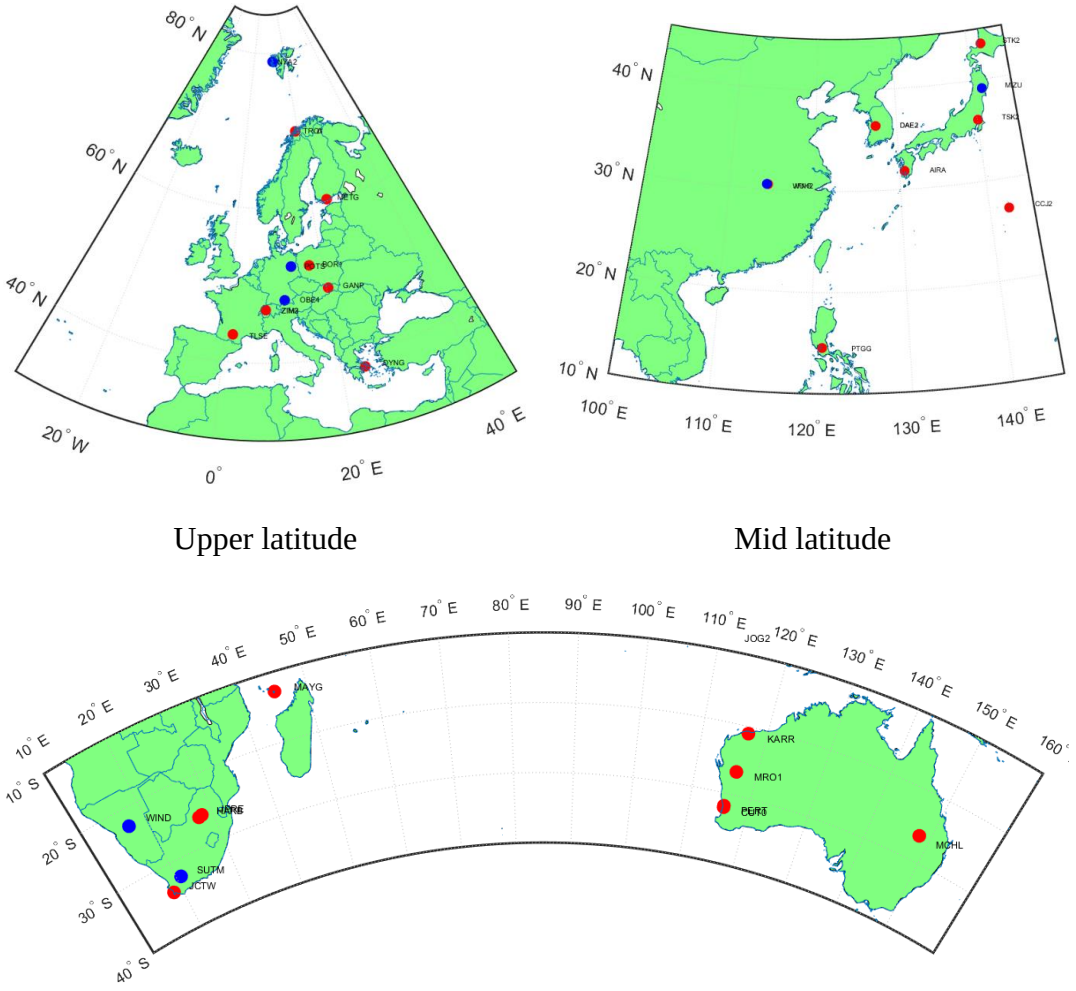

Upper latitude Mid latitude

Lower latitude

Figure 4.7: Distribution of selected MGEX GNSS stations for DOY 32 to 38, 2016 based on upper, middle and lower latitudes. Red and blue represents Trimble and Javad receivers, respectively.

One major goal of this study is to analyze the effect that low and high ionospheric activities have on positional accuracy in PPP based on different latitudes. To do so, it was necessary to choose days where typical ionospheric activities were

observed without the influence of adverse solar phenomena. Figure 4.8 shows the ionospheric activity for DOY 33, 2016 for hours 6, 12, 18 and 22. The ionospheric characteristics observed were typical for all the other days of that week. Regions around the geomagnetic equator showed expected high ionospheric activity. Dual- and triple-frequency modes were employed in the multi-GNSS PPP processing for completeness. The results presented in this section are not meant to indicate that one mode of processing is better than the another. Using GIM and associated rms maps found in IONEX products, the multi-GNSS PPP solutions were constrained. Being reliant on the variations observed in the ionosphere in a day, it was expected that using GIM would reflect the varying ionospheric activities in the PPP solutions in terms of convergence time. By processing groups of multi-GNSS stations at different latitudes with varying ionospheric phenomena, the results would be indicative of the influence that changes in ionosphere has on PPP ionospheric constrained solutions.

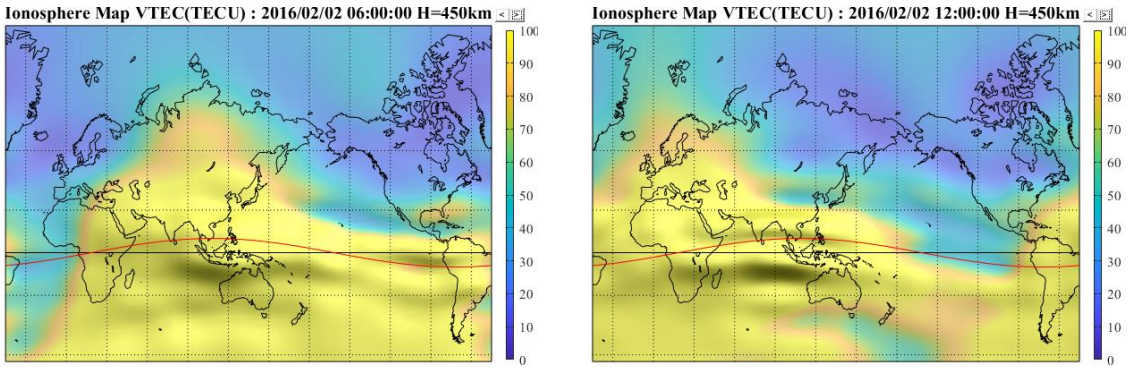

(a) (b)

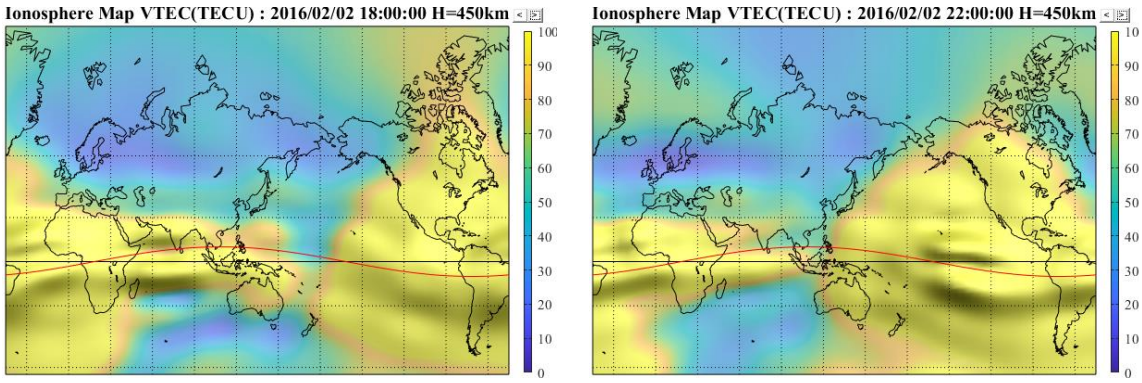

(c) (d)

Figure 4.8: Ionospheric activity for DOY 33, 2016 for hours 6, 12, 18 and 22. Red line represents the geomagnetic Equator. Bar scale are in units of TECU.

Shown in Figure 4.9, Figure 4.10 and Figure 4.11 are the dual- and triple-frequency PPP GIM constrained solutions in the first hour of convergence for upper, mid and lower latitudinal regions, respectively. It was interesting to observe that after 20 minutes, the differences between the solutions for all the three regions was minimal, indicating that irrespective of the latitude, optimal performance with GIM was obtained before the first 20 minutes. Constraining further after the 20 minute-mark had limited effect, especially for the upper and mid-latitude regions. This characteristic is understandable given that that ionospheric constraint is usually critical and effective only in the first few minutes of PPP convergence and initialization in either dual- or triple-frequency PPP processing modes.

The key differences were observed within the first 15 minutes. Taking into consideration a 10-minute convergence period, 40%, 50% and 18% of stations reached

a 20 cm horizontal threshold in the upper, mid and lower latitudes, respectively, for dual-frequency processing. In the triple-frequency case, 46% of the stations reached the horizontal threshold in the upper latitudinal region. However, mid and lower latitudes saw an improvement with 48% and 36% of the stations reaching the threshold, respectively. Similarly, major differences in terms of improvements and percentages of stations reaching the 20 cm horizontal threshold, varied depending on the processing mode. Though the same GIM product was used in constraining the solutions, different convergences were observed when the solutions were ionospherically constrained. It becomes obvious that the slant VTEC from GIM and its corresponding rms values affect PPP convergence since they are not uniform with regards to latitudinal changes.

However, there are major limitations to be considered in this analysis. Environmental conditions of the stations used can potentially affect the outcome. The location, stability, multipath profile and even receiver firmware changes are all limiting factors which were not taken into account but can potentially affect the results. Satellite geometry and visibility is another factor that potentially impacts convergence in this analysis. Given that the stations are in different latitudes, there is the possibility of rejecting some satellites or processing less satellites due to bad geometry. However, with these limiting factors in mind, it is necessary to take note of the role that ionospheric latitudinal changes affect PPP constrained solutions.

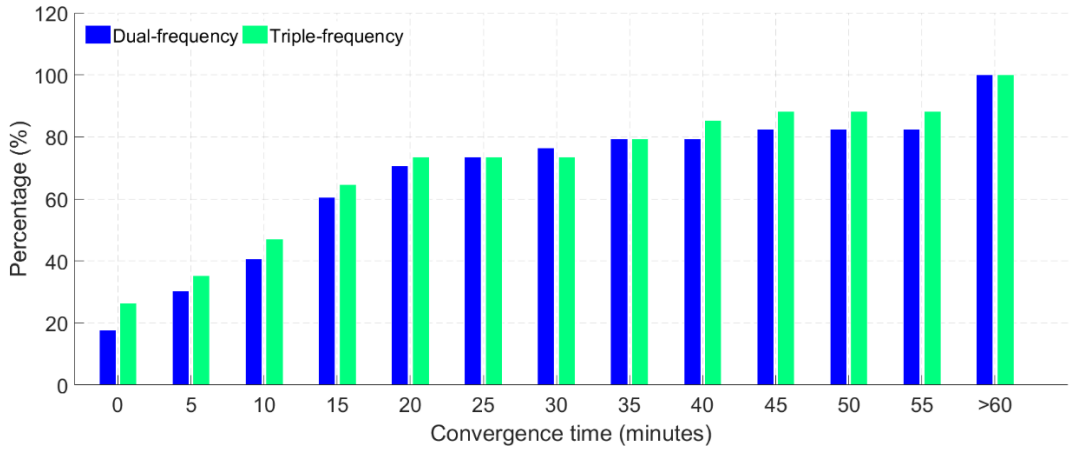

Figure 4.9: Dual- and triple-frequency PPP solutions showing the first hour of convergence periods for upper latitude stations with GIM constraints. Results for horizontal components with 0.2 m horizontal error threshold.

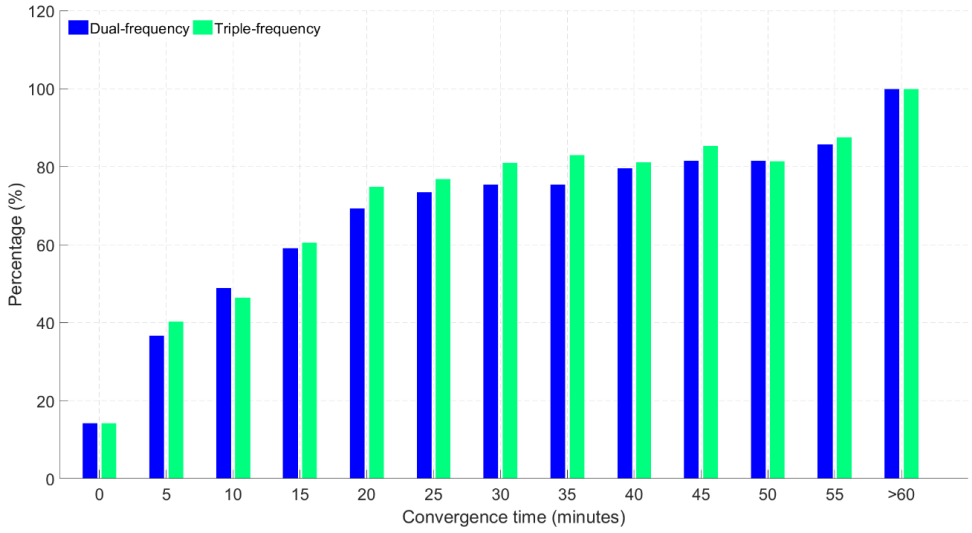

Figure 4.10: Dual- and triple-frequency PPP solutions showing the first hour of convergence periods for middle latitude stations with GIM constraints. Results for horizontal components with 0.2 m horizontal error threshold.

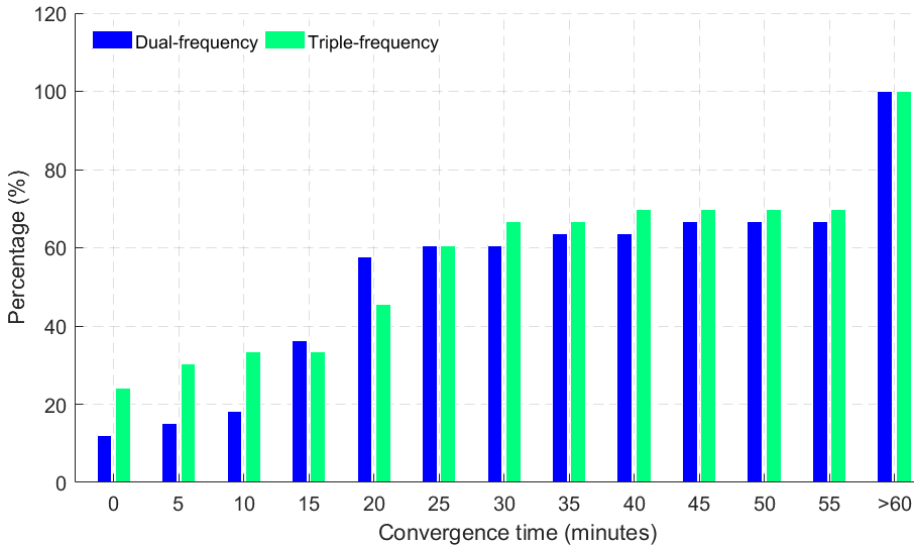

Figure 4.11: Dual- and triple-frequency PPP solutions showing the first hour of convergence periods for lower latitude stations with GIM constraints. Results for horizontal components with 0.2 m horizontal error threshold.

4.6 **Proximity analysis of slant ionospheric delays from nearby stations**

The use of global ionospheric corrections from a global network of stations does help in improving the solution quality in PPP as discussed before. There is a dependency on network density for better interpolation between ionospheric pierce points. This dependency is a concern, which affects the PPP user when constraining the solutions. The denser the network of stations, typically the better the ionospheric TEC estimates obtained. It is expected that by using the slant ionospheric estimates from nearby stations, the solution convergence should be better than using a station far away. However, how close does a reference station have to be or how dense does

a network need to be for its slant ionospheric estimates to be helpful in achieving PPP-AR-like performance in multi-GNSS PPP processing? To attempt answering this question, a group of selected stations were used, as shown in Table 4.2, with varying baseline distances up to ~200 km. Also shown in Figure 4.12 is the distribution of the stations. The stations were selected based on their proximity from the reference station ALBH, located in Victoria, Canada.

GNSS Station	Reference / Rover	Distance from reference station (km)
ALBH	Reference	0
P435	Rover	37
P439	Rover	56
P401	Rover	94
PCOL	Rover	152
P417	Rover	202

Table 4.2: Network of GNSS stations with varying baseline lengths.

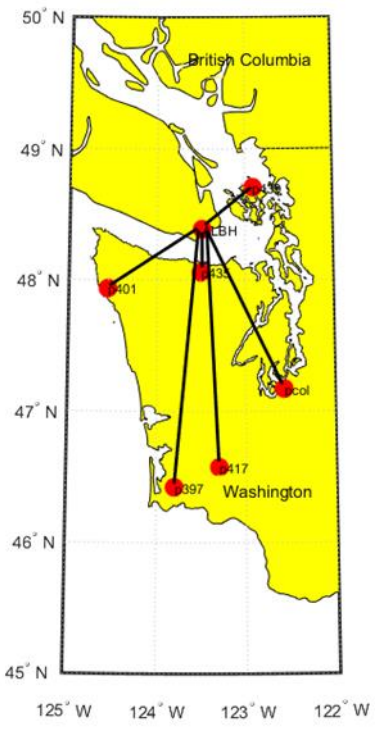

Figure 4.12: Distribution of selected MGEX GNSS stations for DOY 32, 2016 used in the proximity analysis.

Estimated slant ionospheric corrections from rover stations were used as constraints in the first epoch of multi-GNSS dual-frequency PPP processing. Using a horizontal error threshold of 10 cm, convergence times were observed for each rover ionospheric constraint used even as the baseline length widened. As depicted in Figure 4.13, the convergence of the reference station improved with slant delays from nearby stations, shown by the steady blue line. From 37 km to 202 km, the convergence times steadily rose from 11 minutes to 16 minutes, respectively.

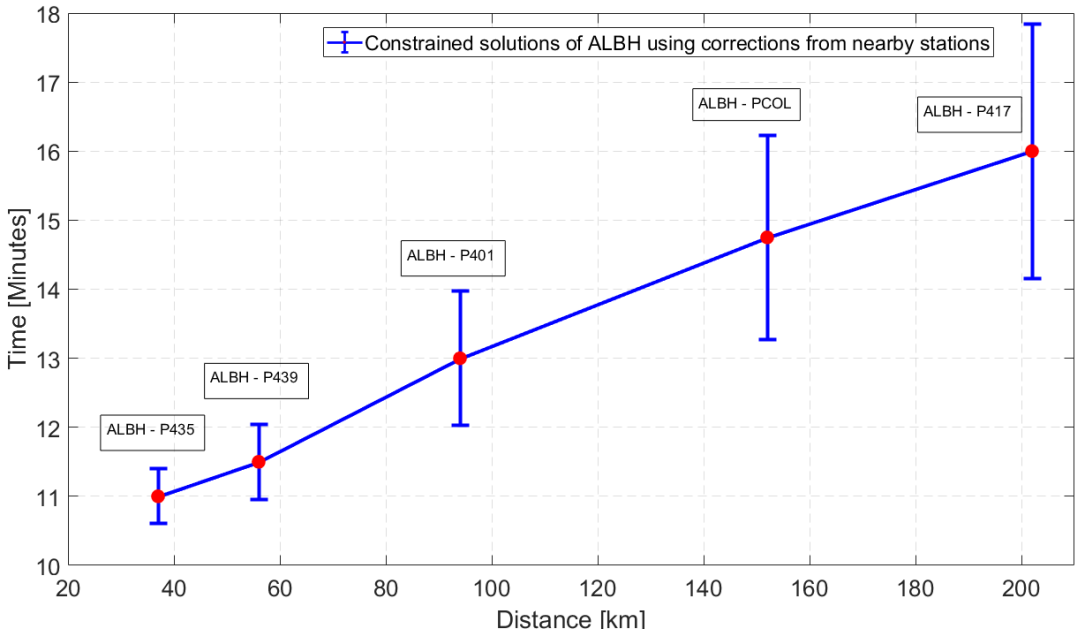

Figure 4.13: Proximity analysis showing convergence times between rover stations with increasing baseline lengths considering 10 cm horizontal threshold.

The uncertainties, represented by the error bars, also showed a steady increase which corresponded with the length of the baseline between ALBH station and the rover stations. It was interesting to observe that stations had to be less than 100 km apart for a convergence time of 12 minutes or less to be realized when using nearby stations to constrain the PPP solutions.

4.7 Dual- and triple-frequency multi-GNSS PPP atmospheric constraining with ambiguity resolution

This section presents analyses on the impact of atmospheric constraints in multi-GNSS PPP processing. The purpose is to outline the progression of improvement in

the usage of atmospheric constraints. While the aim is to improve the solution quality and accuracy, further insight is also provided on how different processing modes are impacted by atmospheric constraining. It must be noted that post-processed products are used for the analyses presented in this section. These post-processed products include the orbits and clocks as well as GIM. Real-time analyses were not considered in this section given the unavailability of real-time GIM delays and ZPD estimates.

4.7.1 Datasets used and data processing details

To investigate the impact of atmospheric parameter constraints in both dual- and triple-frequency multi-GNSS PPP, 40 globally distributed MGEX GNSS receiver stations were arbitrarily selected for PPP processing. Figure 4.14 shows the global distribution of stations.

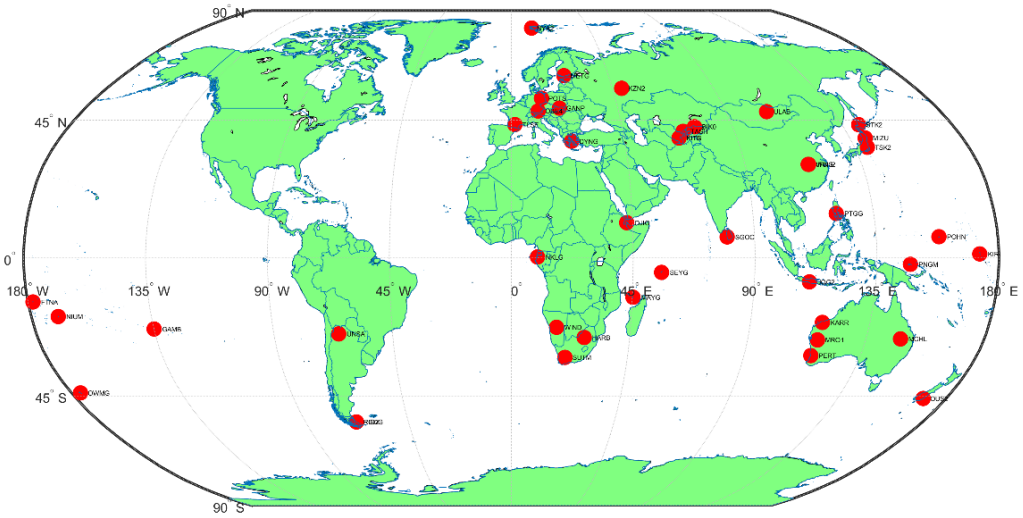

Figure 4.14: Map of global distribution of selected multi-GNSS stations.

Observations from these stations were processed from DOY 253 to 259 in 2018. The stations were arbitrarily selected based on homogeneity of receiver and antenna types to limit the effects of equipment hardware delays impacting the results. Javad and Trimble receiver-antenna combinations were considered. Shown in Table 4.3 are the processing parameters and settings used in the generation of results discussed in subsequent sections. GBM precise orbits and clocks from GeoForschungsZentrum (GFZ) were used because of the availability of orbits and clocks for all available GNSS constellations.

Processing parameters	YorkU GNSS PPP engine settings
Processing technique	Uncombined mode using raw strength of observations
Antenna corrections	IGS ANTEX
Satellite orbits and clocks	GBM (GFZ)
Elevation mask	Minimal 10°
GNSS system	GPS, GLONASS, Galileo and BeiDou
Observation processing mode	Dual-frequency, Triple-frequency, GPS ambiguity resolution, static processing
Data format	RINEX 2.x or 3.x
Ionospheric mitigation	Slant ionospheric delays: estimated GIM delays: used to constrain only the first epoch
Troposphere modelling	Hydrostatic delay: Davis (GPT) Wet delay: estimated

Table 4.3: Processing strategy and parameters used in YorkU GNSS PPP engine for data analysis

4.7.2 Dual-frequency analysis

Shown in Figure 4.15 and Figure 4.16 are the histogram and time series of dual- frequency GPS(G) + GLONASS(R) + Galileo(E) + BeiDou(C) (GREC) PPP atmospheric-constrained, static horizontal solutions in the first hour of convergence, respectively. Defining convergence period as the time the solutions take to reach a horizontal error of 20 cm, the histogram shows a level of consistency benefiting PPP solutions when they are atmospherically constrained. Percentages of stations reaching the defined convergence threshold are shown. Three different scenarios were analyzed which included (1) unconstrained GREC PPP solutions, (2) Ionospheric (GIM) constrained and (3) GIM + tropospheric constrained GREC PPP solutions. It is interesting to observe that after 20 minutes, the differences between the solutions for GIM constrained and GIM + ZPD constrained solutions are minimal, indicating that optimal performance with GIM and ZPD constraints was obtained before the first 20 minutes. Constraining further after the 20 minute-mark had very limited effect on improving positioning performance.

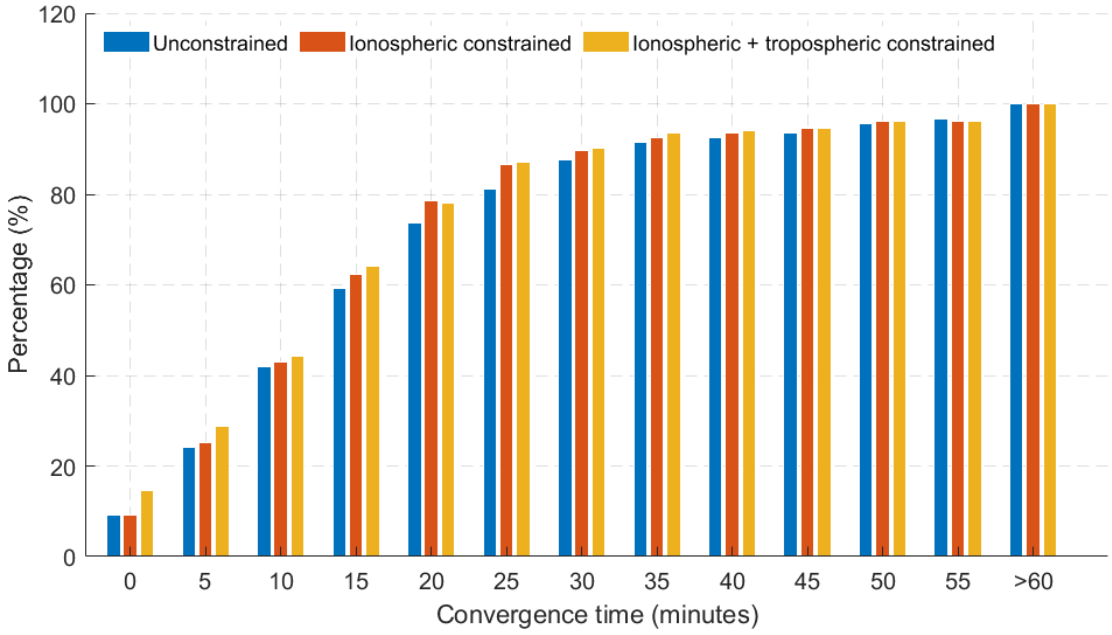

Figure 4.15. Histogram showing percentage of 40 stations converging based on 24 hourly solutions in dual-frequency GREC processing mode. Results shown have a 20 cm horizontal error threshold.

This characteristic is understandable given that atmospheric constraints are usually critical and effective only in the first few minutes of PPP convergence and initialization.

The prominent differences were observed within the first 15 minutes. The atmospheric constrained solutions saw an average of 6% improvement over the unconstrained, in terms of percentages of stations converging under 20 cm of horizontal error. However, the histograms do not tell the whole story. By observing the convergence time series, the significance of the constrained solutions becomes even much more obvious. By defining a stricter convergence of 10 minutes under a

horizontal positional error of 10 cm, the 95th percentile of the atmospheric constrained solutions reached convergence in 6 minutes, as shown in Figure 4.16. The effectiveness of applying atmospheric constraints is clearly seen in the first few epochs. The quickest initialization was observed for ionospheric and tropospheric constrained solution.

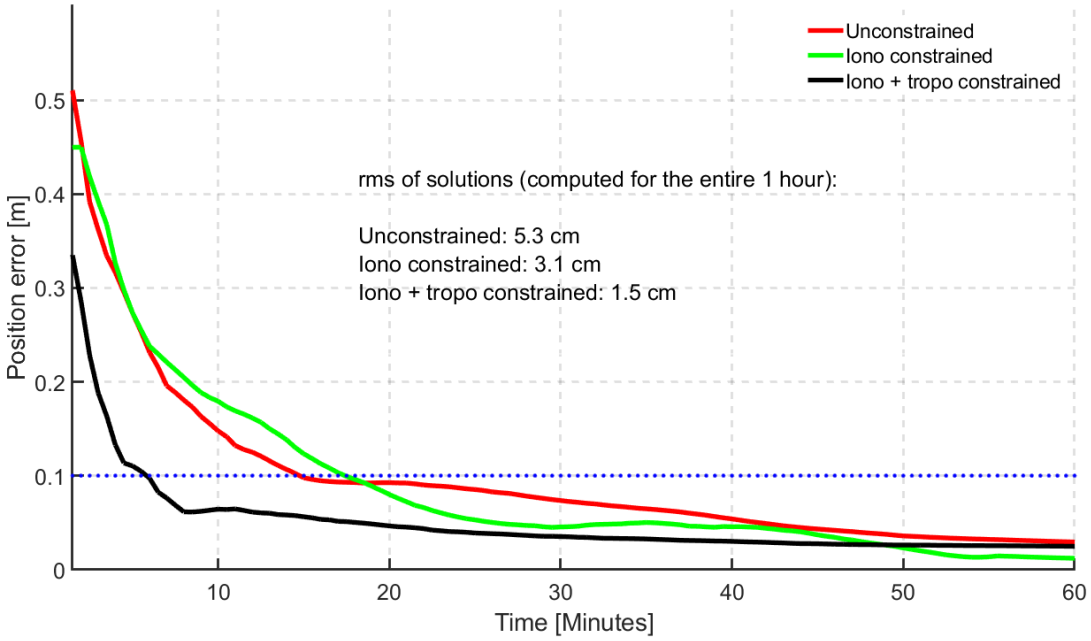

Figure 4.16. 95th percentile time series showing horizontal positional error (hourly) based on 24 hourly solutions for 40 stations for dual-frequency GREC processing mode. Blue dotted line represents the 10 cm convergence threshold.

4.7.3 Triple-frequency analysis

As shown in the dual-frequency scenario, similar characteristics were observed for the triple-frequency atmospheric constrained GREC PPP solutions. A look at the

histogram, as shown in Figure 4.17, saw an average of 7% improvement over the unconstrained, in terms of percentages of stations converging under 20 cm of horizontal error.

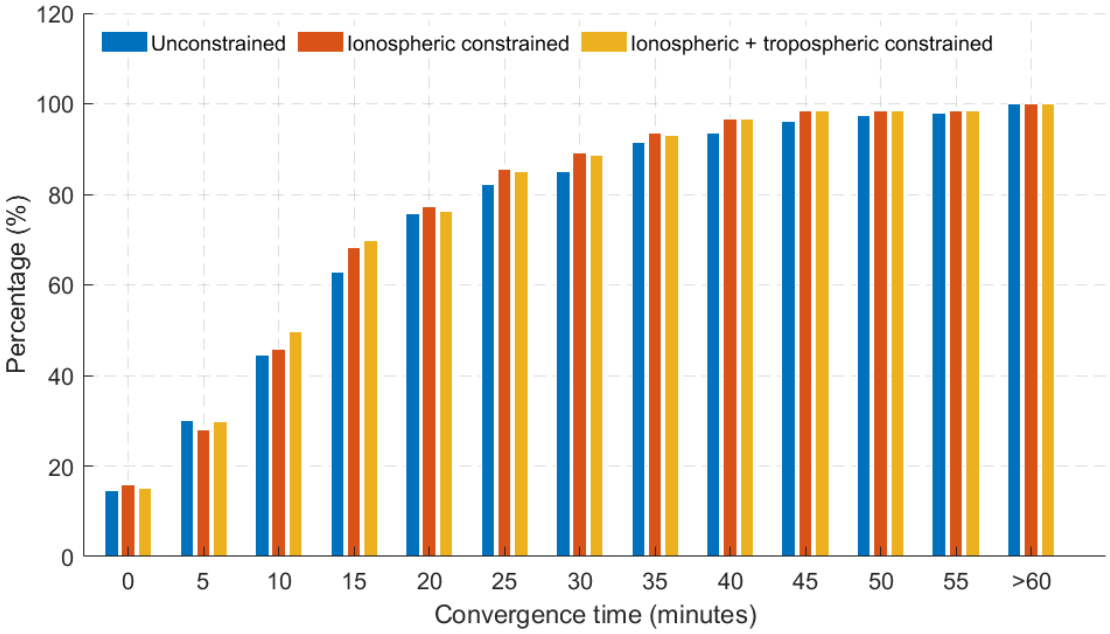

Figure 4.17. Histogram showing percentage of 40 stations converging based on 24 hourly solutions in triple-frequency GREC processing mode. Results shown have a 20 cm horizontal error threshold.

However, a significant level of improvement was observed by investigating the convergence of the time series of the atmospheric constrained solutions as depicted in Figure 4.18. Considering the 95th percentile and convergence defined as 10 minutes

for solutions to fall under 10 cm of horizontal positional error, the atmospheric (iono + tropo) constrained solutions achieved convergence in 2 minutes.

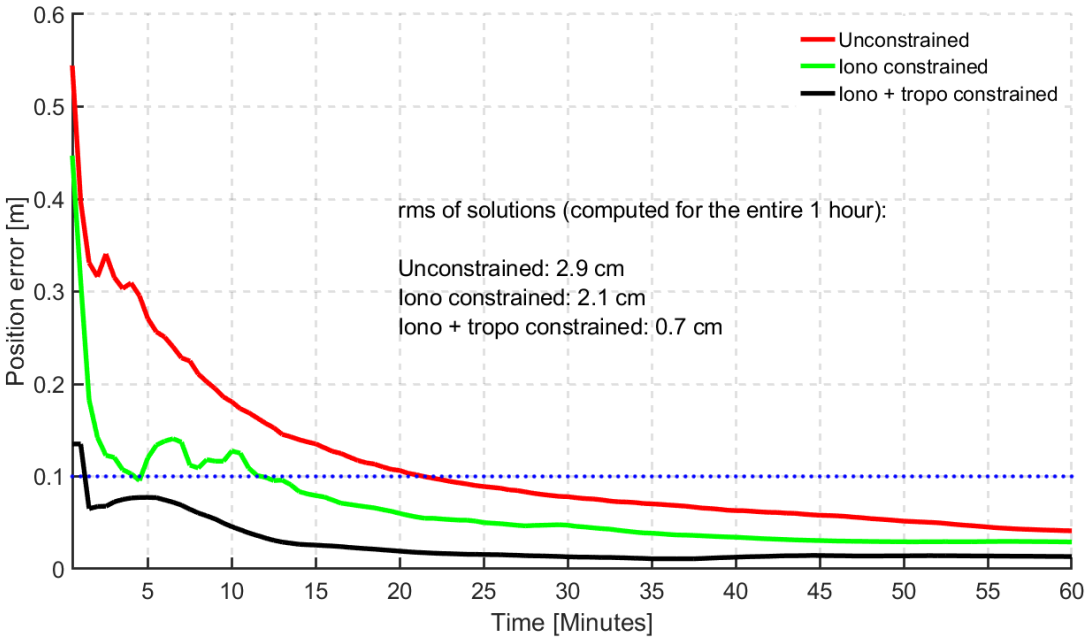

Figure 4.18. 95th percentile time series showing horizontal positional error (hourly) based on 24 hourly solutions for 40 stations for triple-frequency GREC processing mode. Blue dotted line represents the 10 cm convergence threshold.

This level of improvement is significant and relevant as it reveals not only the benefits of having more frequencies, but how the coupling of these extra frequencies with atmospheric constraining can enhance the solution quality of multi-GNSS PPP solutions. In comparison to the dual-frequency constrained scenario, the triple-frequency constrained solutions had a 67% improvement in terms of solution convergence.

4.7.4 Dual-frequency analysis with GPS-AR

The third scenario investigated involved resolving the ambiguities for GPS satellites while applying atmospheric constraints in a dual-frequency GREC PPP processing. Only GPS ambiguities were resolved for this analysis but future work would include GEC-AR. Similar to the other previous scenarios, the histogram, as shown in Figure 4.19, saw an average of 6% improvement over the unconstrained, in terms of percentages of stations converging under 20 cm of horizontal error. More insight was provided in the times series as shown in Figure 4.20.

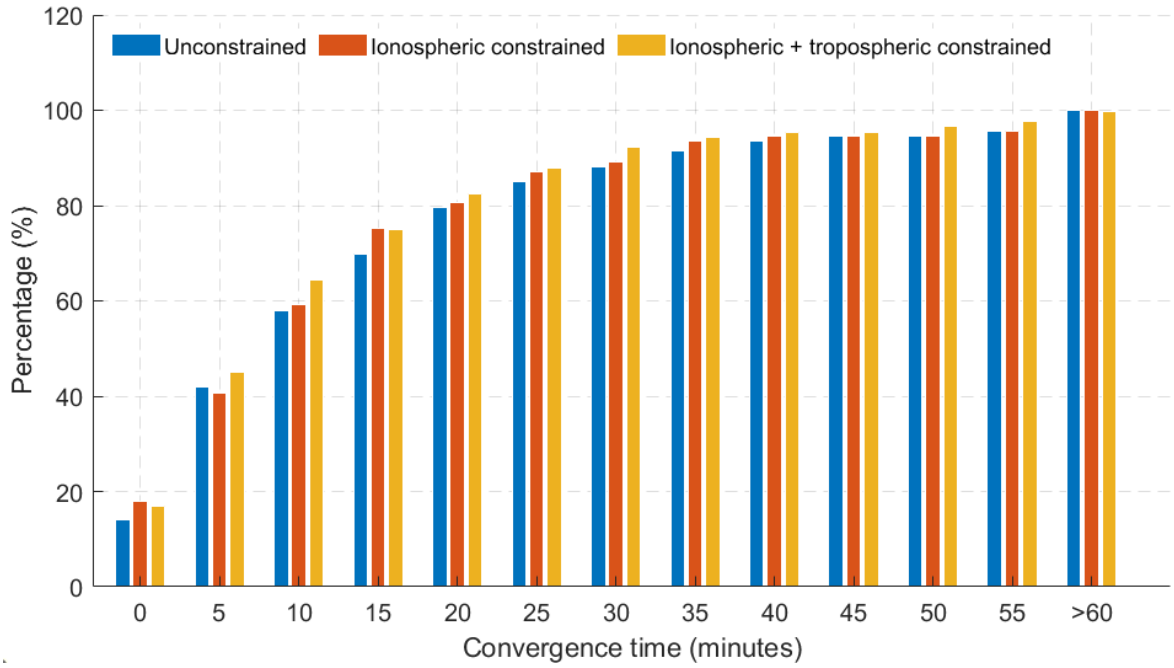

Figure 4.19. Histogram showing percentage of 40 stations converging based on 24 hourly solutions in dual-frequency GREC with GPS-AR processing mode. Results shown have a 20 cm horizontal error threshold.

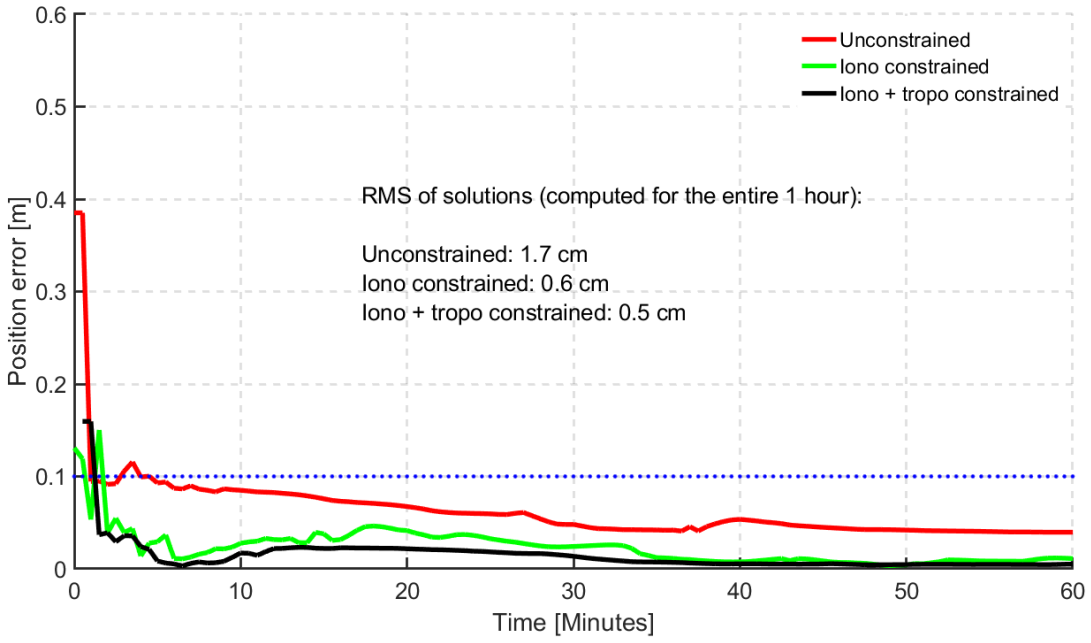

Figure 4.20. 95th percentile time series showing horizontal positional error (hourly) based on 24 hourly solutions for 40 stations for dual-frequency GREC with GPS-AR processing mode. Blue dotted line represents the 10 cm convergence threshold.

With convergence defined as 10 minutes for solutions to fall under 10 cm of horizontal positional error, and considering the 95th percentile, the atmospheric constrained solutions with GPS-AR achieved convergence in less than 2 minutes. The steadiness of the converged solutions was consistent than triple-frequency atmospheric constrained solutions.

In summary, it is imperative to bring into context all the significant levels of improvement throughout all the various scenarios addressed in this chapter. Shown in Table 4.4 are the significant improvements in convergence time observed with contributions from the research work in this chapter. The typical convergence in

minutes is compared to the research contributions through the results presented in this chapter. With RTK-like performance being the target, it is expedient to address how close PPP is to RTK performance. Considering a typical RTK convergence of a few centimetres in a few minutes, the atmospheric constrained multi-GNSS PPP solutions presented is closely comparable to RTK performance, though we are not there just yet. The significance of this enhanced performance informs the possibility of using PPP in much more time-sensitive applications.

Processing modes	Convergence in minutes (Typical)	Convergence in minutes (Achieved)
Dual-frequency PPP	20	15 (Aggrey and Bisnath 2017b, a)
Triple-frequency PPP	20	18 (Aggrey and Bisnath 2017b)
Dual-frequency atmospheric-constrained PPP	~	6 (Laurichesse and Blot 2016)*
Triple-frequency atmospheric-constrained PPP	~	2 (Laurichesse and Blot 2016)*
Dual-frequency PPP-AR	15	11 (Seepersad et al. 2017)
Dual-frequency atmospheric-constrained PPP-AR	~	< 2

Table 4.4. Improvements in convergence time achieved in comparison to typical convergence periods (to 10 cm horizontal) defined by the mode of PPP processing.

**By mitigating triple-frequency biases, Laurichesse and Blot (2016) obtained these tropospheric constrained PPP convergences by considering 20 cm horizontal error threshold.*

4.8 Summary

It is concluded that the choice of using predicted or post-processed products impacts the level of improvement in PPP solution initialization and convergence. Centimetre-to-millimetre level of variations were observed to exist among the different IONEX products when used to constrain dual-and triple-frequency PPP solutions. Using a global network of stations in different latitudinal regions through novel analysis, it was observed that key differences exist in terms of convergence time improvements and percentages of stations reaching a 20 cm horizontal threshold depending on the processing mode. It was also observed that the slant VTEC from GIM and its corresponding rms values affect PPP convergence since they are not uniform with regards to latitudinal changes. It was significant to observe the effect that ionospheric latitudinal changes had on multi-PPP constrained solutions. Proximity analysis was also conducted to ascertain how far or close a nearby station had to be for its slant ionospheric delay to be useful in constraining PPP solutions when considering a tight convergence threshold of 10 cm horizontal error. For a convergence time of 12 minutes or less, it was observed that stations had to be less than 100 km apart in the test data used. The significance of the analysis anchors on the sparsity or

density of the network of stations used to generate ionospheric products which potentially affects the PPP user in terms of solution convergence.

Using GIM and tropospheric zenith delay corrections, a progression of improvements has been shown. Position accuracy and solution convergence were the key criteria assessed. By resolving ambiguities while constraining atmospheric parameters, it was observed that the multi-GNSS PPP solutions converged to the decimetre-level in less than 2 minutes for the horizontal components. Comparing the atmospheric constrained multi-GNSS PPP-AR to the unconstrained solution, a significant level of improvement was noticed which addressed the importance and efficacy of the constraints applied. The atmospheric constrained PPP solutions for triple-frequency PPP solutions showed more than 60% improvement in the position accuracy as compared to dual-frequency solutions. Using a strict convergence threshold of 10 minutes for the PPP solution to be steady under a horizontal error of 10 cm, the significance of atmospheric constraints in PPP-AR was shown. The realism of the GIM and estimated slant delays was also investigated which informs on the need to be cautious of either under or over constraining the PPP solutions. In summary, to address the original questions posed at the introduction of this contribution, here are the brief conclusions:

(1) ***What is the magnitude of improvements observed from the usage of traditional dual-frequency measurements to triple-frequency PPP processing with atmospheric constraints?***

Results presented showed a significant level of improvement of more than 60% from atmospheric constrained dual- to triple-frequency multi-GNSS PPP in terms of the reduction in convergence time.

(2) ***What are the inherent challenges when constraining PPP solutions with atmospheric corrections either functionally or stochastically?***

It was shown that caution needs to be taken when using GIM estimates and their uncertainties to constrain. To avoid under or over constraining, there is the need for an adaptive method in the application of the constraints.

(3) ***What is the significance of PPP-AR in multi-GNSS PPP atmospheric constrained solution?***

PPP-AR plays a vital role and enables an improved atmospheric constrained solution. Results presented in this chapter with GPS-AR showed the best improvement at the 95^{th} percentile.

(4) ***Finally, what are the key challenges left in obtaining near-instantaneous PPP convergence akin to RTK data processing?***

With typical RTK convergence of 2 minutes to reach decimetre level of accuracy, the result summary presented in Table 4.4 showed how close we are to near-instantaneous convergence akin to RTK. With better and improved atmospheric products, as well as orbits, clocks and bias estimation, PPP solution accuracy is bound to get better.

Figure 4.21 illustrates the accuracy progression of PPP in different processing modes as compared to RTK and the standard positioning service (SPS). With RTK defining the core of accuracy at the millimetre-centimetre level, the combination of ambiguity resolution and ionospheric constraining draws PPP closer to RTK. PPP has evolved over the years from the conventional float dual-frequency solutions to triple-frequency with AR. It is anticipated that PPP will continue to improve with the mitigation of measurement and hardware biases. So where are we now as PPP users? It is safe to say that we are in the light green zone getting warmer to the greener turf of RTK performance.

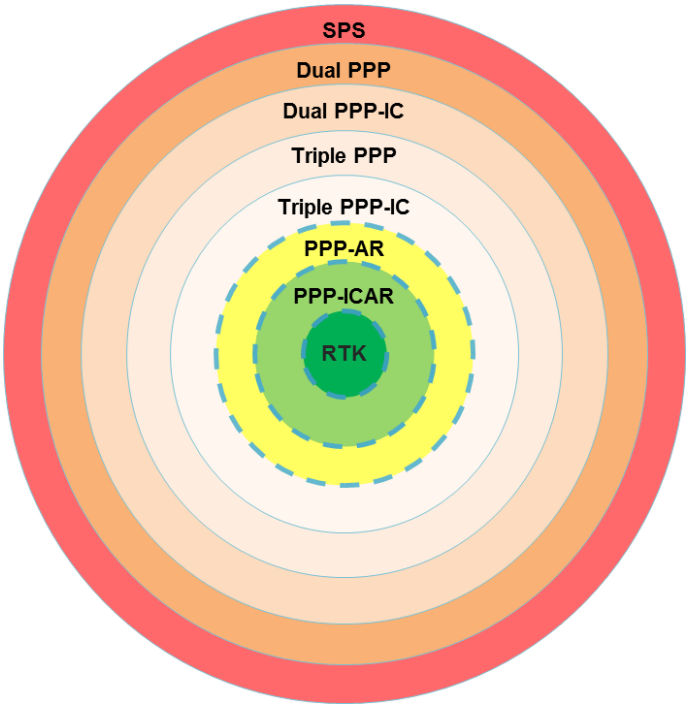

Figure 4.21: Accuracy hierarchy from RTK to Standard Positioning Service (SPS). This diagram is an augmentation from Collins et al. (2012).

CHAPTER 5 MULTI-GNSS PPP USING NEXT-GENERATION SMARTPHONE MEASUREMENTS

This chapter evaluates the feasibility of achieving improved positioning accuracy with raw GNSS measurements from recently released smartphones. Using PPP as the processing mode, positioning accuracy and performance of selected newly available devices are analyzed. These devices include the Xiaomi Mi8, Google Pixel 3, Huawei Mate 20 and Samsung Galaxy S9. All tested devices had the capability of tracking either three or four GNSS constellations, and the first and third track two frequencies. This chapter provides a synopsis on the evolution of navigation on smart devices. A detailed smartphone measurement analysis is also provided. Static and kinematic PPP analyses are investigated with emphasis on the impact of smartphone hardware on the accuracy of user position.

The key research questions to be answered are: (1) What is the typical performance when using the raw measurements from these smartphones in multi-GNSS PPP processing in static and kinematic scenarios? (2) Given the limitation that the hardware components of the smartphones present, what PPP processing changes can be implemented to make use of the raw measurements from smartphones? (3) What is the level of accuracy that can be achieved with multi-GNSS PPP given normal smartphone usage by the user?

5.1 Introduction

The proliferation of smartphones over the past few decades has fuelled technological innovation in navigation applications. In contrast to decades-old mainframe computers, the performance of current mobile devices with faster processor chipsets reveal greater and better capabilities. The promise that such advancement ushers in includes lower cost rates in the development, testing and deployment of various applications. From a software perspective, mobile device applications enjoy faster update cycles, while eliminating the need for extra hardware components. There are currently over five billion GNSS enabled devices worldwide with over 75% of such devices being smartphones (European GNSS Supervisory Authority 2017). The use of location information accounts for more than 50% of applications on smartphones, either through Google Play or Apple stores (Kaplan and Hegarty 2017; Sunkevic 2017). This critical need for position and timing capabilities on smartphones makes the case to understand, investigate and improve the accuracy standard. Applications requiring high precision such as car navigation, personnel monitoring and bicycle rental services are currently being hosted on smartphones. The desire for high accuracy location-based services in the mass market only serves as the impetus to advance further with improving GNSS positioning on smartphones as observed in various research contributions (Pesyna et al. 2014; Kirkko-Jaakkola et al. 2015; Banville and Van Diggelen 2016; Yoon et al. 2016; Humphreys et al. 2016; Alsubaie

et al. 2017). Considering the rising use of smart wearables and phones, GNSS navigation is bound to expand the possibility of various other applications that currently may not seem feasible due to the constraints of geodetic-grade precision and accuracy. Hence, the primary goal of this chapter is to test the bounds of accuracy which would address how far multi-GNSS positioning with PPP can afford the smartphone user. The challenges and benefits of processing multi-GNSS smartphone data in both static and kinematic PPP modes in open-sky and obscured urban environments will be addressed.

The introduction of the world's first dual-frequency GNSS-enabled smartphone, the Xiaomi Mi8, has brought some excitement to both academia and navigation research in general. The Xiaomi smartphone is equipped with a Broadcom BCM47755 chipset capable of tracking L1/E1 and L5/E5 signals from GPS, Galileo and BeiDou (EGSA 2018; Robustelli et al. 2019). Other releases such as the Huawei Mate 20 and Huawei Mate 20 Pro also have dual-frequency chipsets which track all available GNSSs. With this recent public access to raw GNSS observations on smartphone devices, a new dawn in low-cost positioning is on the horizon. Enabled by Google through its Android API, pseudorange and carrier-phase measurements can be obtained in real-time from off-the-shelf, mass-market devices (Sunkevic 2017). In difficult environments such as urban canyons, the typical expected performance of mobile devices is in the range of a few metres to many tens of metres, considering a

single-frequency processing scenario. However, the use of multi-GNSS measurements from either dual- or single-frequency chipsets coupled with extra error modelling promises to enhance the solution accuracy (and initial position solution convergence) to a few decimetres. This chapter addresses the advantage of the Android raw measurements in PPP processing, while providing integrity measures that are needed to be adhered to for a robust and reliable position solution.

5.2 Evolution of navigation on smart devices

A pioneering step into the future of car navigation was realized in 1985 when Etak Inc. introduced the Etak Navigator, as shown in Figure 5.1. This product release represented the first generation of smart device navigation. Though it offered basic features, limited geographical coverage, and few user and route options, it showed the possibilities and potential of chipset receivers. The automobile industry was then revolutionized by navigation technology (Zavoli and Bloch 1990). The dawn of personal digital assistants (PDAs) and Benefons represented the second and third generations of smart navigation devices. In contrast to their first-generation counterparts, these devices offered wireless connections with the acquisition of real-time data, but only for a limited geographical coverage area (Viken 2010; Sullivan 2012; Edwards 2018). However, fourth generations devices like Garmin's GPS units offered end users not only global coverage but personalized service-oriented options regulated by cellular service providers.

1st Gen: Etak Navigation system

2nd Gen: PDAs

3rd Gen: Benefon

4th Gen: Nuvi 200W

5th Gen: smartphone

Figure 5.1. Generations of smart navigation devices (based on Viken 2010; Sullivan 2012; Newcomb 2013).

The academic and industrial progression in enhancing the accuracy of navigation solutions resulted in the modernization and launching of satellite constellations, as well as refinement and advancement of various navigation algorithms. Furthermore, the rise of more capable chipsets and the transition from geodetic-grade equipment to low-cost changed the tide of navigation. Currently, the fifth generation of smart devices exist with the potential of attaining better solution accuracy. A good example of such devices is the current generation of smartphones, most of which are equipped with single-frequency chips. There has been various research contributions showing centimetre-level RTK positioning using single-frequency chips in smartphones (Mongredien et al. 2016; Humphreys et al. 2016;

Odolinski and Teunissen 2017, 2019). Taking it up a notch, a potential paradigm shift has occurred with the release of dual-frequency chipsets which promises decimetre- to centimetre-level solution accuracy for the end user. Figure 5.2 shows and summarizes the key characteristics of all the generations of smart devices.

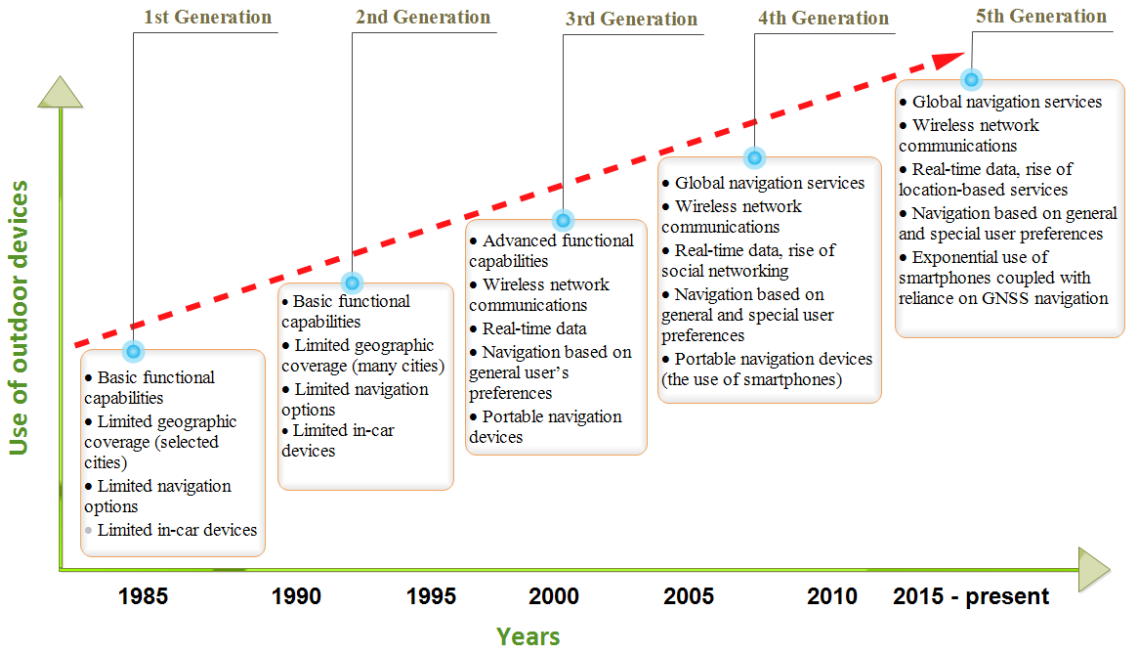

Figure 5.2. Characteristics of the generations of smart navigation devices (based on Karimi (2011)).

Currently, the chipset manufacturing industry has the potential of redefining positioning accuracy with regards to low-cost equipment. 2018 saw the emergence of ground-breaking dual-frequency chipsets designed for various applications, with the intention of improving GNSS solution accuracy. The smartphone market was revolutionized in September 2017 with the launch of Broadcom's BCM47755 dual-

frequency chipset. This introduction ignited a motivation to see more similar chipsets in the market (Murfin 2017). In February 2018, STMicroelectronics and U-blox launched their Teseo and F9 receiver chipsets, respectively, capable of tracking L1/L2 or L1/L5 frequencies and are intended to target the automotive industry (Cozzens 2018; Markowitz 2018). In the same month at the Mobile World Congress in Barcelona, Qualcomm unveiled their multi-GNSS, multi-frequency Snapdragon X24 LTE receiver with Intel also presenting a dual-frequency receiver prototype (Al Khairy 2018; Leather 2019).

To ascertain the level of accuracy that can be obtained by these recent smartphone chipsets, Trimble and Novatel investigated and achieved sub-metre positioning accuracy with BCM47755 and Tesco V chipsets, respectively (Riley et al. 2018; Abrahams 2018). These initial results demonstrated the possibility of attaining decimetre-level accuracy with smartphone chipsets. It is expected that as the positioning techniques continue to improve and hardware limitations are addressed, smartphone GNSS solution accuracy can be significantly improved. There are obvious challenges that threaten the possibility of higher accuracy and these include but are not limited to low-cost antenna attenuations, duty cycles and receiver power consumption. However, the recent capability added to smartphones to turn off the duty cycle unearths optimism among application developers and end-users that such challenges are either being dealt with or will be. It is also worth noting that by turning

off duty cycling, it consequentially increases the power consumption of the smartphone.

5.3 Smartphone raw measurement analysis

Four recently launched smartphones were investigated, namely the Xiaomi Mi8, Huawei Mate 20, Google Pixel 3 and Samsung S9. The characteristics of these smartphones are highlighted in Table 5.1. All the phones could track at least 3 out of the 4 GNSSs. And the Xiaomi Mi8 and Huawei Mate 20 had the capability to track dual-frequency L1/L5 signals.

Phones	Duty Cycle	Android version	GNSS	Measurements	Carrier-phase tracking
Xiaomi Mi8	Off	9	GRECJ	L1 and L5	Yes
Huawei Mate 20	Off	9	GREC	L1 and L5	Yes
Google Pixel 3	Off	9	GRE	L1	No
Samsung Galaxy S9	Off	9	GREC	L1	Yes
G: GPS, R: GLONASS, E: Galileo, C: BeiDou, J: QZSS					

Table 5.1. Test smartphones and the supported raw GNSS measurements.

All the smartphones were assessed against a SwiftNav Piksi and Topcon NET-G3A receivers. It is noteworthy to point out the cost differences between the GNSS chipsets in the phones in comparison to geodetic-grade receiver types. These

smartphone chips cost in the 10 US dollar range, while the Piksi and Topcon receivers, belonging in the relative low-cost and geodetic categories, costs a few hundreds to thousands of dollars, respectively. With a geodetic-grade antenna, resulting in geodetic-grade measurement quality, the Piksi and Topcon receivers were used to produce reference position solutions throughout the analyses described in the subsequent sections. Unlike the dual-frequency L1/L5 smartphones, the Piksi receiver tracks the L1/L2 legacy signals from all GNSSs. However, Topcon NET-G3A tracked L1/L2 signals for only GPS and GLONASS.

5.3.1 C/N_0 analysis of smartphone measurements

In assessing the measurement quality of the smartphones, the carrier-to-noise density ratio (C/N_0) of the received satellite signals was observed. It is well-known that one of the determining factors impacting the signal reception quality is C/N_0, which by definition, represents the power in the received signal compared to the power spectral density of the receiver noise (Misra and Enge 2006). Four main factors dictate the received signal power at the point antenna centre of mass: (1) power density of the incoming GNSS signal; (2) reception area of the antenna; (3) receiver antenna gain; and (4) satellite elevation (Braasch and Van Dierendonck 1999). Figure 5.3 shows the consistency of C/N_0 values over time for each smartphone, as well as the SwiftNav Piksi receiver. As illustrated in Figure 5.3(b)(c)(d)(e), low and irregular C/N_0 values from the smartphones over the observation period, potentially due to the cellphone-

grade GNSS receiver chipset and antenna which can impact signal reception. In contrast, the geodetic-grade, low-cost Piksi receiver shows reliable and high C/N_0 values with a consistent average of 45 dB-Hz due to a better antenna, as shown in Figure 5.3(a). The delimiting factor of using either Monolithic Microwave Integrated Circuit (MMIC) or monopole antennas in smartphone designs comes at a cost in the quality of GNSS signal reception (Riddle 2013).

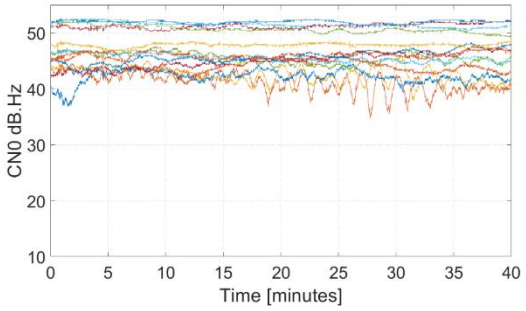

(a) SwiftNav Piksi

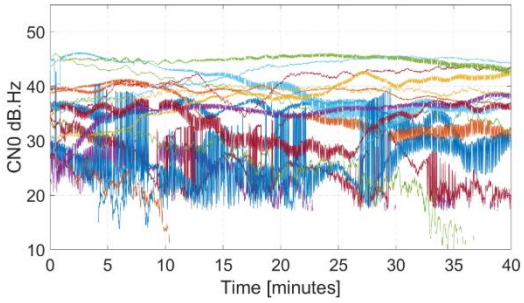

(b) Xiaomi Mi8

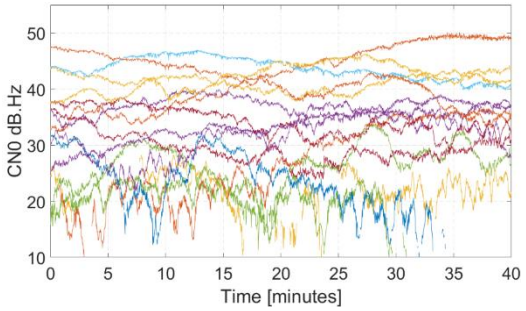

(c) Samsung Galaxy S9

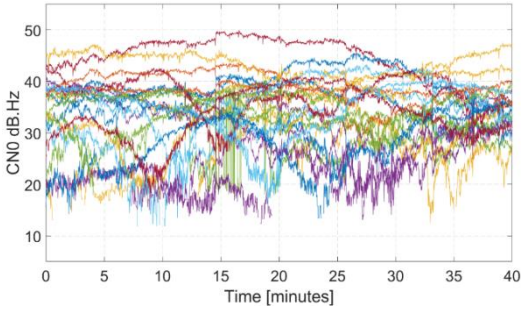

(d) Google Pixel 3

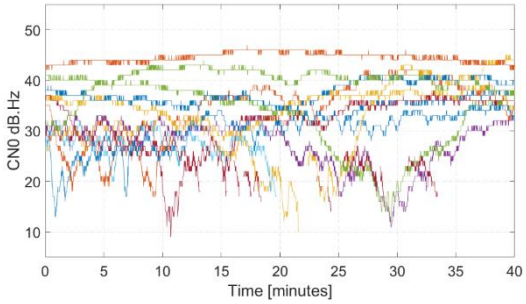

(e) Huawei mate 20

Figure 5.3. C/N_0 values for all observed sensors showing their levels of consistency over time. Sensors include (a) SwiftNav Piksi (b) Xiaomi Mi8 (c) Samsung Galaxy S9 (d) Google Pixel 3 and (e) Huawei Mate 20. Results are shown for DOY 65, 2019.

5.3.2 Signal noise and multipath analysis of smartphone measurements

However, C/N_0 analysis only tells part of the story in regard to the signal and measurement quality of each sensor. Only Xiaomi results, compared to SwiftNav Piksi, are shown because it was representative of the other smartphones analyzed. Presented in Figure 5.4 and Figure 5.5 are the noise and multipath analyses, respectively. Multipath is a result of reflection and diffraction when signals travelling from a transmitter to a receiver propagate via multiple paths (Bisnath and Langley 2001). This error effect is usually caused by reflected GNSS signals from surrounding objects and terrains such as trees and buildings. The measured distance between the receiver and satellite is increased due to the reflected signals. As a result, the pseudorange and carrier-phase measurements contain inherent errors due to the multipath effect. The magnitude of range error can reach up to 10 to 20 metres for

pseudorange measurements and up to 5 cm for carrier-phase measurements considering geodetic-grade equipment.

The coloured noise of the pseudorange and carrier-phase measurement consist of the multipath and noise which is a resultant of signal reflections around the satellite and receiver antenna, thermal noise in cable connectors, and the instrumental delay variations possibly due to temperature fluctuations which can occur at different levels: cables, receivers, antenna, splitters, amplifiers, etc. (Defraigne and Bruyninx 2007). Per satellite, the pseudorange multipath observable can be computed from the measured pseudorange and carrier-phase measurements. Considering two signals L1 and L2 on two frequencies f_1 and f_2, the pseudorange multipath/noise are represented in equations 5.1 and 5.2 :

$$MP_1 = P_1 - \left(1 + \frac{2}{\alpha - 1}\right) L_1 + \left(\frac{2}{\alpha} - 1\right) L_2 \qquad 5.1$$

$$MP_2 = P_2 - \left(\frac{2\alpha}{\alpha - 1}\right) L_1 + \left(\frac{2\alpha}{\alpha - 1} - 1\right) L_2 \qquad 5.2$$

where

$$\alpha = \left(\frac{f_1}{f_2}\right)^2$$

Figure 5.5 in particular shows the difference between the C/A-code and carrier-phase measurements, which represents the combined effect of pseudorange multipath and signal noise.

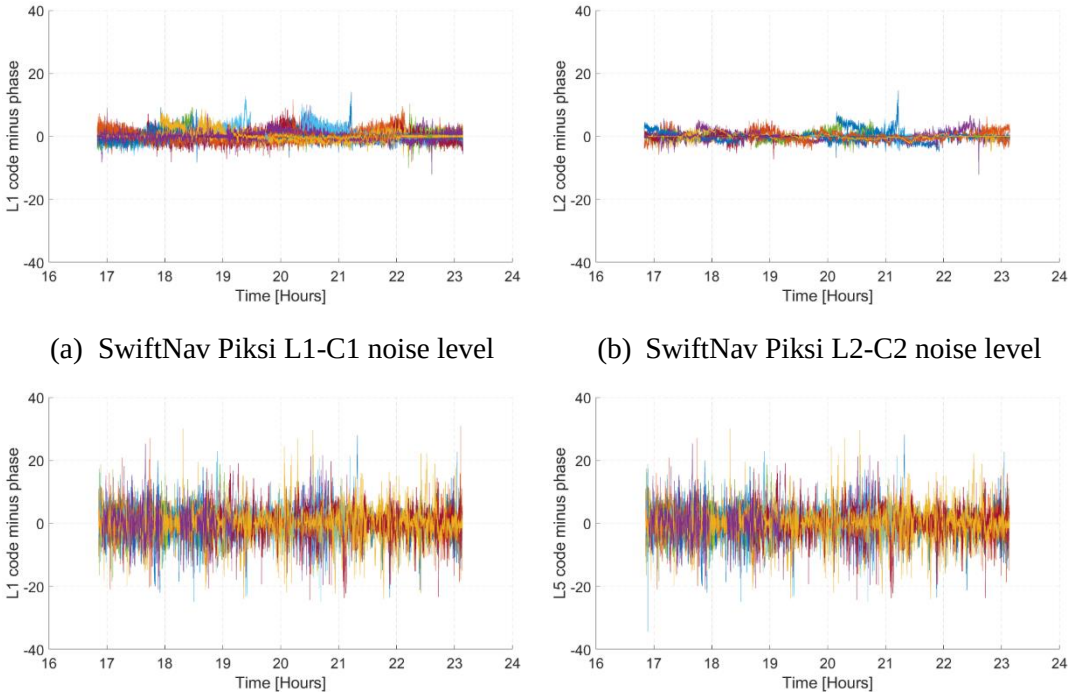

(a) SwiftNav Piksi L1-C1 noise level (b) SwiftNav Piksi L2-C2 noise level

(c) Xiaomi Mi8 L1-C1 noise level (d) Xiaomi Mi8 L5-C5 noise level

Figure 5.4. Signal noise level (in metres) for SwiftNav Piksi receiver and Xiaomi Mi8.

For completeness, multipath observables, representing the effect of multipath on the received signal, were formed for L1/L2/L5 signal bands as shown in Figure 5.5. Results are shown for 6 hours of data for DOY 82 of 2019. The mean of the difference between C/A-code and carrier-phase measurements was removed. Table 5.2 summarizes the rms of the residuals of the smartphones, as compared the SwiftNav

Piksi receiver. The magnitude of the multipath and signal noise level from the SwiftNav receiver was significantly lower in comparison to the smartphones. By differencing the noise levels of the two sensors in Table 5.2 and representing as a percentage, the multipath effect on the signals for SwiftNav Piksi was approximately 90% less than that of the effect on Xiaomi Mi 8. The signal noise level for Xiaomi Mi 8 told a similar story in comparison to the SwiftNav Piksi receiver. Given the limitations of the antenna of the smartphones, it was expected that the quality of the measurements will deteriorate in comparison to a geodetic-grade receiver and antenna (Gill et al. 2017; Gill 2018).

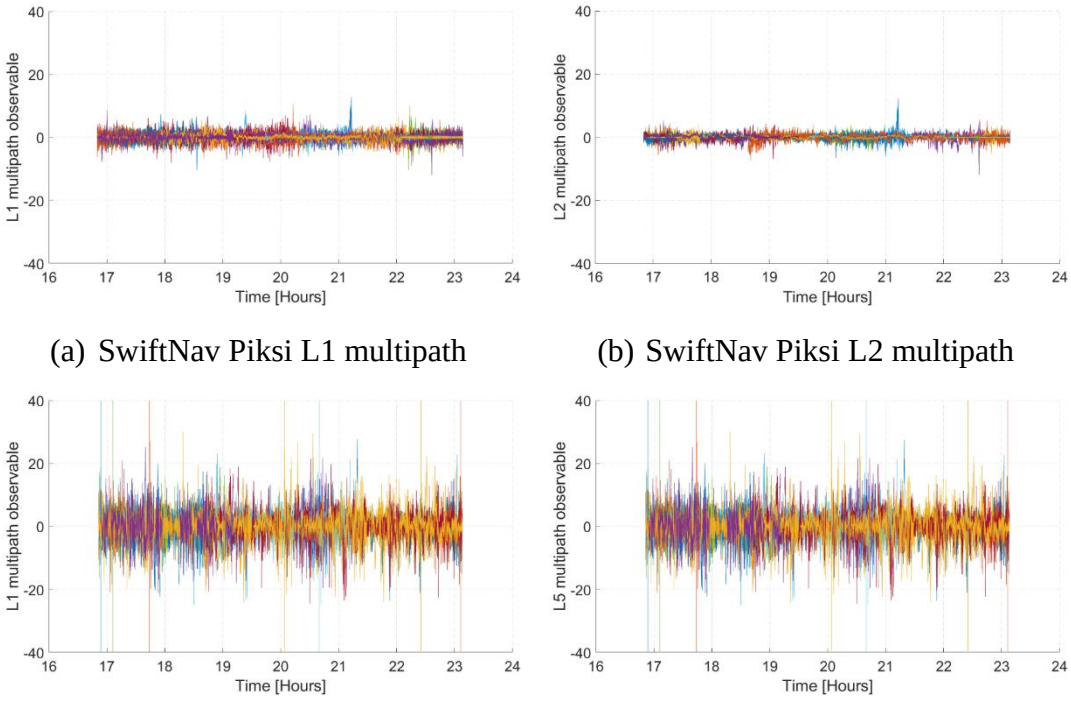

(a) SwiftNav Piksi L1 multipath (b) SwiftNav Piksi L2 multipath

(c) Xiaomi Mi8 Piksi L1 multipath (d) Xiaomi Mi8 Piksi L5 multipath

Figure 5.5. Multipath (in m) for SwiftNav Piksi receiver and Xiaomi Mi8.

Sensors	Measurement quality analysis (m)		Multipath analysis (m)	
	L1-C1	L2-C2/ L5-C5	MP1	MP2/MP5
SwiftNav Piksi	2.1	3.5	1.1	1.2
Xiaomi Mi8	17.9	19	16.1	16.5

Table 5.2. rms for the signal noise and multipath effect observed for Xiaomi Mi8 and SwiftNav Piksi.

5.4 PPP processing strategy for smartphone measurements

Shown in Table 5.3 are the processing parameters and settings used in the generation of results discussed in subsequent sections. The YorkU GNSS PPP engine was employed in processing the observations (refer to Chapter 1). Precise orbits and clocks from Centre National d'Etudes Spatiales (CNES) were used because of the availability of orbits and clocks for all available GNSS constellations.

Logging real-time data from the smartphones for PPP processing can be a challenge. It is imperative to note that not all available smartphones have the capability to log the raw GNSS data. A constantly updated list of available smart devices which log the raw GNSS measurements can be found at this link: https://developer.android.com/guide/topics/sensors/gnss. One prominent drawback is the duty cycling, which is used to regulate battery consumption on smartphone devices. Typically with the embedded GNSS chipsets, smartphones track and log GNSS measurements for about 200 ms before reserving power by shutting down for

about 800 ms (Banville and Van Diggelen 2016). This action is critical given the possibility of cycle-slip occurrences which impact positioning techniques such as Real-Time Kinematic (RTK) and PPP.

Processing parameters	YorkU GNSS PPP engine settings
Processing technique	Uncombined mode using raw strength of measurements
Antenna corrections	*IGS ANTEX
Satellite orbits and clocks	CNT (CNES)
Elevation mask	10°
GNSS system	GPS, GLONASS, Galileo and BeiDou
Observation processing mode	Single- and dual-frequency, static and kinematic processing
Data format	RINEX 3.x
Ionospheric mitigation	Slant ionospheric delays
Troposphere modelling	Hydrostatic delay: Davis (GPT) Wet delay: estimated Mapping function: Global Mapping Function (GMF)
**Phase centre offsets and variations for GPS L5, Galileo and BeiDou satellites were not corrected due to unavailability of corrections in the current ANTEX release. Smartphone and SwiftNav Piksi antenna corrections were also not corrected for the same afore-mentioned reason.*	

Table 5.3. YorkU PPP processing parameters for the smartphones.

The interaction with smartphone sensors through application programming interfaces (APIs) makes it possible for developers to extract information. The quest to

obtain raw GNSS measurements has been on-going for years before the introduction of Android's Marshmallow version. Through the APIs, NMEA (National Marine Electronics Association) formatted position, time and velocity (PVT) receiver data could be extracted (Sunkevic 2017). In 2018, Google publicly released their GNSS Analysis Tools as part of their API in the Android Nougat version, enabling the processing and analysis of GNSS measurements. This release enabled users to access the PVT and raw GNSS measurements directly. GNSSlogger, Google's android application, interfaces directly with smartphones and logs GNSS data in the NMEA format (Diggelen and Khider 2018). Since Google's launch, other loggers have been developed by various organizations for logging smartphone GNSS data in RINEX formats. These logging applications include but are not limited to Geo++ RINEX logger (Geo++ GmbH 2018), RINEX ON (Nottingham Scientific Ltd 2018), GalileoPVT (Crosta and Watterton 2018) and G-RitZ logger (Kubo 2018).

Table 5.4 summarizes some of the key details of the current RINEX GNSS android loggers for smartphone GNSS processing. For this research work, Geo++ RINEX Logger and RINEX ON were used.

Logger	Organization	Output Format	Logged data		
			Pseudoranges	Carrier phases	Ephemeris
GNSSLogger	Google	NMEA	Yes	Yes	Yes
Geo++ RINEX Logger	Geo++ GmbH	2.11 or 3.03	Yes	Yes	Yes
RINEX ON	Nottingham Scientific Ltd	3.03	Yes	Yes	Yes
GalileoPVT	European Space Agency (ESA)	CSV/NMEA raw Android measurements	Yes	Yes	No
G-RitZ Logger	Ritsumeikan University	2.11 and 3.03	Yes	Yes	No

Table 5.4. Currently existing sample RINEX GNSS loggers for smartphones.

5.5 PPP smartphone processing

In order to perform uncombined, dual-frequency PPP measurement processing, it was necessary that different sets of standard deviations had to be employed for each set of hardware. The values shown in Table 5.5 are derived empirically for each set of GNSS receiver hardware (Gill et al. 2017). The standard deviations are used to determine the relative weighting between the pseudorange and carrier-phase measurements. It is important to note that with the smartphones, the

noise on the pseudorange measurements increases. As shown in Table 5.5, the magnitude of the noise on the pseudorange measurements from the smartphones is much higher compared to the other relatively low-cost and geodetic-grade receiver measurements. The higher standard deviation can also be thought in-terms of de-weighting the noisier pseudorange measurements in the estimation process, as the a priori standard deviation determines the relative weighting.

Receiver	σ pseudorange (m)	σ carrier-phase (m)
Smartphones	4	0.04
SwiftNav Piksi	0.4	0.002
Topcon NET-G3A	0.1	0.001

Table 5.5. a priori standard deviations of pseudorange and carrier-phase measurements used in PPP processing for SwiftNav Piksi, Topcon NET-G3A geodetic-grade receiver and the smartphones.

In assessing the performance of the smartphones under investigation, the SwiftNav Piksi and Topcon NET-G3A dual-frequency L1/L2 receivers and geodetic-grade antennas were used to determine a reference solution. It was expected that the antenna type differences between the phones and the reference receivers would strike major distinctions in the solution qualities. The smartphone antennas are more susceptible to multipath effects from reflected signals, as shown in the previous

section, due to linear polarization. This phenomenon makes smartphone antennas more sensitive to poor quality GNSS signals, as compared to geodetic-grade antennas (Pathak et al. 2003; Zhang et al. 2018). Static and kinematic user dynamics were investigated and addressed in the subsequent sections with the duty cycle of the smartphones turned off.

5.5.1 Static dual-frequency PPP smartphone data processing

The static PPP analysis was performed by setting up an experiment on the roof of the Petrie Science and Engineering building at York University. Figure 5.6 shows the full setup of the experiment with the smartphone and SwiftNav Piksi receiver and antenna while Figure 5.7 illustrates the geodetic reference setup using Topcon NET-G3A receiver with a choke-ring antenna. For clarity, it must be pointed out that these two setups were not done on the same day. The reference setup was however done around the same time as the smartphones. The purpose of using the geodetic setup was to "ground truth" the point previously occupied by the smartphones and the SwiftNav Piksi receiver and antenna.

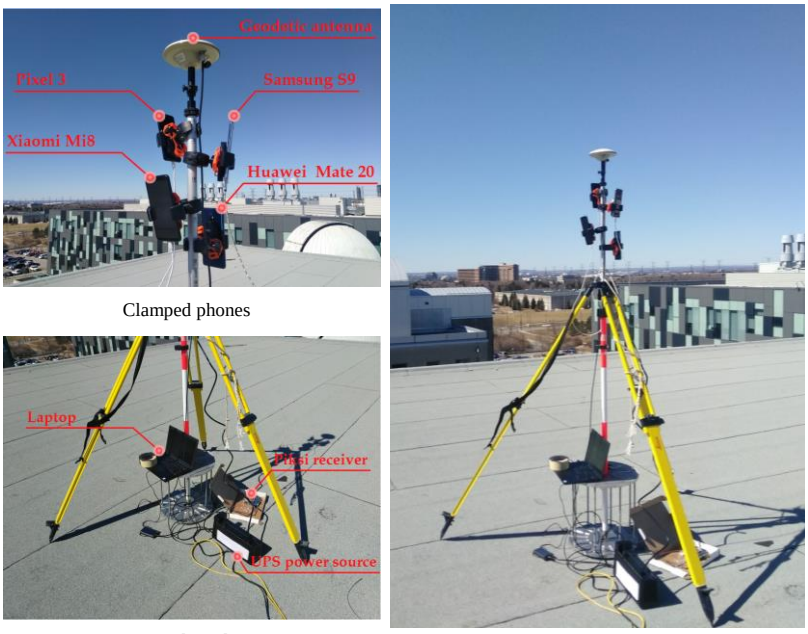

Figure 5.6. Setup of smartphones with SwiftNav Piksi receiver and antenna on DOY 82, 2019.

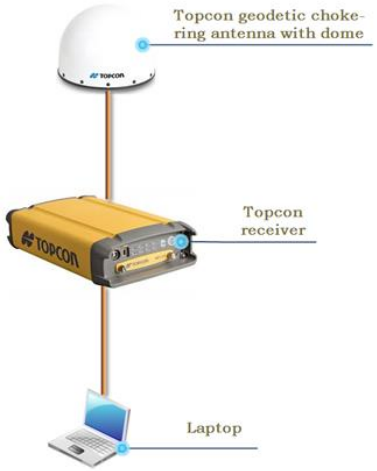

Figure 5.7. Setup of Topcon NET-G3A receiver with choke-ring antenna on DOY 83, 2019.

Data were collected for a period of 6 hours for DOY 82 in 2019. The SwiftNav Piksi antenna was mounted on a GNSS carbon fibre pole with the smartphones clamped to it. Though the preferred method to minimize multipath would have been to put the smartphones on the ground level, clamping was chosen to vaguely represent a user holding the phone. It must be noted that the purpose of this study is not to compare smartphones against one another, but rather to assess their performance in terms of positioning. Hence, the subsequent results have the smartphones labelled A to D. Presented in Figure 5.8 and Figure 5.9 are the horizontal component time series and scatter plot of two of the smartphones (A and B) with the capability to track L1/L5 signals. Solution results are compared to the SwiftNav Piksi and Topcon NET-G3A receivers.

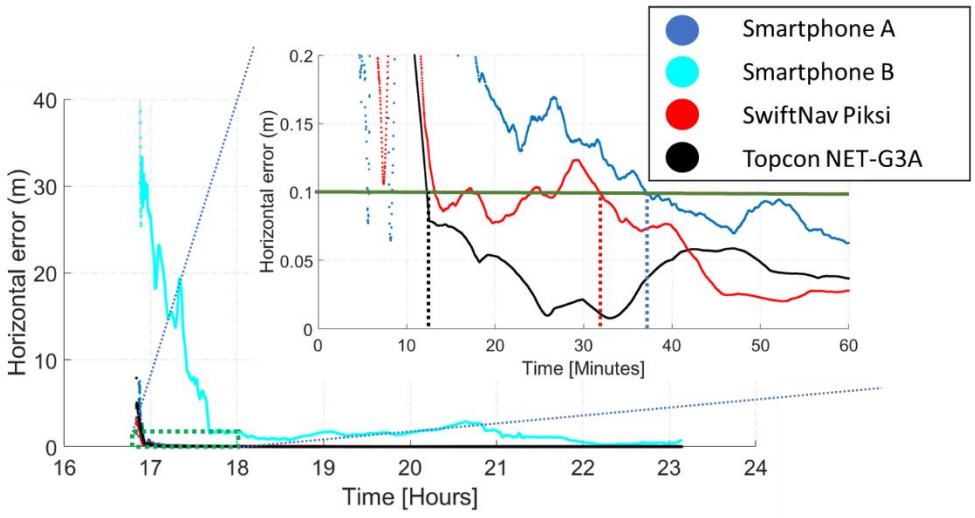

Figure 5.8. Smartphones A and B dual-frequency horizontal results (L1/L5) compared to SwiftNav Piksi (L1/L2) and Topcon NET-G3A (L1/L2).

The dual-frequency analysis for the smartphones A and B showed some interesting characteristics worth noting. Given both smartphones' ability to track a secondary frequency (L5), it was expected that they would act similarly in terms of PPP solution convergence. However, that is not the case. Defining convergence as the time taken for the solution to reach a horizontal error of 10 cm, Topcon, SwiftNav Piksi and smartphone A and solutions took 12, 32 and 38 minutes, respectively, to converge. However, the smartphone B solution did not converge. If the convergence threshold was redefined to be 50 cm in the horizontal component, it took 5 hours to converge.

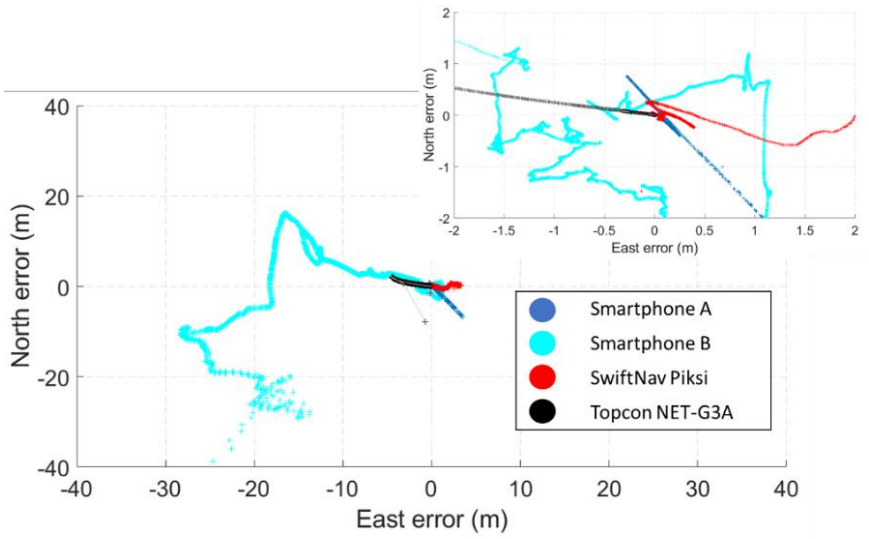

Figure 5.9. Smartphones A and B dual-frequency horizontal scatter plot. Results are compared to SwiftNav Piksi and Topcon NET-G3A.

The horizontal scatter plot, in Figure 5.8, tells a similar story, showing how smartphone B had tens of metres of error in the North and East components. Given the

significance of these deviations from the norm, an investigation ensued and led to some interesting conclusions.

The Geo++ logger was the default logger for all the smartphones. However, due to an Android update on smartphone B, it was not possible to use the Geo++ logger as it could not save the raw measurement logs. Hence the RINEX ON logger was used only for smartphone B. However, the pseudoranges and carrier-phase measurements were either bad or computed wrongly for most epochs. This behaviour was not the case for the other smartphones using the Geo++ logger. To ascertain that it was a logging issue, RINEX ON logger was used on the other smartphones and the same outcome of bad or wrong measurements was observed. It was thus interesting to note that the choice of logger appears to affect the measurement quality and ultimately, positioning performance. Given the inability to save data with Geo++ logger on smartphone B and wrongly computed measurement logs from using the RINEX ON logger, smartphone B was not included in the succeeding analyses. Hence, it must be stated that the position results from smartphone B, as presented in Figure 5.8, does not represent the actual results that can be obtained if there were no issues with data logging.

The exclusion of smartphone B from Figure 5.8 unearthed some interesting results which were unexpected. Shown in Figure 5.10 is the zoomed in version of Figure 5.8 showing the horizontal results of smartphone A, SwiftNav Piksi and Topcon

NET-G3A. Though the SwiftNav Piksi converged in 32 minutes, as compared to 38 minutes for smartphone A, both results were closely comparable given a 10 cm horizontal error threshold. Even more telling is the fact there are currently about 13 satellites with L5 capability but only an average of 5 can be seen at any point in time. This fewer number of observed GPS satellites in smartphone A was expected to impact the solution performance in contrast to the reference receivers, even though other GNSSs were similarly tracked and processed. However, this good surprise and outcome from smartphone A does not tell the entire story, especially when viewed from a residual analysis perspective.

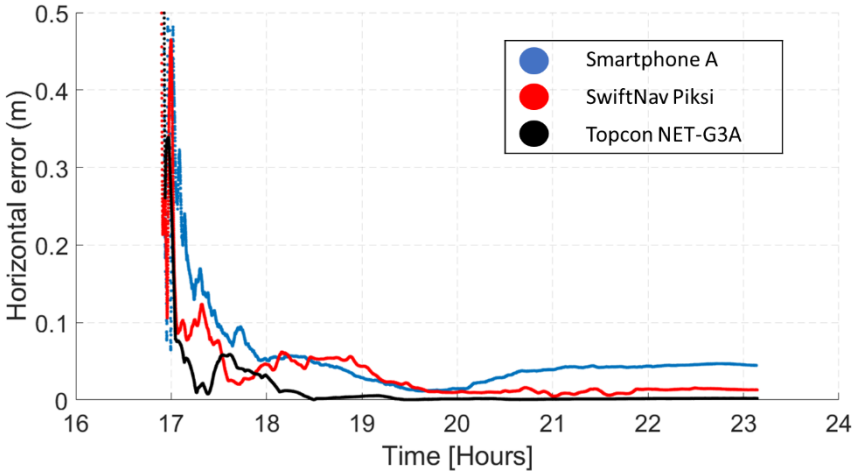

Figure 5.10. Smartphone A dual frequency horizontal results (L1/L5) compared to SwiftNav Piksi (L1/L2) and Topcon NET-G3A (L1/L2).

Presented in Figure 5.11 are the pseudorange and carrier-phase residuals for smartphone A and the reference receivers. Though they both follow typical noise-like residual trends, there are numerous jumps and outliers in the smartphone time series, and the residual magnitudes for both sensors are different in the range of tens of metres.

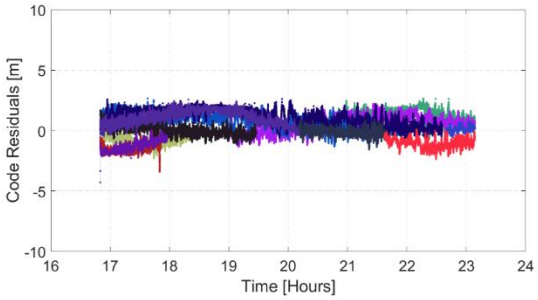

(a) Topcon NET-G3A code residuals

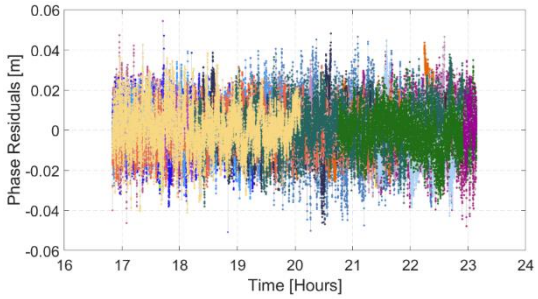

(b) Topcon NET-G3A carrier-phase residuals

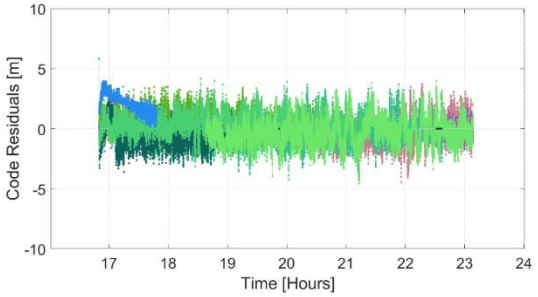

(c) SwiftNav Piksi code residuals

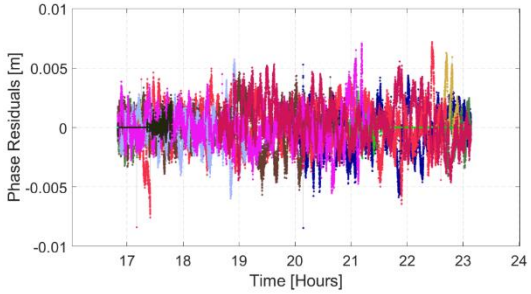

(d) SwiftNav Piksi carrier-phase residuals

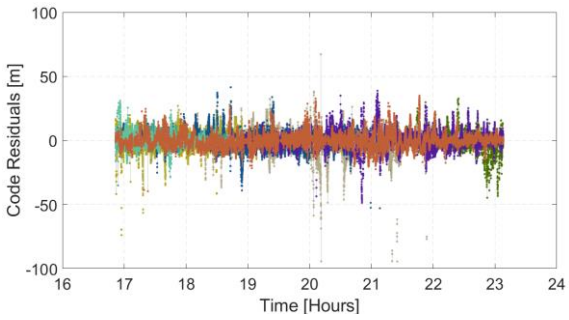

(e) Smartphone A code residuals

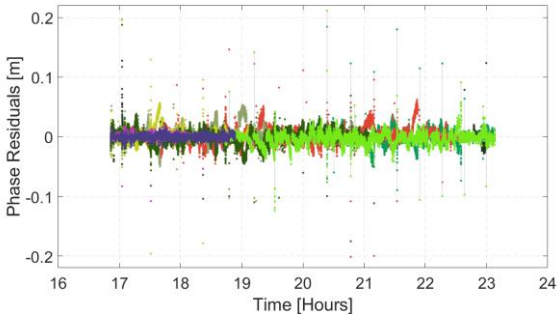

(f) Smartphone A carrier-phase residuals

Figure 5.11. Pseudorange and carrier-phase post-fit residuals for Topcon NET-G3A (Figure 5.11a, b), SwiftNav Piksi (Figure 5.11c, d) and smartphone A (Figure 5.11e, f).

The SwiftNav Piksi and Topcon NET-G3A pseudorange and carrier-phase residuals are at the 5 metre and sub-centimetre range, respectively. Table 5.6 summarizes the accuracy of positioning as well as the residuals for the sensors.

Sensors	**Position accuracy (rms) (in cm)**		**Residuals (rms) (in m)**	
	2D	3D	Pseudorange	Carrier-phase
SwiftNav Piksi	3	4	0.3	0.004
Topcon NET-G3A	0.3	0.6	0.3	0.007
Smartphone A	4	9	4.7	0.09

Table 5.6. Accuracy of positioning and pseudorange and carrier-phase post-fit residuals (in metres) for SwiftNav Piksi, Topcon NET-G3A and smartphone A.

Though the positioning accuracy for the sensors were similar at the centimetre level, the residuals for the SwiftNav and Topcon were significantly lower than smartphone A, as expected. Residual rms for the pseudoranges were 30 cm and 4.7 m for the reference receivers and smartphone A, respectively. The large residuals observed in the smartphone measurement processing can potentially be due to unmodelled hardware bias, high multipath and noise given the hardware limitations of the smartphone (Riley et al. 2018; Robustelli et al. 2019).

5.5.2 Static single-frequency PPP smartphone analysis

As shown in Table 5.1, the Samsung Galaxy S9 logs only single-frequency measurements. Complimentary to the dual-frequency results shown previously, it was necessary to process all the smartphones' data in single-frequency PPP mode. It must be noted however that smartphone D was excluded because it does not track carrier-phase measurements. In the same vein, smartphone B was also excluded due to the reasons previously highlighted in the dual-frequency PPP analysis. The ionospheric effect was mitigated using Global Ionospheric Maps (GIM). Shown in Figure 5.12 to Figure 5.13 are the single-frequency horizontal PPP solutions and residuals for smartphones A and C as compared to SwiftNav Piksi.

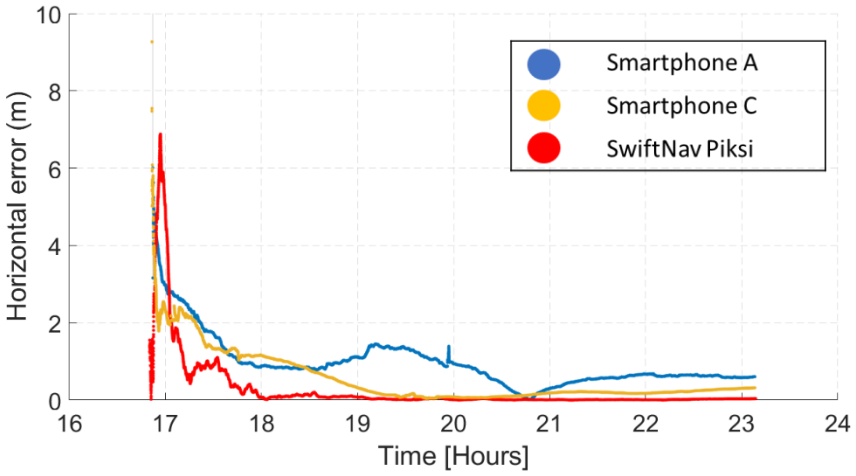

Figure 5.12. Single-frequency horizontal results (L1/C1) for smartphones A and C compared to SwiftNav Piksi (L1/C1).

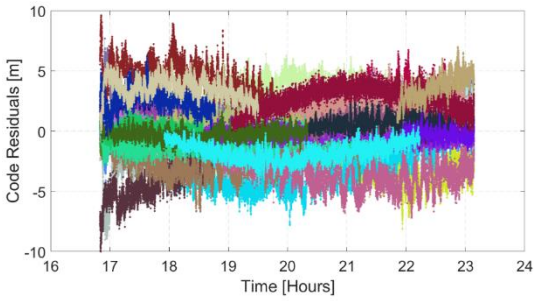

(a) SwiftNav code residuals

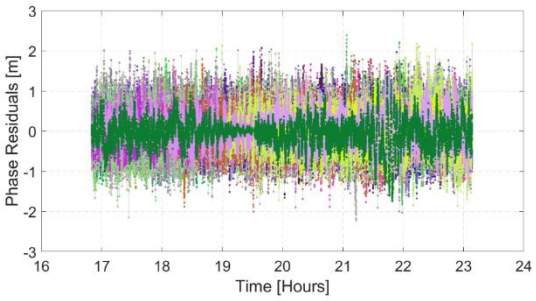

(b) SwiftNav carrier-phase residuals

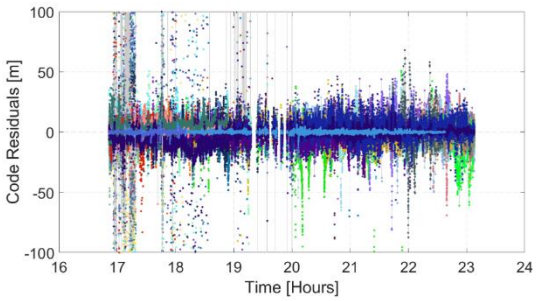

(c) Smartphone A code residuals

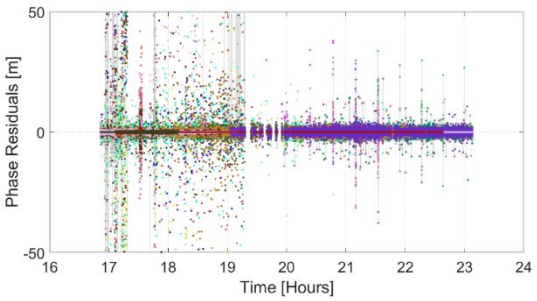

(d) Smartphone A carrier-phase residuals

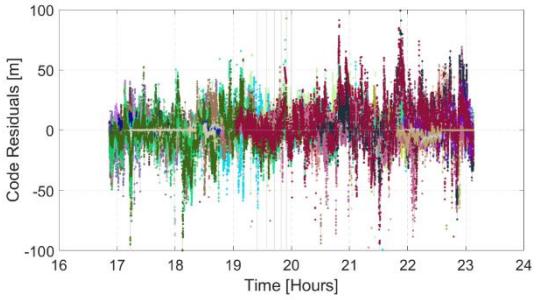

(e) Smartphone C code residuals

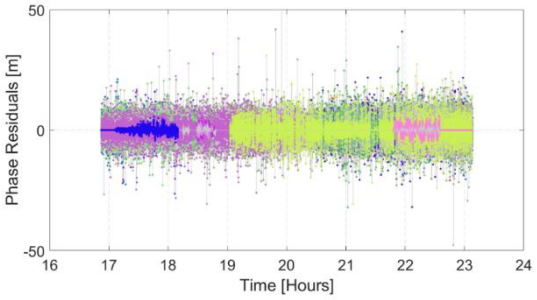

(f) Smartphone C carrier-phase residuals

Figure 5.13. Pseudorange (a,c,e) and carrier-phase (b,d,f) post-fit residuals for smartphones A and C.

Defining the convergence threshold as 20 cm horizontal error, solutions of SwiftNav Piksi and smartphone C converged in 54 minutes and 2 hours, respectively. The performance from SwiftNav Piksi was expected given its “better” hardware, but the steadiness of the solution from smartphone C as well as its faster PPP initialization,

is interesting. Smartphone A did not converge at the defined convergence threshold. However, similar to smartphone C, its initialization was better than SwiftNav Piksi. There were also significant deviations in the East and North components for the smartphones and SwiftNav Piksi, as depicted in Figure 5.14. The residual analysis showed very noisy carrier-phase residuals due to the usage of GIM which corrects about 75% of the ionosphere, as well as unmodelled hardware biases and noise.

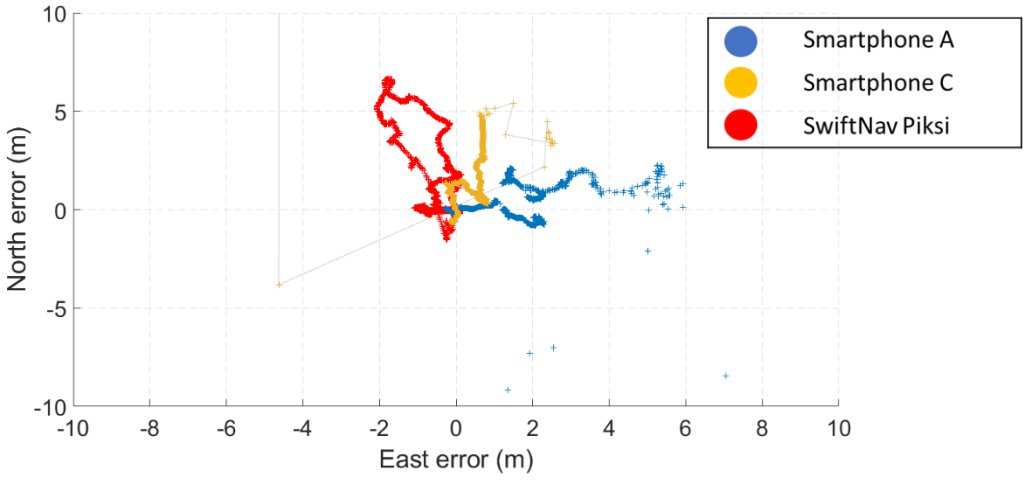

Figure 5.14. Smartphones A and C single-frequency horizontal scatter plot. Results are compared to SwiftNav Piksi.

5.5.3 Static smartphone PPP versus internal smartphone standard positioning performance.

Given that the internal solutions from the smartphones, obtained from the logged NMEA logs, were standard positioning results, it was necessary to compare all

the smartphones. Shown in Figure 5.15 are the results from the internally logged standard positioning results from smartphones A, C and D. Smartphone D logged on pseudoranges, hence it was processed in pseudorange-only PPP mode. As evidenced in Figure 5.16, the PPP solutions were less noisy with less East and North component deviations in contrast to the internal solutions from the smartphones.

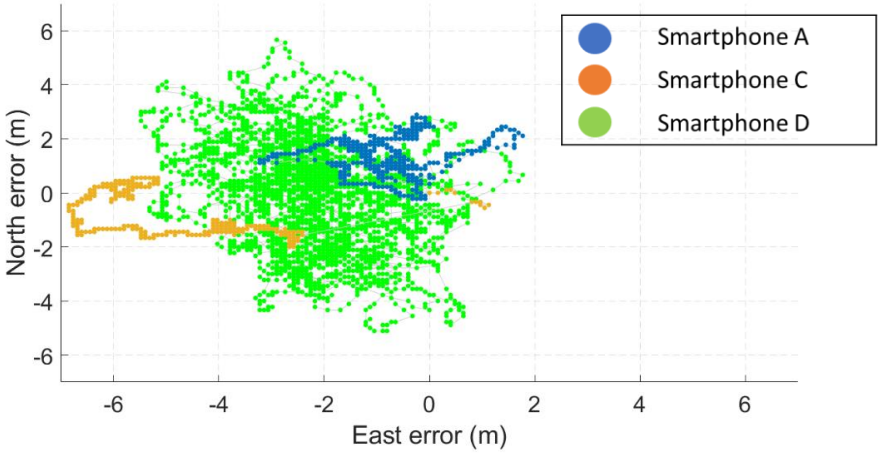

Figure 5.15. Internal standard positioning solutions for smartphones A, C and D.

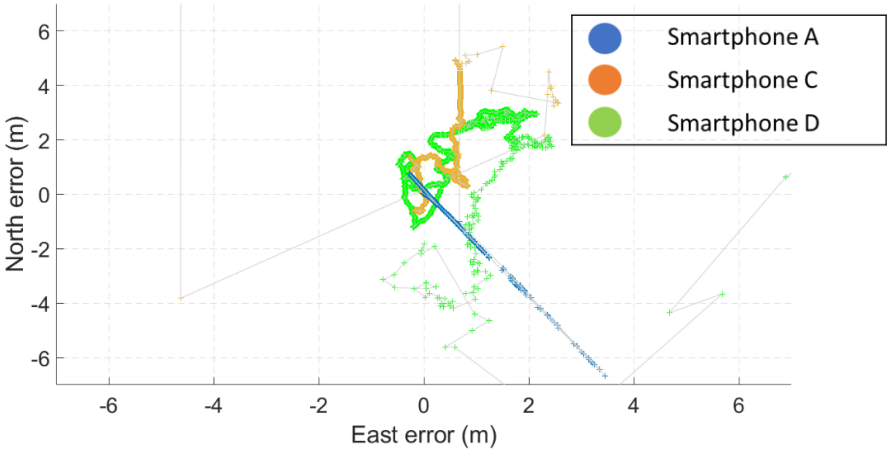

Figure 5.16. PPP positioning solutions for smartphones A, C and D.

5.5.4 Kinematic PPP smartphone data processing.

In order to assess the performance of the smartphones in kinematic mode with multi-GNSS PPP processing technique, a test experiment was setup with a pre-determined route with data collected for 45 minutes. Shown in Figure 5.17 is the entire setup.

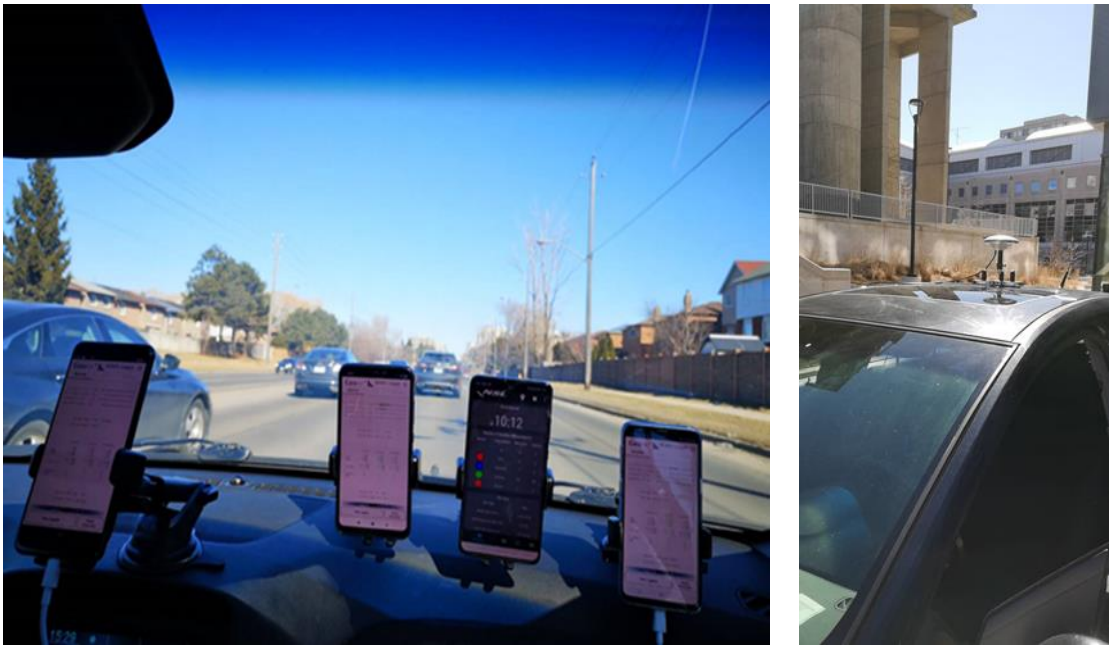

(a) Mounted smartphones on the dashboard (b) SwiftNav Piksi antenna

Figure 5.17. Kinematic test setup with (a) Xiaomi Mi8, Google Pixel 3, Huawei Mate 20 and Samsung Galaxy S9 (from left to right) (b) SwiftNav Piksi antenna is shown mounted on the roof of the vehicle.

The test route was near York University and covered approximately 17 km. Setting up the smartphones involved stabilizing them using car phone mounts on the dashboard of a vehicle. The SwiftNav Piksi was used as a reference solution and had its antenna mounted on the roof of the vehicle with a magnetic mount.

From a bird's eye view shown in Figure 5.18(a), all smartphones appear to be on track except for a few deviations from smartphone A during some traffic stops. Given smartphone A was the only device with L1/L5 capability being processed in L1/L5 PPP mode, the number of processed satellites was significantly reduced. High multipath also contributed to the deviations noticed for smartphone A. Again, for reasons previously stated, smartphone B was excluded from this experiment.

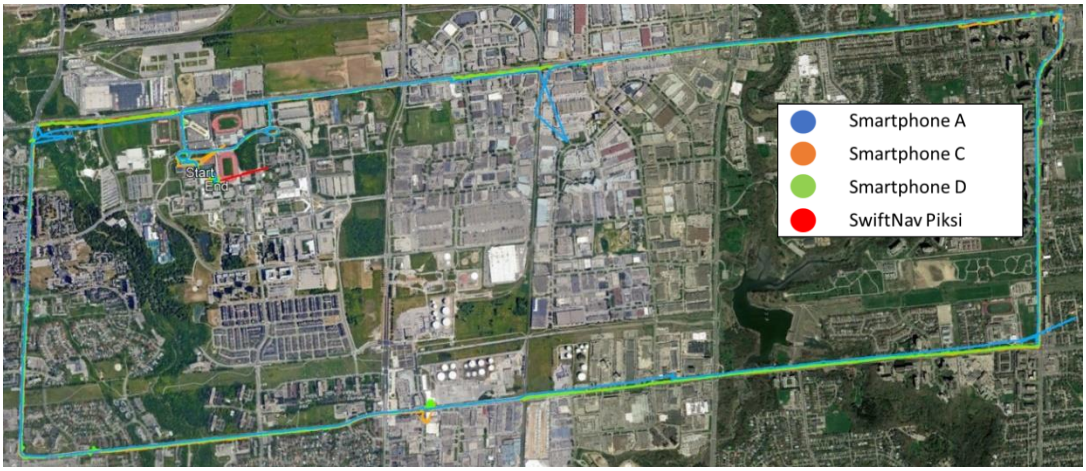

(a) Trajectory of kinematic test as seen from a bird's eye view

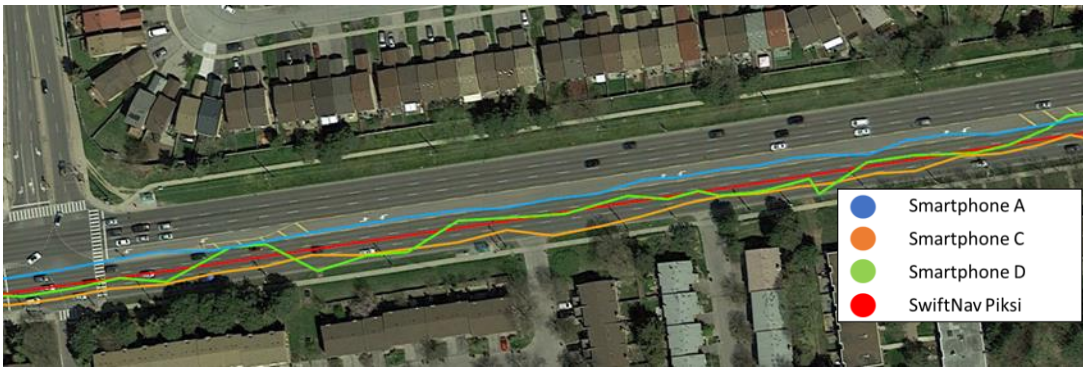

(b) Zoomed in portion of road detailing the trajectory of the smartphones

Figure 5.18. Results for kinematic run: (a) general trajectory (b) detailed zoomed in portion of road showing the performance of the smartphones and SwiftNav Piksi receiver.

However, a critical look at the performance of the smartphones, as shown in Figure 5.18(b) indicates some interesting behaviour. The SwiftNav Piksi geodetic receiver and antenna show the best results as expected for the obvious reasons of more capable hardware. Smartphone D, being the only pseudorange-only tracking device, show tens of metres in comparison to the geodetic reference receiver. However, smartphones A and C, L1/L5 and L1/C1 capable respectively, are relatively comparable, on wide stretches of the road, to the SwiftNav Piksi. However, that is not the case when the car followed sharp bends or roundabouts. Shown in Figure 5.19 are the performances of the smartphones in comparison to the reference receiver.

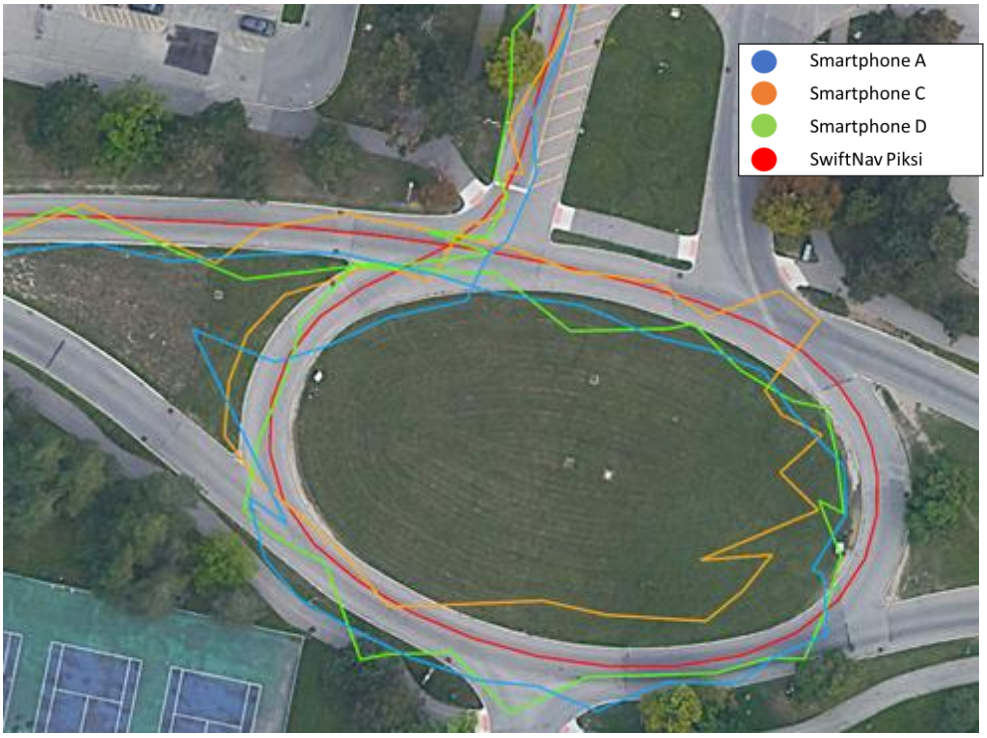

Figure 5.19. Results for kinematic run: (a) general trajectory (b) detailed zoomed in portion of road.

It was interesting to see how well the SwiftNav Piksi performed, given it was a relatively low-cost receiver with geodetic grade components. The performance of the smartphones however, generally deteriorated around the bends and roundabouts due to significant drops in satellite number due to ever-changing satellite geometry. With the phones being inside the car, this was expected, along with significant multipath. Shown in Figure 5.20 are the kinematic pseudorange and carrier-phase residuals of the smartphones investigated as well as SwiftNav Piksi, which portrayed expected characteristics.

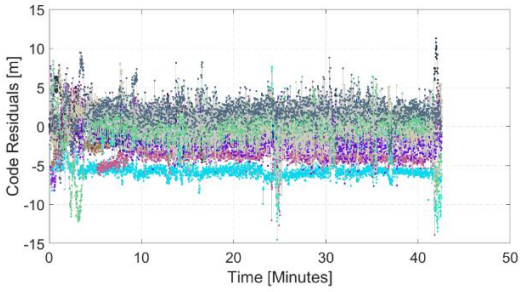

(a) SwiftNav code residuals

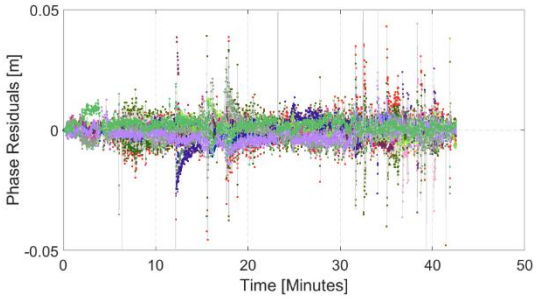

(b) SwiftNav carrier-phase residuals

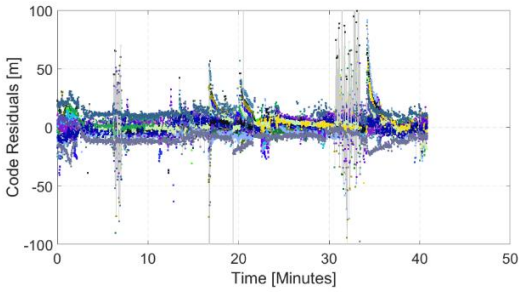

(c) Smartphone A code residuals

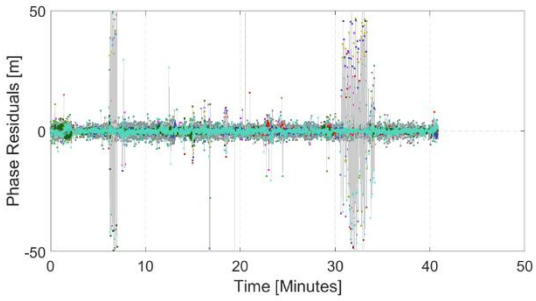

(d) Smartphone A carrier-phase residuals

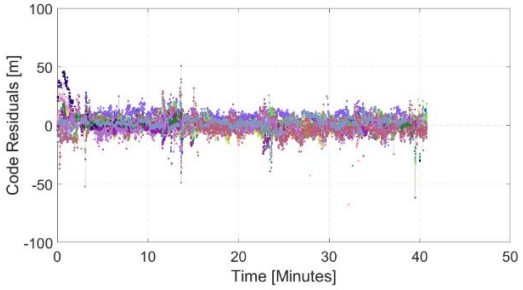

(e) Smartphone C code residuals

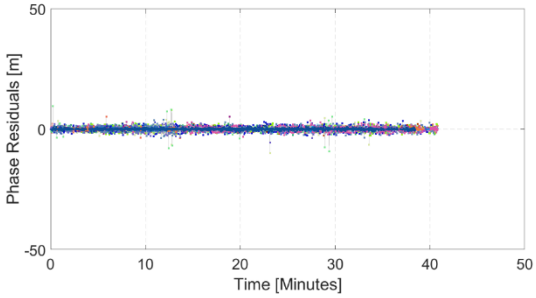

(f) Smartphone C carrier-phase residuals

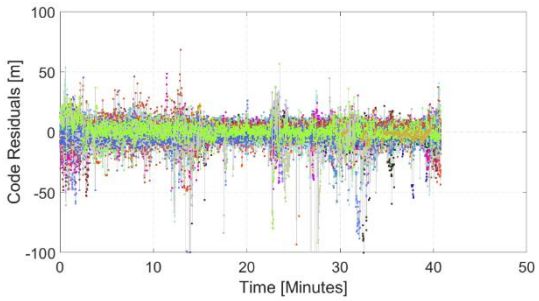

(g) Smartphone D code residuals

Figure 5.20. Kinematic pseudorange and carrier-phase residuals of the smartphones in comparison to SwiftNav Piksi.

The residuals from the SwiftNav Piksi receiver was well-behaved and consistent with what was expected, given the dynamics of the car and process noise employed in the data processing. However, the pseudorange and carrier-phase residuals for all the smartphones were a magnitude of order worse in comparison to the SwiftNav Piksi receiver. As shown in Table 5.7, the pseudorange residuals for all the smartphones were consistent at the few metres level. The positioning accuracy for the smartphones were all at the metre-level, compared to decimetre range for SwiftNav Piksi.

Sensors	Position accuracy (rms)		Residual analysis (rms)	
	2D	3D	Pseudorange	Carrier-phase
SwiftNav Piksi	0.58	0.79	0.35	0.004
Smartphone A	6.09	7.95	5.8	1.74
Smartphone C	5.85	6.34	3.64	0.31
Smartphone D	7.07	8.47	6.97	~

Table 5.7. Accuracy of positioning and pseudorange and carrier-phase post-fit residuals (in metres) for SwiftNav Piksi and smartphones in kinematic data processing.

5.6 **Summary**

The positioning results from the dual-frequency chipsets showed improvements in accuracy and reductions in convergence time over a 6-hour period and especially over the first few minutes. The smartphones' performance was compared with that of a geodetic and relative low-cost receiver. Experiments were conducted in multiple different scenarios with the aim of testing the smartphones under different multipath profiles. For static PPP results, a static setup enabled the collection of 6 hours of data. Kinematic solutions were also obtained by using a car on a selected route. It was observed that the smartphones raw measurements showed higher multipath profiles and lower C/N_0 compared to the geodetic and low-cost receiver. Given the quality of the raw measurements, appropriate measurement weighting and

software augmentation was made while the convergence threshold in our York PPP engine was set to 10 and 20 cm for dual-and single-frequency modes, respectively. An elevation and C/N_0 threshold of 10° and 15 dB-Hz were also used, respectively, as checks to improve data quality. Single-frequency PPP processing with smartphones showed an average horizontal root mean square (rms) error of 60 cm. However, with dual-frequency multi-GNSS PPP processing, the horizontal rms error was an average of 40 cm. The good news of having duty cycle turned off for the smartphones provided consistent measurements for kinematic solutions. For both static and kinematic scenarios, decimetre-level to metre-level horizontal error was achieved, respectively. In summary, the chapter addressed and answered the following research objective questions:

(1) What is the typical performance when using the raw measurements from these smartphones in multi-GNSS PPP processing either in static or kinematic scenarios?

In static GNSS PPP processing with a smartphone equipped with a dual-frequency chipset, it is possible to obtain decimetre-level accuracy in 38 minutes, comparable to geodetic-grade receiver and antenna. A kinematic scenario showed an accuracy of a few metres.

(2) Given the limitation that the hardware components of the smartphones present, what PPP processing changes can be implemented to make use of the raw measurements from smartphones?

As shown in this research contribution, the signal noise level on the raw measurements from smartphones can be approximately 90% more than that of a geodetic-grade equipment. The C/N_0 of the satellites tracked can be significantly low as 10 dB-Hz. It is thus imperative to implement necessary measurement weighting schemes to accommodate these measurements in PPP processing.

(3) What is the best performance that can be achieved with multi-GNSS PPP given the usage of the smartphones by the user?

Through an experimental setup, the GNSS PPP solution converged in 38 minutes, assuming a horizontal error threshold of 10 cm. The 10 cm error threshold represents a strict tolerance for very precise applications. The convergence is expected significantly improve if the threshold is increased further depending on the user application.

CHAPTER 6 APPLICATION OF PPP AUGMENTATION TO LOW-COST GNSS RECEIVER MEASUREMENTS

The recent market releases of state-of-the-art low-cost receivers capable of tracking multi-GNSS signals or multiple frequencies, offers a glimpse into the potential level of improvement in the user solution accuracy. This chapter investigates various low-cost, multi-GNSS receiver chipsets, including: Piksi Multi Module, Unicorecomm Nebulas II and U-blox F9 sensors. The tests which were performed were grouped into 3 main categories: Measurement quality analysis, uncombined PPP solution processing and residual analysis. Static and kinematic scenarios were considered in all of the tests performed on the chipset sensors. Solutions were obtained from geodetic receivers to serve as a reference. To appreciate the quality of the observations obtained from the sensors, multipath observables were formed to generate a full multipath profile.

6.1 Introduction

Over the past decade, Global Navigation Satellite Systems (GNSSs) has undergone an evolution and ultimately is having an impact on user solution performance. The availability of more GNSSs with modernized multi-frequency signals has revolutionized both the receiver manufacturing and technology industries, as well as

positioning algorithms (Seepersad et al. 2017; Aggrey and Bisnath 2017b, a; Bisnath et al. 2018; Aggrey 2018). This progression opens the door to a vast number of potential applications including but not limited to location-based services (Michelon and Bouchired 2003; Amundson 2005; Tomatis et al. 2008; Chen et al. 2009), autonomous navigation (Bowyer et al 2016.; Neri et al 2018.; Nielsen and Dehghanian 2014; Rispoli et al.; Tijero et al 2018.; Vydhyanathan et al 2007.; Zhang et al. 2008; Asari et al. 2016), Internet-of-Things (IoT) (Katsumoto et al. 2017; Lucas-Sabola et al. 2017), etc. The user interest in such applications stems from the idea that geodetic-grade receivers may not be necessary for quality position solutions. It would be equally possible to use low-cost receivers to obtain relatively equivalent results, as compared to their geodetic grade counterparts (Beran et al. 2005; Kirkko-Jaakkola et al. 2015; Todd Humphreys et al. 2016; Gill et al. 2017). Though it is possible to obtain centimetre level of accuracy using high end geodetic grade receivers, the cost of them poses a challenge. It is important to note that the idea of investigating these receiver modules is not to either advocate for or promote these brands. This chapter aims to address how the accuracy of low-cost receivers have improved over the years from the hardware perspective, as well as show how that reflects in the position domain.

With the growth of location-based services (LBS), new market areas are emerging and influencing the receiver manufacturing industry. From automotive and IoT to social networking and sports, the diversity of applications using multi-GNSS low-cost

receiver chipsets is expanding (Cui et al. 2017). In recent years, a significant focus has been shown by receiver chipset manufacturers in providing relatively low-cost equipment but with geodetic grade accuracy standards. Broadcom, Qualcomm and MediaTek have entered into the smartphone market (Wang 2018; EGSA 2018; Do 2018), while U-blox and STMicroelectronics have their sight on automotive and IoT market segments (U-blox 2011, 2013; Inside GNSS 2016; STMicroelectronics 2019; Synopsys 2019). Multi-constellation and multi-frequency chipsets have become the standard with increased availability for the mass market as of 2018. The current expanse of receiver chipsets has led to classifications with a range from high-accuracy geodetic chipsets to low and ultra-low-cost products. The differentiation among the current receiver chipsets is mostly driven by power consumption and cost.

As the next generation of low-cost, multi-frequency, multi-constellation GNSS receivers, boards, chips and, to a lesser extent, antennas enter the market, this chapter seeks to investigate the utility of the PPP approach in processing raw measurements from these sensors. Experiments collecting data from a number of GNSS sensors in a number of static and kinematic benign, realistic, suburban and urban environments are presented. The research questions intended to be addressed include: (1) What is the performance of current low-cost geodetic-grade receiver sensors? (2) Given the quality of observations of relative low-cost sensors in contrast to geodetic grade receivers, what adaptive measurement weighting can be used to enhance the solution

performance? (3) Through multi-GNSS PPP processing, what performance metrics can the end user adopt as a guide when it comes to low-cost receiver applications?

6.2 **Receivers used and multi-GNSS PPP data processing strategy**

The data processing strategy used in the processing of datasets is similar to what is described in Table 5.3. Precise orbits and clocks from GFZ (German Research Centre for Geosciences) were used because of the availability of orbits and clocks for all available GNSS constellations.

6.2.1 Receivers investigated

In a compact form, the U-blox F9 positioning module provides multi-GNSS capability intended for industrial applications. It is integrated with U-blox multi-band RTK technology for centimetre-level accuracy. Using advanced jamming and spoofing detection technologies, U-blox F9 claims an insurance towards the security of positioning and navigation in general (Cozzens 2018; U-blox 2019). Originally designed for autonomous systems, SwiftNav Piksi multi-GNSS module also offers centimetre-level accuracy and faster RTK convergence time (Varela et al. 2019).

Similarly, Unicorecomm Nebula II is a multi-GNSS high-precision next-generation module developed by Unicore Communications. It supports GPS, GLONASS, Galileo, BeiDou and QZSS satellite systems. The module also supports

triple-frequency RTK technology and is intended for high-precision positioning. Shown in Table 6.1 is the summary of the chipsets used in this research contribution highlighting their relative low-cost prices.

Receiver	Manufacturer	Price (per unit)
SwiftNav Piksi	SwiftNav	~$2300 USD*
U-blox F9	U-blox	~$150 USD
Unicorecomm Nebula II	Unicore Communications	~$250 USD
*This price is for the SwiftNav evaluation kit which includes two Piksi Multi-GNSS Modules, two evaluation Boards, two high-quality survey-grade GNSS antennas, two high-performance radios, cables and accessories.		

Table 6.1. Low-cost geodetic-grade receiver types investigated.

For a thorough static analysis, 24 hours of static data were collected on the roof of the Petrie Science and Engineering building, York University. Figure 6.1 shows the setup structure of three low-cost receiver chipsets used in data collection. Acting as a reference for ground truthing, a Topcon receiver with choke-ring antenna was also used.

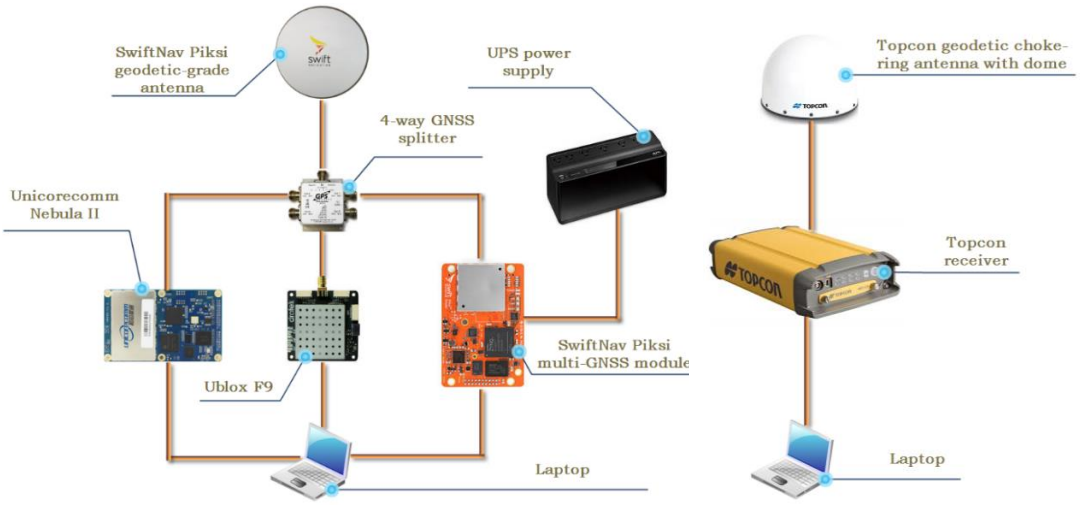

(a) Setup for low-cost receiver chipsets

(b) Setup for geodetic reference

Figure 6.1: Static equipment setup for (a) low-cost receiver chipsets and (b) geodetic reference receiver and antenna.

6.2.2 Measurement weighting scheme employed

In order to perform uncombined dual-frequency PPP using the low-cost receiver chipsets, it was necessary that different set of standard deviations had to be employed for each set of hardware. The values shown in Table 6.2 are derived empirically for each set of GNSS receiver hardware. The standard deviations are used to determine the relative weighting between the pseudorange and carrier-phase measurements. It is important to note that with the relatively low-cost hardware, the noise on the pseudorange measurements increases, whereas the quality of the carrier-phase

measurements was observed to be comparable to the geodetic-grade measurements. As shown in Table 6.2, the magnitude of the noise on the pseudorange measurements from U-blox F9 is much higher compared to the other low-cost and geodetic-grade receiver measurements. The reason for down weighting the U-blox F9 was primarily due to the assumption of potential higher hardware biases given its price tag. The higher standard deviation can also be thought in-terms of de-weighting the noisier pseudorange measurements in the estimation process, as the a priori standard deviation determines the relative weighting.

Receiver	σ pseudorange (m)	σ carrier-phase (m)
U-blox F9	4	0.02
SwiftNav Piksi	0.4	0.002
Unicorecomm Nebula II	1	0.02
Topcon	0.1	0.001

Table 6.2. a priori standard deviations of pseudorange and carrier-phase measurements used in PPP processing for U-blox F9, SwiftNav Piksi, Unicorecomm Nebula II and Topcon geodetic-grade receiver.

6.3 Measurement quality analysis

One of the determining factors that defines the ranging performance of GNSS receivers is signal-to-noise-ratio (SNR) (Ray et al. 2001; Lu et al. 2005; Misra and Enge 2006). Typically, SNR values are low at lower elevation angles compared to

those at zenith. Shown in Figure 6.2, Figure 6.3 and Figure 6.4 are the SNR values of the raw measurements observed against time and satellite elevations.

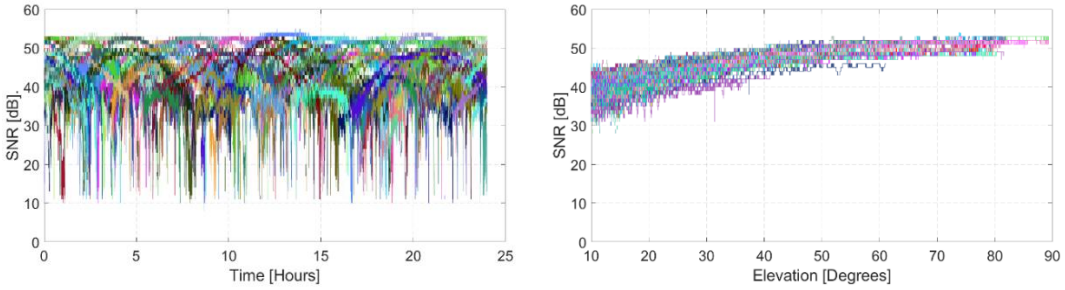

(a) U-blox F9 SNR against time

(b) U-blox F9 SNR against elevation

Figure 6.2: SNR at different elevation angles and against time from U-blox F9.

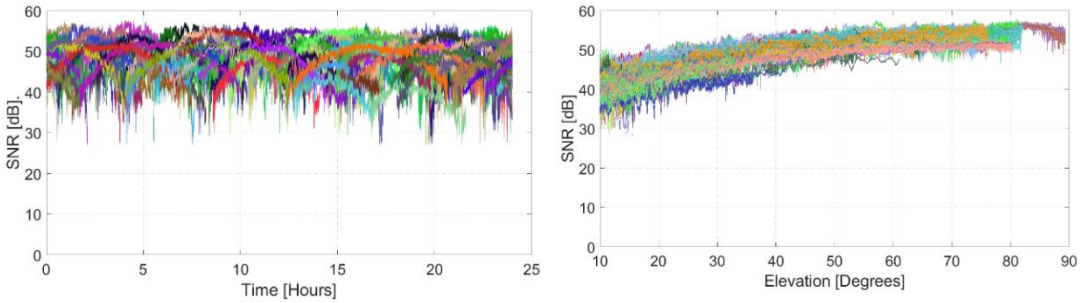

(a) SwiftNav Piksi SNR against time

(b) SwiftNav Piksi SNR against elevation

Figure 6.3: SNR at different elevation angles and against time from SwiftNav Piksi.

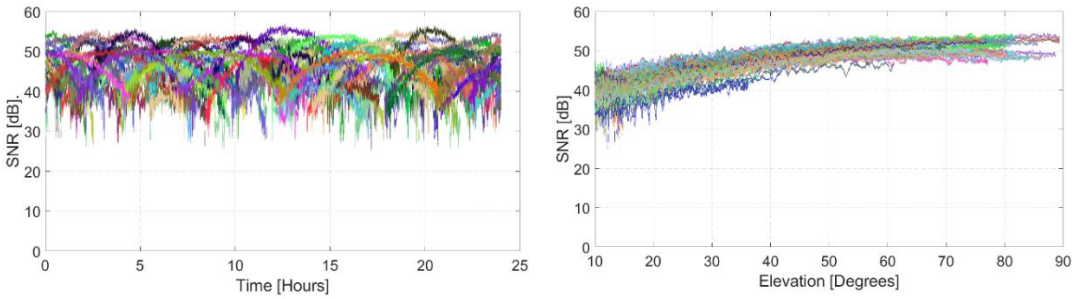

(a) Unicorecomm SNR against time

(b) Unicorecomm SNR against elevation

Figure 6.4: SNR at different elevation angles and against time from Unicorecomm Nebula II.

As illustrated in Figure 6.2, Figure 6.3 and Figure 6.4 the relatively high SNR proportions of a signal from the geodetic-grade low-cost equipment points to the how the definition of low-cost is changing in regards to receiver chipsets and hardware. All the three receiver modules examined showed strong signal strengths as was expected given their geodetic grade hardware. The average SNR for all the three multi-GNSS modules ranged between 35 to 55 dB. Shown in Figure 6.5, Figure 6.6 and Figure 6.7 are the measurement noise levels and multipaths for all the receiver chipsets under investigation.

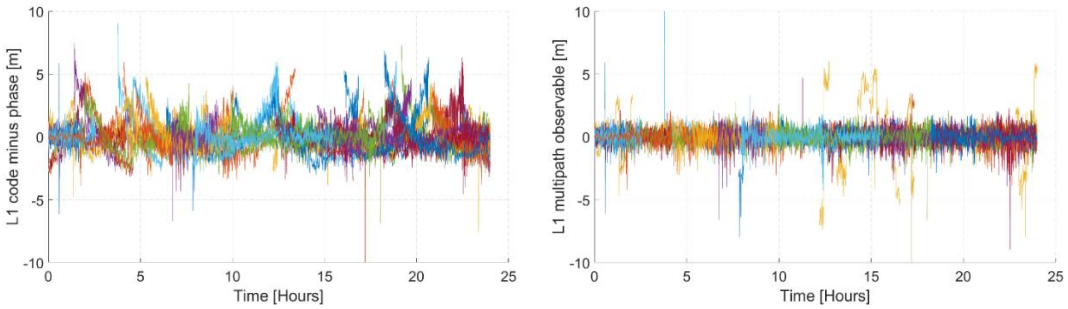

(a) U-blox F9 measurement noise (b) U-blox F9 multipath

Figure 6.5: (a) Measurement noise level and (b) multipath effect on U-blox F9 for DOY 140, 2019 for a period of 24 hours.

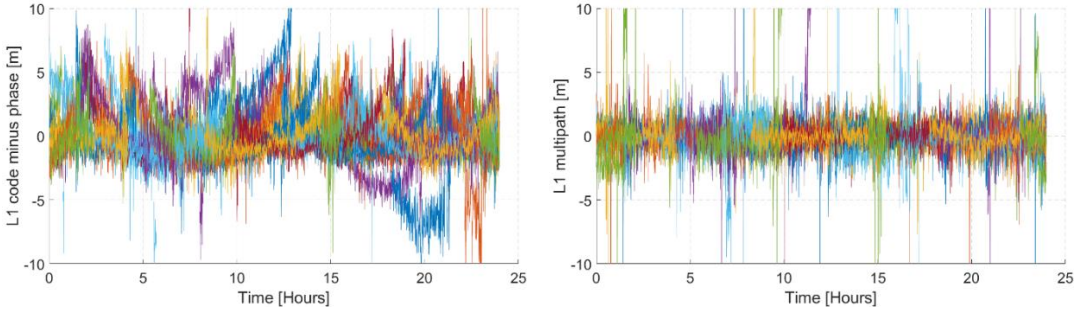

(a) SwiftNav Piksi measurement noise (b) SwiftNav Piksi multipath

Figure 6.6: (a) Measurement noise level and (b) multipath effect on SwiftNav Piksi for DOY 140, 2019 for a period of 24 hours.

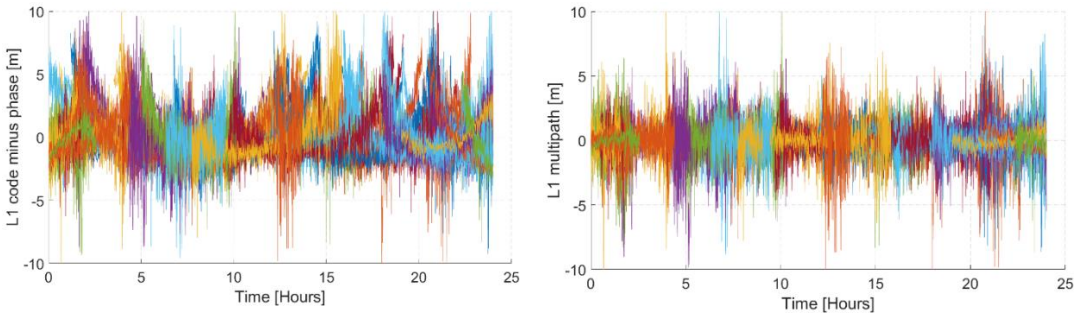

(a) Unicorecomm Nebula II measurement noise

(b) Unicorecomm Nebula II multipath

Figure 6.7: (a) Measurement noise level and (b) multipath effect on Unicorecomm Nebula for DOY 140, 2019 for a period of 24 hours.

It is well known that the measurement noise level as well as multipath is minimal ranging from 1 to 2 m, considering a geodetic-grade receiver and antenna hardware (Kim et al. 2014; Xie et al. 2017). The signal noise and multipath effect results presented above for all the receiver chipsets averaged 4 and 3 m, respectively. Though relatively higher than geodetic-grade hardware equipment, it was interesting to notice how comparable the signal noise and multipath are to their geodetic counterparts. The U-blox F9 showed the least susceptibility to noise while the SwiftNav Piksi experienced the highest levels.

6.3.1 Static multi-GNSS PPP analysis

Figure 6.8 and Figure 6.9 show 24-hour horizontal and 3D positioning results, respectively, for U-blox F9, SwiftNav Piksi, Unicorecomm Nebula II and Topcon geodetic-grade receiver. Results shown are for DOY 140, 2019. The focus of the static analyses centred on the steadiness of solution convergence, initialization and residual analyses. PPP convergence for these results is defined as the time taken for the solution to reach a 10 cm error threshold.

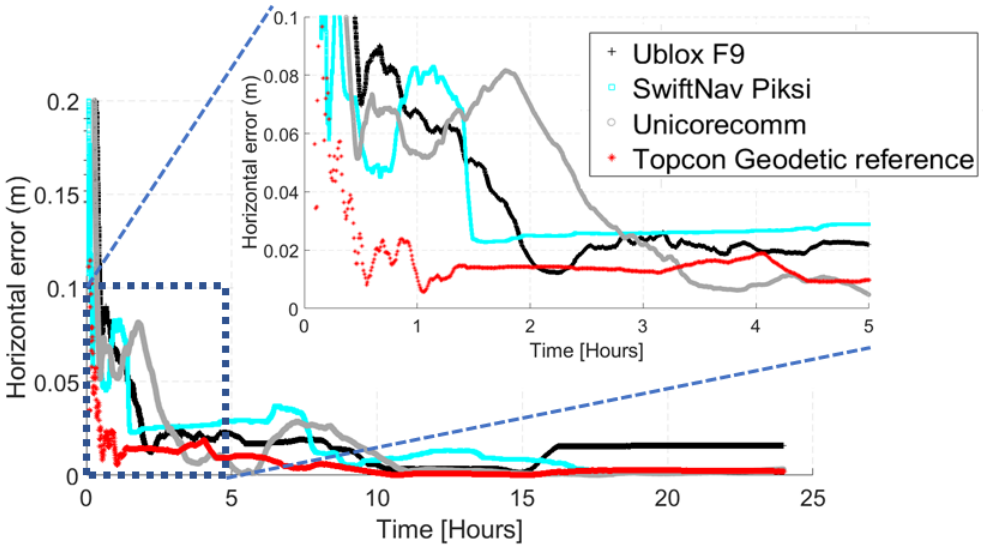

Figure 6.8: Horizontal positioning error for U-blox F9 (black cross), SwiftNav Piksi (turquoise square), Unicorecomm Nebula II (grey circle) and Topcon geodetic-grade receiver (red star). Results are shown for DOY 140, 2019 for a period of 24 hours.

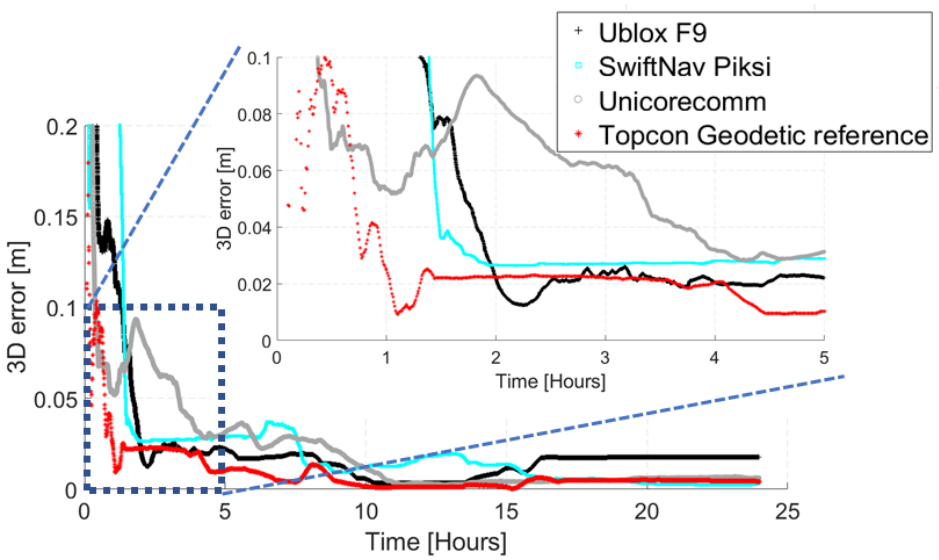

Figure 6.9: 3D positioning error for U-blox F9 (black cross), SwiftNav Piksi (turquoise square), Unicorecomm Nebula II (grey circle) and Topcon geodetic-grade receiver (red star). Results are shown for DOY 140, 2019 for a period of 24 hours.

As shown in Figure 6.8 and Figure 6.9, the Topcon geodetic receiver achieved the best performance due to obvious reasons of geodetic-grade hardware. Considering both horizontal and 3D positioning results, the Topcon reached convergence in 9 and 10 minutes, respectively. This relatively fast convergence from the Topcon reference was closely followed up by SwiftNav Piksi with 18 minutes for the horizontal positioning results. However, it only obtained a steady 3D convergence after 1.4 hours signifying the impact of residual multipath and noise in the up component on the positioning results. Unicorecomm Nebula II and U-blox F9 achieved a horizontal convergence of 22 and 27 minutes, respectively. The 3D convergence for both of these

receivers however showed better performance as compared to SwiftNav Piksi. Unicorecomm Nebula II solution converged in 22 minutes while U-blox F9 steadied at 1.3 hours. It is noteworthy to point out that, both the Unicorecomm and U-blox F9 had better solution steadiness for the entire 24-period in contrast to the SwiftNav Piksi.

Shown in Figure 6.10(a) and (b) are the horizontal scatter plots of the receiver chipsets. The presented PPP solutions are for 24 hours of data processing. The blue ring in the figures represent the 95th percentile. The north and east deviations observed were due to solution initializations before they converged given the dominance of the carrier-phases. As the convergence became steady, most of the solution points were within the 95th percentile.

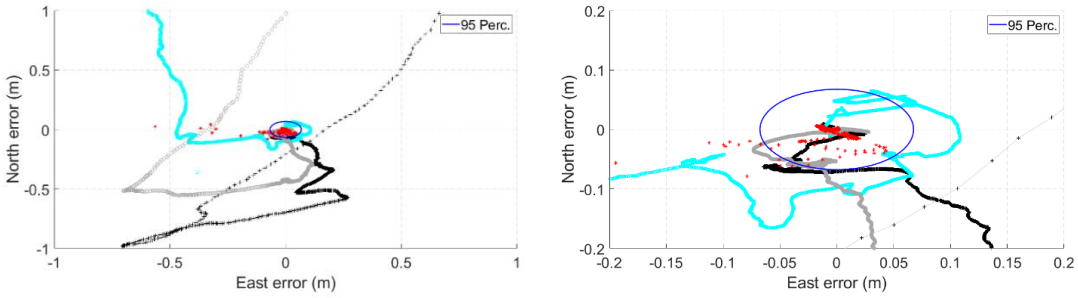

(a) Scatter results at 1 m error threshold

(b) Scatter results at 20 cm error threshold

Figure 6.10: Horizontal scatter for U-blox F9 (black cross), SwiftNav Piksi (turquoise square), Unicorecomm Nebula II (grey circle) and Topcon geodetic-grade receiver (red star). Results are shown for DOY 140, 2019 for a period of 24 hours. Blue ring represents 95th percentile.

Table 6.3 shows the statistical results for all the low-cost receivers as well as Topcon geodetic reference receiver over the 24-hour period for DOY 140, 2019. The statistics presented are for the north, east, up, 2D and 3D components. It was interesting to observe the equivalence in the comparison of the accuracies of the receivers to the millimetre level. Though the Topcon receiver achieved the best accuracy standard due to its geodetic-grade hardware components, the relatively low-cost receivers tallied closely irrespective of the hardware limitations and low-cost characterization.

Receiver	N (mm)	E (mm)	U (mm)	2D (mm)	3D (mm)
U-blox F9	12	7	6	14	15
SwiftNav Piksi	4	13	7	14	15
Unicorecomm Nebula II	10	2	10	10	14
Topcon	4	2	4	4	5

Table 6.3. N, E, U, 2D and 3D component statistics for U-blox F9, Swiftnav Piksi, Unicorecomm Nebula II and Topcon receivers. Statistics are shown for DOY 140, 2019 for a period of 24 hours after steady convergence.

Given that the position domain does not entirely depict the performance of the receivers, a residual analysis was necessary to add another layer of depth to the assessment. Presented in Figure 6.11, Figure 6.12, Figure 6.13 and Figure 6.14 are the pseudorange and carrier-phase residual time series for Topcon, U-blox F9, SwiftNav Piksi and Unicorecomm Nebula II receivers, respectively.

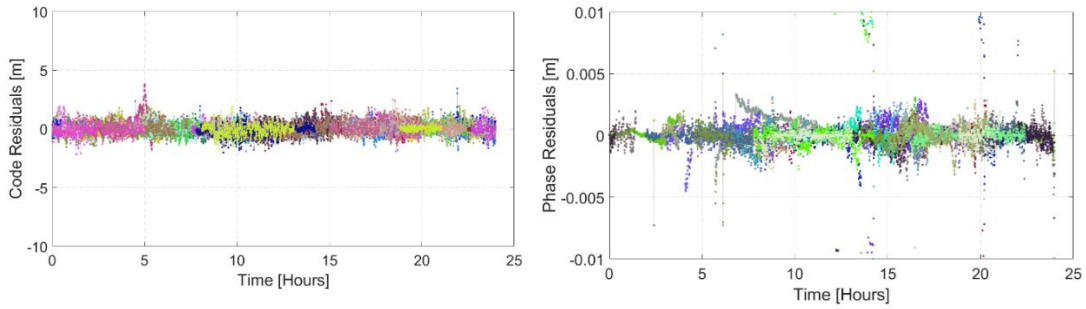

(a) Topcon pseudorange residuals (b) Topcon carrier-phase residuals

Figure 6.11: (a) Pseudorange and (b) carrier-phase residual time series for Topcon geodetic-grade receiver for DOY 140, 2019 for a period of 24 hours. Different satellites are represented by different colours.

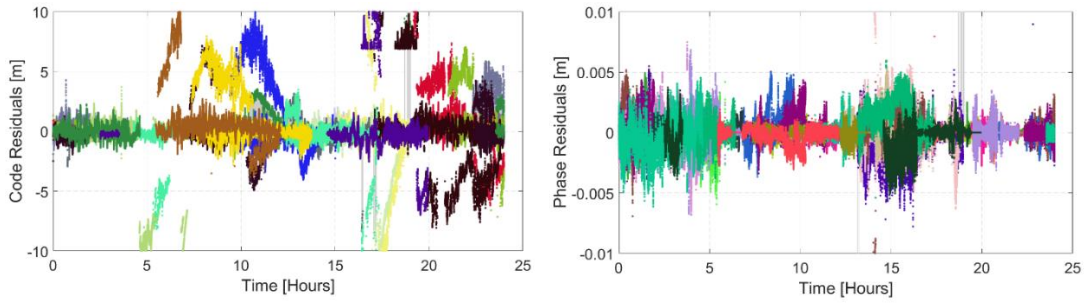

(a) U-blox F9 pseudorange residuals (b) U-blox F9 carrier-phase residuals

Figure 6.12: (a) Pseudorange and (b) carrier-phase residual time series for U-blox F9 receiver for DOY 140, 2019 for a period of 24 hours. Different satellites are represented by different colours.

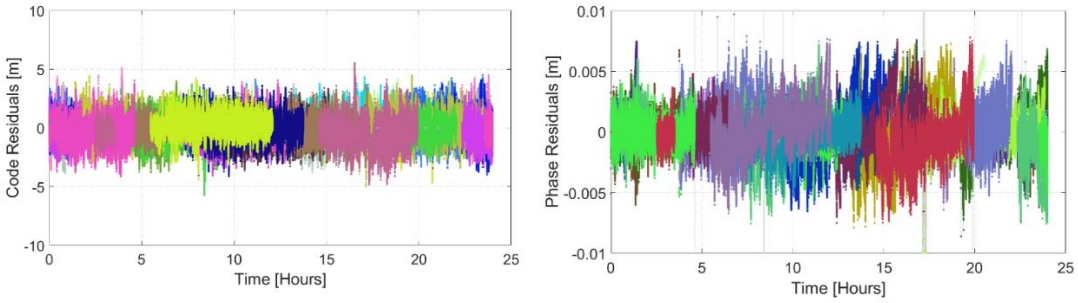

(a) SwiftNav Piksi pseudorange residuals

(b) SwiftNav Piksi carrier-phase residuals

Figure 6.13: (a) Pseudorange and (b) carrier-phase residual time series for SwiftNav Piksi receiver for DOY 140, 2019 for a period of 24 hours. Different satellites are represented by different colours.

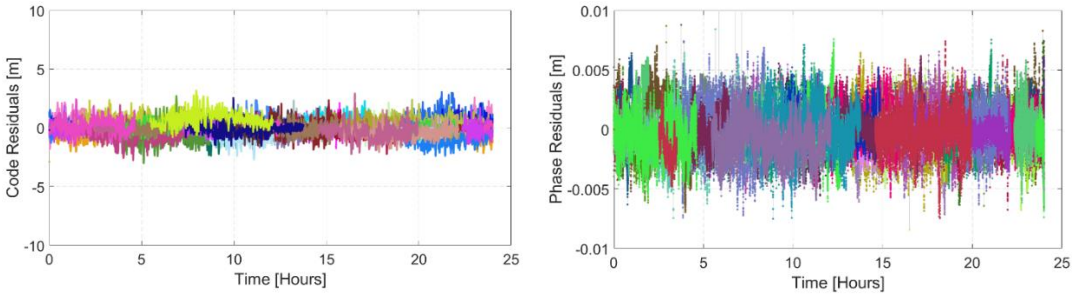

(a) Unicorecomm Nebula II pseudorange residuals

(b) UnicorecommNebula II carrier-phase residuals

Figure 6.14: (a) Pseudorange and (b) carrier-phase residual time series for Unicorecomm Nebula II receiver for DOY 140, 2019 for a period of 24 hours. Different satellites are represented by different colours.

As portrayed in Table 6.4, the carrier-phase residual rms was fairly consistent at the millimetre level among all the receivers. However, the rms for the U-blox F9 pseudorange residuals reached up to the metre level while the other receivers ranged between 20 and 50 cm. Being the cheapest among them, the 1 m level residuals were potentially due to more predominant hardware biases originating from the low-cost hardware receiver components.

Receiver	Pseudorange residual rms (m)	Carrier-phase residual rms (mm)
U-blox F9	1.02	2
SwiftNav Piksi	0.42	1
Unicorecomm Nebula II	0.27	2
Topcon	0.26	3

Table 6.4. Pseudorange and carrier-phase residual rms statistics for U-blox F9, Swiftnav Piksi, Unicorecomm Nebula II and Topcon. Statistics are shown for DOY 140, 2019 for a period of 24 hours.

6.3.2 Kinematic multi-GNSS PPP analysis

To further assess the performance of the U-blox F9, Swiftnav Piksi and Unicorecomm receiver chipsets, a kinematic test was conducted on DOY, 2019 lasting approximately 50 minutes. The setup of the receivers for the experiment was similar to the static experiment, as depicted in Figure 6.1(a). The GNSS data were collected on the streets of Toronto, near York University, Canada. Similar to the static test, GBM final products were used and the processing strategy was equivalent to the one shown

in Table 5.3. However, to represent the dynamics of a moving car, the process noise used was 20 m/s. Shown in Figure 6.15 are the trajectory of the receivers around the York University campus.

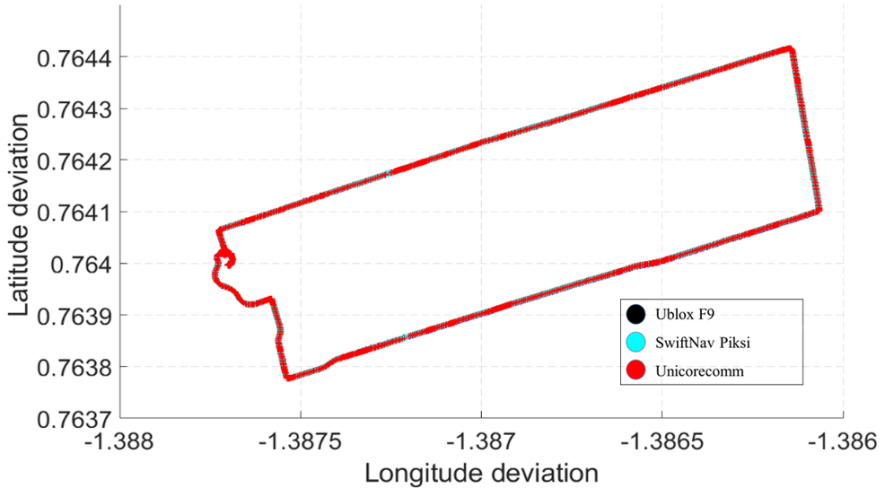

Figure 6.15: Horizontal trajectory of car using U-blox F9, SwiftNav Piksi and Unicorecomm Nebula II receivers for DOY 141, 2019 for a period of 50 minutes.

The car went under several dense tree canopies, resulting in significant drops in the number of GNSS satellites. Aside moving in a straight lane in most cases of the car drive, there were unique situations that tested the solution quality and accuracy of the receivers. Shown in Figure 6.16 are sample instances of situations that helped in the assessment of the receivers. While going under an overpass, there was a momentary drop of signals which affected the solutions. As seen in Figure 6.16 (a), before the entry into the shadow of the overpass, all the trajectories of the receivers stayed on track. However, due to loss of satellites, the exit trajectories were affected

as the solutions re-initialized before converging back to the designated trajectory after a few seconds.

(a) Under an overpass

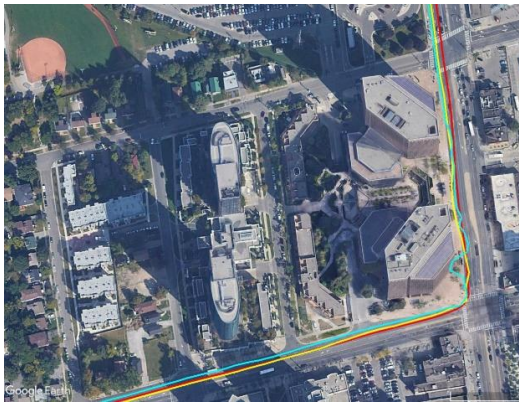

(b) Around a bend with tall buidings

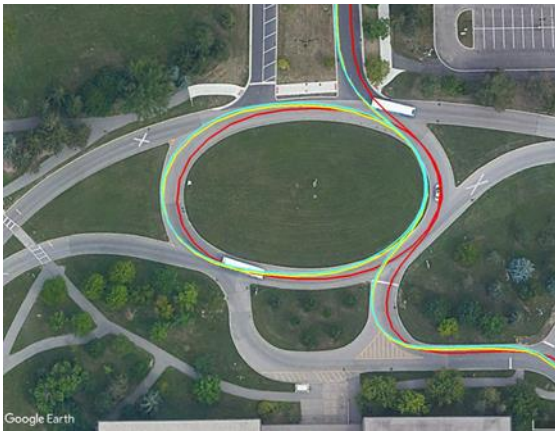

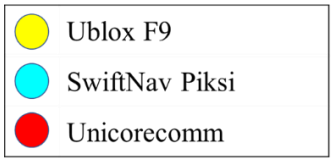

(c) Through a roundabout

Figure 6.16: Sample instances of trajectory of car in the assessment of U-blox F9, SwiftNav Piksi and Unicorecomm Nebula II receivers for DOY 141, 2019 for a period of 50 minutes.

Figure 6.17 shows the rises and drops of the number of satellites as the car traversed along the designated trajectory. A similar scenario was repeated when there was significant multipath of the GNSS signals around a bend with very tall storey buildings, as shown in Figure 6.16 (b). It is interesting to observed that U-blox F9 and SwiftNav Piksi solutions are much more susceptible to the number of satellites. The Unicorecomm solution performed much better around the bends in comparison to the rest of the receivers.

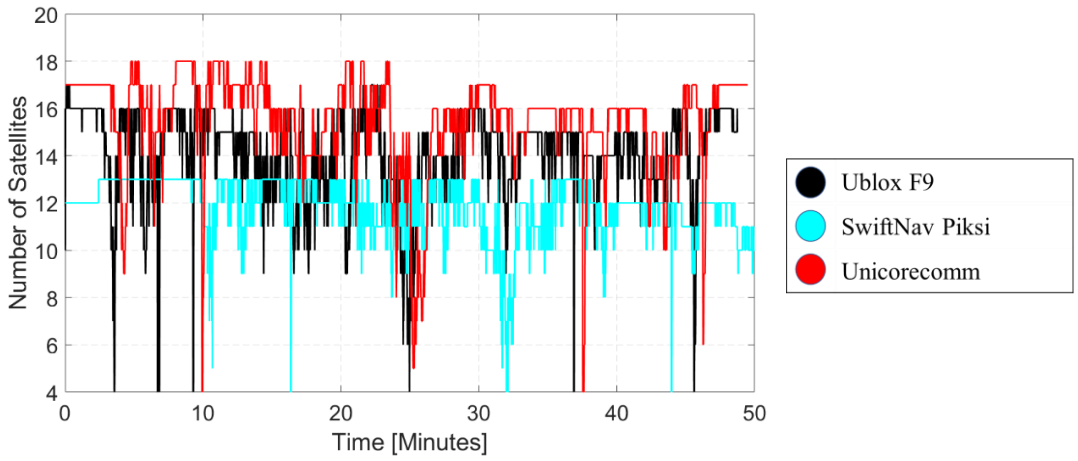

Figure 6.17: Number of satellites during trajectory of car in the assessment of U-blox F9, SwiftNav Piksi and Unicorecomm Nebula II receivers for DOY 141, 2019 for a period of 50 minutes.

Lastly, the performance differences of the receivers became even more obvious through a roundabout as shown in Figure 6.16 (c). Similar to the prior right turn

scenario, the performance of the Unicorecomm solution was interestingly better as it closely followed the actual track of the car. On the much straighter route scenarios, all the receivers performed equally in following the actual trajectory of the car. Shown in Figure 6.18, Figure 6.19 and Figure 6.20 are the kinematic pseudorange and carrier-phase residuals of the receiver chipsets investigated.

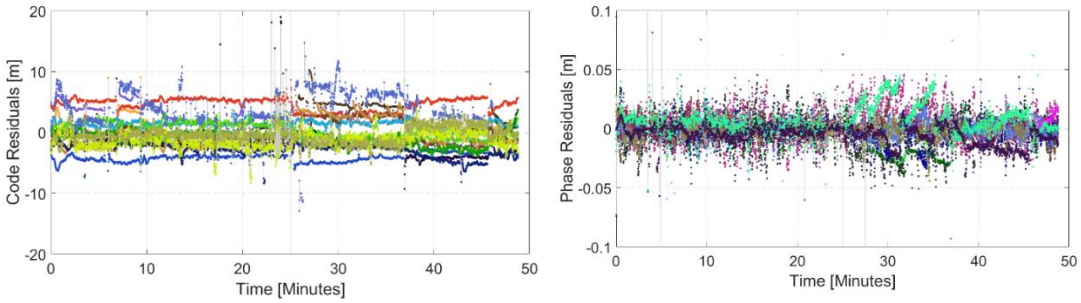

(a) U-blox F9 pseudorange residuals (b) U-blox F9 carrier-phase residuals

Figure 6.18: Kinematic (a) Pseudorange and (b) carrier-phase residual time series for U-blox F9 receiver for DOY 141, 2019 for a period of 24 hours. Different satellites are represented by different colours.

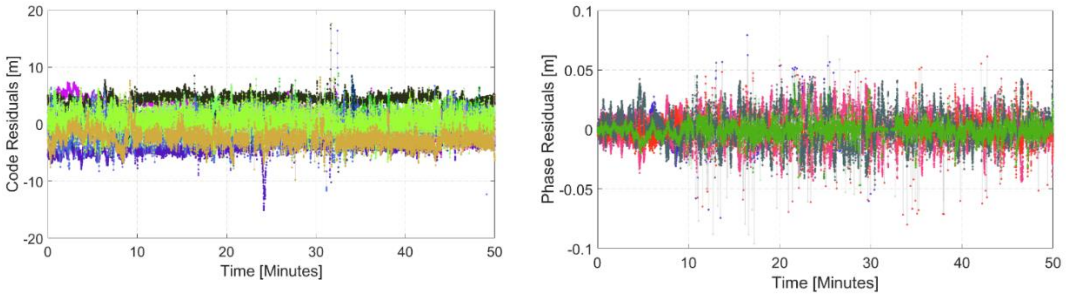

(a) SwiftNav Piksi pseudorange residuals (b) SwiftNav carrier-phase residuals

Figure 6.19: Kinematic (a) Pseudorange and (b) carrier-phase residual time series for SwiftNav Piksi receiver for DOY 141, 2019 for a period of 24 hours. Different satellites are represented by different colours.

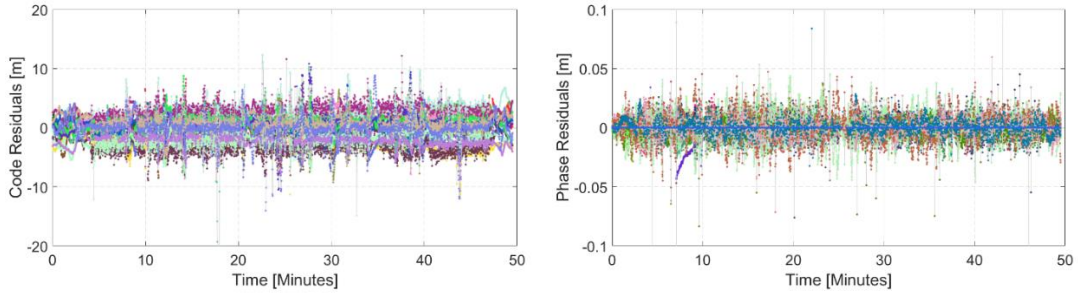

(a) Unicorecomm pseudorange residuals

(b) Unicorecomm carrier-phase residuals

Figure 6.20: Kinematic (a) Pseudorange and (b) carrier-phase residual time series for Unicorecomm Nebula II receiver for DOY 141, 2019 for a period of 24 hours. Different satellites are represented by different colours.

The residuals from all the receivers were well-behaved and consistent with what was expected, given the dynamics of the car and process noise employed in the data processing. As shown in Table 6.5, the pseudorange residuals for all the receivers were consistent at the 1 m level. However, the carrier-phase residuals for the U-blox F9 reached up to the centimetre level while the SwiftNav Piksi and Unicorecomm Nebula II were at the millimetre level.

Receiver	Pseudorange residual rms (m)	Carrier-phase residual rms (mm)
U-blox F9	1.30	17
SwiftNav Piksi	1.32	7
Unicorecomm Nebula II	1.47	6

Table 6.5. Kinematic pseudorange and carrier-phase residual rms statistics for U-blox F9, Swiftnav Piksi, Unicorecomm Nebula II and Topcon. Statistics are shown for DOY 141, 2019 for a period of 24 hours.

6.4 Summary

The results presented in this research contribution are very promising for the use of PPP in next-generation GNSS sensors for vehicle, Internet of things (IoT), etc. applications. Results obtained through this research contribution showed the equivalence in positioning accuracy between the sensors and the reference geodetic receivers. In summary this work highlighted some objectives that were intended to be answered:

(1) What is the performance of current low-cost geodetic-grade receiver sensors?

The equivalence of solutions between the current emerging low-cost sensors and geodetic-grade receivers was demonstrated. Results indicated that millimetre level difference in static multi-GNSS PPP solution accuracy. The major differences in the sensors was highlighted in the PPP initialization where depending on the sensor and its hardware components, centimetre level differences were observed.

Both static and kinematic scenarios investigated showed coherence among the solutions as well as consistency in the geodetic-grade solution accuracy obtained.

(2) Given the quality of observations of relative low-cost sensors in contrast to geodetic grade receivers, what adaptive measurement weighting can be used to enhance the solution performance?

The measurement weighting scheme adapted in this work corresponded to the quality of the hardware components of the receiver sensors. It was highlighted that appropriate a priori standard deviations for both pseudorange and carrier-phase measurements have to be carefully accounted for to prevent over- and under-weighting the measurement. As a guide, an example of the weighting scheme was shown as was implemented for the results shown in this contribution.

(3) Through multi-GNSS PPP processing, what performance metrics can the end user adopt as a guide when it comes to low-cost receiver applications?

The performance assessment used throughout this work was a standard approach. The quality of the measurements was thoroughly examined using the SNR of the raw measurements. The position domain was also assessed considering the PPP solution steady convergence and initialization to assess the accuracy and quality of the position estimates. The residual effect of both the measurements and satellite characteristics were analyzed to paint a full picture of the PPP solutions.

The emergence of geodetic-grade low-cost receiver chipsets promotes research which will only accelerate in the coming years. Future work would involve the resolution of float ambiguities on all available GNSS signals as well as imposing a priori constraints to improve the solution quality.

CHAPTER 7 CONCLUSIONS AND RECOMMENDATIONS FOR FUTURE RESEARCH

From geodetic grade hardware to low-cost GNSS equipment, the work in enhancing accuracy is intended to be used for improving the solution performance for dual-frequency, low-cost chips and smartphone positioning. The release of state of the art dual-frequency, low-cost chips from GNSS manufacturing companies opens the doorway to various applications. By employing geodetic-grade accuracy standards to low-cost hardware, it has been shown in the preceding chapters that PPP solutions obtained with low-cost equipment have significantly improved.

7.1 Conclusions

The focus of this research is to improve PPP solution quality by significantly reducing the initial convergence time of PPP as well as increase the integrity of the user solution. The augmentations developed for improving the user position accuracy is further employed to smartphone measurements and low-cost GNSS chips. Unique and significant contributions were made to enhance the accuracy of the user positions. The objectives addressing these contributions include: 1) Improving multi-GNSS PPP convergence through the use of dual- and triple-frequency measurements; 2) Using global and regional atmospheric corrections to improve PPP solution accuracy; 3)

Improving user solution accuracy using measurements from recently released smartphone chips; 4) Applying PPP augmentations to newly released state-of-the-art low-cost chips intended for the automotive market.

7.1.1 Multi-GNSS PPP initialization

It is concluded that the addition of the third frequency does impact PPP float solution initialization significantly. Improvements of 23% and 27% were observed for the first 5 and 10-minute period, respectively, where the issue of quick convergence is critical. Though results were shown for float solutions, it is anticipated that by resolving ambiguities, the level of improvement should significantly increase. Emphasis was placed on the GPS L5 bias in terms of how its application could potentially aid in PPP float solutions. The new proposed CNES SINEX bias format was applied and results show 22% and 18% improvement in the first 5 and 10 minutes, respectively. Given that the ambiguities were not fixed, this level of improvement was expected. It was also shown that by applying different weighting schemes, the triple-frequency float solutions are impacted in the first few minutes. For constellational-based weighting, down-weighting GLONASS but maintaining equal weights for GPS, Galileo and BeiDou showed the best results. Relatively good results were observed when Galileo and BeiDou were down weighted. Observable weighting showed GLONASS pseudorange being down weighted with equal weights for Galileo, GPS

and BeiDou. The results were better than further down-weighting GLONASS and Beidou observables.

7.1.2 Improving multi-GNSS PPP convergence through atmospheric constraints

It is concluded that the choice of using predicted or post-processed products impacts the level of improvement in PPP solution initialization and convergence. Centimetre-to-millimetre level of variations were observed to exist among the different IONEX products when used to constrain dual-and triple-frequency PPP solutions. Using a global network of stations in different latitudinal regions through novel analysis, it was observed that key differences existed in terms of convergence time improvements and percentages of stations reaching a 20 cm horizontal threshold depending on the processing mode. It was also observed that the slant VTEC from GIM and its corresponding rms values affect PPP convergence since they are not uniform with regards to latitudinal changes. It was significant to observe the effect that ionospheric latitudinal changes had on multi-PPP constrained solutions. Proximity analysis was also conducted to ascertain how far or close a nearby station had to be for its slant ionospheric delay to be useful in constraining PPP solutions when considering a tight convergence threshold of 10 cm horizontal error. For a convergence time of 12 minutes or less, it was observed that stations had to be less than 100 km apart. The significance of the analysis anchors on how sparse and dense network of

stations, used to generate ionospheric products, affect the PPP user in terms of solution convergence.

Using GIM and tropospheric zenith delay corrections, a progression of improvements has been shown. Position accuracy and solution convergence were the key criteria assessed. By resolving ambiguities while constraining atmospheric parameters, it was observed that the multi-GNSS PPP solutions converged to a decimetre-level in less than 2 minutes for the horizontal components. Comparing the atmospheric constrained multi-GNSS PPP-AR to the unconstrained solution, a significant level of improvement was noticed which addressed the importance and efficacy of the constraints applied. The atmospheric constrained PPP solutions for triple-frequency PPP solutions showed more than 60% improvement in the position accuracy as compared to dual-frequency solutions. Using a strict convergence threshold of 10 minutes for the PPP solution to be steady under a horizontal error of 10 cm, the significance of atmospheric constraints in PPP-AR was shown. The realism of the GIM and estimated slant delays was also investigated which informs on the need to be cautious of either under or over constraining the PPP solutions. In summary, to address the original questions posed at the introduction of this contribution, conclusions are as follows:

(1) ***What is the magnitude of improvements observed from the usage of traditional dual-frequency measurements to triple-frequency PPP processing with atmospheric constraints?***

Results presented showed a significant level of improvement of more than 60% from atmospheric constrained dual- to triple-frequency multi-GNSS PPP in terms of the reduction in convergence time.

(2) ***What are the inherent challenges when constraining PPP solutions with atmospheric corrections either functionally or stochastically?***

It was shown that caution needs to be taken when considering using GIM estimates and their uncertainties to constrain. To avoid under or over constraining, there is the need for an adaptive method in the application of the constraints.

(3) ***What is the significance of PPP-AR in multi-GNSS PPP atmospheric constrained solution?***

PPP-AR plays a vital role and enables an improved atmospheric constrained solution. Results presented in this chapter with GPS-AR showed the best improvement at the 95^{th} percentile.

(4) ***Finally, what are the key challenges left in obtaining near-instantaneous PPP convergence akin to RTK data processing?***

With typical RTK convergence of 10 minutes, results presented showed how close we are to near-instantaneous convergence. With accurate and improved atmospheric products, as well as orbits, clocks and bias estimation, PPP solution accuracy is bound to significantly improve, especially in the first few minutes.

7.1.3 Improving smartphone positioning accuracy with multi-GNSS PPP

The positioning results from the dual-frequency chipsets showed improvements in accuracy and reductions in convergence time over a 6-hour period and especially over the first few minutes. The smartphones' performance was compared with that of a geodetic and relative low-cost receiver. Experiments were conducted in multiple different scenarios with the aim of testing the smartphones under different multipath profiles. For static PPP results, a setup mimicking human normal smartphone usage was used to simulate a user holding the phone for 6 hours. Kinematic solutions were also obtained by using a car on a selected route. It was observed that the smartphones raw measurements showed higher multipath profiles and lower C/N_0 compared to the geodetic and low-cost receiver. Given the quality of the raw measurements, adaptive measurement weighting and software augmentation was made while the convergence threshold in our York PPP engine was set to 10 and 20 cm for dual-and single-frequency modes, respectively. An elevation and C/N_0 threshold of 10° and 15 dB-Hz were also used, respectively, as checks to improve data quality. Single-frequency PPP processing with smartphones showed an average

horizontal root mean square (rms) error of 60 cm. However, with dual-frequency multi-GNSS PPP processing, the horizontal rms error was an average of 40 cm. The good news of having duty cycle turned off for Pixel 3 and Xiaomi phones provided consistent measurements for kinematic solutions. For both static and kinematic scenarios, decimetre-level horizontal error was achieved. The raw measurement analysis showed that GPS and Galileo satellites had higher C/N_0 and lower multipath effects as compared to BeiDou.

In summary, the research addressed and answered the following research objective questions:

(1) ***What is the typical performance when using the raw measurements from these smartphones in multi-GNSS PPP processing either in static or kinematic scenarios?***

In static GNSS PPP processing with a smartphone equipped with a dual-frequency chipset, it is possible to obtain decimetre-level accuracy in 38 minutes, comparable to geodetic-grade receiver and antenna. A kinematic scenario showed an accuracy of a few metres.

(2) ***Given the limitation that the hardware components of the smartphones present, what PPP processing changes can be implemented to make use of the raw measurements from smartphones?***

As shown in this research contribution, the signal noise level on the raw measurements from smartphones can be approximately 90% more than that of a geodetic-grade equipment. The C/N_0 of the satellites tracked can be as low as 10 dB-Hz. It is thus imperative to implement necessary measurement weighting schemes to accommodate these measurements in PPP processing.

(3) ***What is the best performance that can be achieved with multi-GNSS PPP given the usage of the smartphones by the user?***

Through an experimental setup purported to mimic human usage of smartphones in a static scenario, the GNSS PPP solution converged in 38 minutes, assuming a horizontal error threshold of 10 cm. The 10 cm error threshold represents a strict tolerance for very precise applications. The convergence is expected significantly improve if the threshold is increased further depending on the user application.

7.1.4 Performance assessment of current relatively low-cost receivers

The results shown in this research contribution were promising for the use of PPP in next-generation GNSS sensors for smartphone, vehicle, Internet of things (IoT), etc. applications. The equivalence in positioning accuracy between the sensors and the reference geodetic receivers was addressed. In summary this work highlighted some objectives that were intended to be answered:

(1) What is the performance of current low-cost geodetic-grade receiver sensors?

The equivalence of solutions between the current emerging low-cost sensors and geodetic-grade receivers was demonstrated. Results indicated that millimetre-level difference in multi-GNSS PPP solution accuracy. The major differences in the sensors was highlighted in the PPP initialization where depending on the sensor and its hardware components, centimetre level differences were observed. Both static and kinematic scenarios investigated showed coherence among the solutions as well as consistency in the geodetic-grade solution accuracy obtained.

(2) Given the quality of observations of relative low-cost sensors in contrast to geodetic grade receivers, what adaptive measurement weighting can be used to enhance the solution performance?

The measurement weighting scheme adapted in this work corresponded to the quality of the hardware components of the receiver sensors. It was highlighted that appropriate a priori standard deviations for both pseudorange and carrier-phase measurements have to be carefully accounted for to prevent over- and under-weighting the measurement. As a guide, an example of the weighting scheme was shown as was implemented for the results shown in this contribution.

(3) Through multi-GNSS PPP processing, what performance metrics can the end user adopt as a guide when it comes to low-cost receiver applications?

The performance assessment used throughout this work was a standard approach. The quality of the measurements was thoroughly examined using the SNR of the raw measurements. The position domain was also assessed considering the PPP solution steady convergence and initialization to assess the accuracy and quality of the position estimates. The residual effect of both the measurements and satellite characteristics were analyzed to paint a full picture of the PPP solutions.

The emergence of geodetic-grade low-cost receiver chipsets promotes researches which will only accelerate in the coming years. Future work would involve the resolution of float ambiguities on all available GNSS signals as well as imposing a priori constraints to improve the solution quality.

7.2 Recommendations for future research

Development of new GNSSs over the years has brought new features and possibilities to the consumer market. With the launch of new GNSS missions, densely spread spectra over 1146-1616 MHz and miniaturization of GNSS chipset have played a vital role in revolutionizing the technology of GNSS receivers. With the development of new features and application demands, there is always an urge from the consumer market to provide high-accuracy positioning solution at a lower cost.

The advent of dual-frequency chipsets in smartphones as well as emergence of geodetic-grade low-cost receiver chipsets enables the capability of improving

accuracy in various potential user applications such as location-based services, augmented reality apps, gaming, etc.

7.2.1 GNSS PPP-AR with low-cost GNSS receivers and antennas

Conventionally, single-frequency positioning is associated with low-cost GNSS receivers. It is anticipated that the integration of low-cost GNSS chips with upcoming new low bandwidth real-time products will enhance position accuracy especially to the automotive market. Novel research areas in multi-GNSS PPP are created with the advancement in low-cost hardware technology and the modernization of GNSS signals. The miniaturization, low prices and hardware structure of low-cost receivers and antennas are expected to be limiting factors that informs the increase of multipath and signal noise in the user position. Investigating various mitigation techniques in handling multipath and signal noise on low-cost receiver measurements would aid in enhancing the solution quality at the user end.

From the theoretical standpoint, there is the impetus to maximize performance: mm-level static positioning over many hours; and few cm-level kinematic positioning in a few minutes, by augmenting PPP in any ways necessary. There is the academic exercise to maximize performance without the need for local or regional reference stations – apparent single-receiver positioning, or truly wide area augmentation. In terms of engineering problems, decimetre-level positioning with ultra-low-cost

hardware is possible with low-cost hardware. And from the practical or commercial aspect, the great interest is for the institution of evolved PPP methods for application which can efficiently and effectively make use of the technology.

In terms of service providers, be it regional or global, commercial or public, there is momentum to provide enhanced correction products that are blurring the lines across the service spectrum from constellation-owner tracking to regional, terrestrial augmentation. A public constellation-owner, though its constellation tracking network, can provide PPP corrections and services. A global commercial provider with or without regional augmentation can provide similar services. The key is providing multi-GNSS state space corrections for satellite orbits, satellite clocks, satellite equipment delays (fractional phase biases), zenith ionospheric delay, and zenith tropospheric delay at the temporal and spatial resolution necessary for the desired positioning performance at reasonable cost, i.e., subscription fees that that particular markets can bear.

Given these correction products, PPP users do have a greater ability to access a wide array of positioning performance levels for various new applications. Be it few dm-level positioning on mobile devices to few cm-level positioning for autonomous or semi-autonomous land, sea and air vehicles. PPP can be used for integrity monitoring and safety-of-life applications where low-cost is a necessity and relatively precise positioning for integrity purposes is required. For safety critical and high-

precision applications, such as vehicle automation, PPP can be used alongside RTK for robustness and independence with low-cost hardware.

7.2.2 Extra widelaning and instantaneous PPP-AR

Currently GPS, Galileo and BeiDou satellites transmit triple-frequency signals. In the near future, it is expected that all available GNSSs will be equipped with the capability of transmitting multi-frequency signals. Various research contributions have investigated the possibility of faster or instantaneous ambiguity resolution using simulated or real-time measurements. Given that more linear combinations can be formed with the addition of these new signals, optimal combinations intended for fast ambiguity resolution (Vollath et al. 1999; Feng 2008) and enhanced cycle slip detection (Zhang and Li 2016). Though various methods such as Three-Carrier AR (TCAR) and Cascading Integer Resolution (CIR), have been proposed in regards to wavelength expansion (Hatch 2006; Cocard et al. 2008; Henkel and Günther 2010), there is still more work to be done given the advancement and modernization of GNSS signals. With regards to triple-frequency AR, the extra widelane promises the reliability of instantaneous ambiguity fixes though the narrowlane ambiguities can be challenging. Triple-frequency PPP-AR with extra widelaning has the added advantages of providing PPP solution quality control, improved measurement redundancy and reliability of PPP-AR solutions.

7.2.3 Sensor integration

The recent emergence of low-cost sensors has prompted research in integrated navigation solution using the PPP technique. Although the GNSS PPP-only position solution has the drawback of initial convergence time, the accuracy that the solution can deliver with integrated sensors make it very attractive to use it in applications like autonomous vehicles, drones, augmented reality, pedestrian navigation, UAVs and other emerging scientific, engineering and consumer applications. These applications demand continuous position accuracy at the metre to centimetre level to satisfy various application requirements. The automotive market, for instance, requires very stringent accuracy in the order of centimetres. The inclusion of low-cost, multi-sensors such as IMUs, barometers, CSAC atomic clocks will aid in obtaining redundancy in measurements to improve position accuracy in the event of the lack of GNSS satellites. It is expected the up component especially would benefit from the coupling of these multiple sensors in a GNSS PPP only solution. Considering pedestrian or UAV applications, the use of IMUs and atomic clocks in a sensor-fused solution can be used as constraints to improve the solution accuracy performance.

7.2.4 Adaptive stochastic modelling

Defining a well-structured stochastic model which accounts for the optimization of estimates in a least-squares solution. Considering that the stochastic model

represents the statistical and variance-covariance characteristics of measurements, much attention has not been drawn to its importance. Given GNSS signal modernization and proliferation, it can be a problem to assume equal variances for these measurements irrespective of GNSS satellites transmitting them. As shown in previous chapters, more work needs to be done on the estimation constraining of the ionospheric term, to make use of a priori ionospheric information and its impacts on both dual- and triple-frequency PPP-AR solution quality. By constraining atmospheric parameters and resolving float ambiguities on all available GNSSs, it is expected that PPP solution accuracy and initialization would improve as evidenced in various researches with dual-frequency measurements. It is also imperative to investigate time correlation errors which are systematic in nature due to noise and multipath effects. With regards to smartphone and low-cost receivers, it is necessary to consider adaptive C/N_0 and elevation weighting for the noisy measurements with aim of enhancing the solution performance.

REFERENCES

Abrahams J (2018) NovAtel® Demonstrates Precise Positioning Using the Teseo APP and Teseo V Automotive GNSS Chipsets from STMicroelectronics. In: GlobeNewswire. https://www.globenewswire.com/news-release/ 2018/03/07/ 1416288/0/en/NovAtel-Demonstrates-Precise-Positioning-Using-the-Teseo-APP-and-Teseo-V-Automotive-GNSS-Chipsets-from-STMicroelectronics. html. Accessed 23 Apr 2018

Aggrey J (2018) Assessment of Global and Regional Ionospheric Corrections in Multi-GNSS PPP. In: Proceedings of the 31st International Technical Meeting of The Satellite Division of the Institute of Navigation (ION GNSS+ 2018). Miami, Florida, pp 3967–3981

Aggrey J, Bisnath S (2017a) Performance Analysis of Atmospheric Constrained Uncombined Multi-GNSS PPP. In: 30th International Technical Meeting of the Satellite Division of the Institute of Navigation (ION GNSS+ 2017). Portland, Oregon, pp 2191–2203

Aggrey J, Bisnath S (2017b) Analysis of Multi-GNSS PPP Initialization using Dual- and Triple-frequency Data. In: Proceedings of the 2017 International Technical Meeting of The Institute of Navigation. Monterey, California, pp 445–458

Aggrey JE (2015) Multi-GNSS precise point positioning software architecture and analysis of GLONASS pseudorange biases. MSc Thesis, York University, Toronto, Canada, pp 22-46.

Al Khairy M (2018) Snapdragon X24: World's first announced 2 Gbps LTE modem. In: Qualcomm: https://www.qualcomm.com/news/onq/2018/02/14/ snapdragon-x24-worlds-first-announced-2-gbps-lte-modem. Accessed 24 Apr 2019.

Alsubaie N, Youssef A, El-Sheimy N (2017) Improving the accuracy of direct geo-referencing of smartphone-based mobile mapping systems using relative orientation and scene geometric constraints. Sensors 17, pp 2237.

Amiri-Simkooei AR, Jazaeri S, Zangeneh-Nejad F, Asgari J (2015) Role of stochastic model on GPS integer ambiguity resolution success rate. GPS Solutions, pp 1–11. doi: 10.1007/s10291-015-0445-5.

Amundson M (2005) Compass Assisted GPS for LBS Applications. Honeywell International Inc., Plymouth, pp 1-4.

Asari, K, Matsuoka S, Amitani H (2016) "QZSS RTK-PPP Application to Autonomous Cars," Proceedings of the 29th International Technical Meeting of the Satellite Division of The Institute of Navigation (ION GNSS+ 2016), Portland, Oregon, September 2016, pp.2136-2142.

Banville S (2014) Improved convergence for GNSS Precise Point Positioning. PhD Dissertation, University of New Brunswick, pp 99-153.

Banville S, Collins P, Zhang W, Langley RB (2014) Global and regional ionospheric corrections for faster PPP convergence. Navigation Volume 61, pp 115–124.

Banville S, Van Diggelen F (2016) Precise positioning using raw GPS measurements from Android smartphones. GPS World Volume 27, pp 43–48.

Beran T, Langley RB, Bisnath SB, Serrano L (2005) High-accuracy point positioning with low-cost GPS receivers: how good can it get. In: ION GNSS. pp 13–16

Bertiger W, Desai SD, Haines B, Harvey N, Moore AW, Owen S, Weiss JP (2010) Single receiver phase ambiguity resolution with GPS data. Journal of Geodesy, Volume 84, pp 327–337. doi: 10.1007/s00190-010-0371-9.

Bisnath S, Aggrey J, Seepersad G, Gill M (2018) Innovation: Examining precise point positioning now and in the future. GPS World, March 2018, https://www.gpsworld.com/innovation-examining-precise-point-positioning-now-and-in-the-future/.

Bisnath S, Collins P (2012) Recent developments in precise point positioning. Geomatica, Volume 66, pp 103–111.

Bisnath S, Gao Y (2009) Current state of precise point positioning and future prospects and limitations. In: Observing our changing earth. Springer, pp 615–623.

Bisnath SB, Langley RB (2001) Pseudorange multipath mitigation by means of multipath monitoring and de-weighting. Proceedings of KIS, 2001, pp 1-9.

Bowyer M, Bertani A, Aitken E, Rawashdeh SA. (2016) "Landmark Based Autonomous Snowplow Navigation," Proceedings of the 29th International Technical Meeting of the Satellite Division of The Institute of Navigation (ION GNSS+ 2016), Portland, Oregon, September 2016, pp. 1502-1511.

Braasch MS, Van Dierendonck A (1999) GPS receiver architectures and measurements. Proceedings of IEEE Volume 87, pp 48–64.

Byun S, Bar-Sever Y (2010) The re-analysis of the IGS tropospheric product, IGS Workshop, Newcastle, 28th June- July 1st 2010, http://acc.igs.org/tropo/tropo-repro_IGSW10.pdf, pp 1-8.

Cabinet Office, Government of Japan (2019a) Centimeter Level Augmentation Service (CLAS). In: Quazi-Zenith Satellite System. https://qzss.go.jp/en/overview/services/sv06_clas.html. Accessed 22 Jul 2019.

Cabinet Office, Government of Japan (2019b) Sub-meter Level Augmentation Service (SLAS). In: Quazi-Zenith Satellite System. https://qzss.go.jp/en/overview/services/sv05_slas.html. Accessed 29 Jul 2019.

Cameron A (2019) Benefits coming from GPS III constellation. In: GPS World. https://www.gpsworld.com/benefits-coming-from-gps-iii-constellation/. Accessed 22 Jul 2019.

Chen, K, Gao, Y (2005), "Real-Time Precise Point Positioning Using Single Frequency Data," Proceedings of the 18th International Technical Meeting of the Satellite Division of The Institute of Navigation (ION GNSS 2005), Long Beach, CA, September 2005, pp. 1514-1523.

Chen R., Hyppä J., Zhang J., Takala J., Kuittinen R., Chen Y., Pei L., Liu Z., Zhu L., Kuusniemi H., Liu J., Qin Y., Leppäkoski H., Wang J. (2009) "Development of a 3D Personal Navigation and LBS System with Demonstration in Shanghai EXPO in 2010," Proceedings of the 22nd International Technical Meeting of the Satellite Division of The Institute of Navigation (ION GNSS 2009), Savannah, GA, September 2009, pp. 2124-2129.

China National Administration of GNSS and Applications (2019) China Launched the 41st BeiDou Satellite and Short Message Capacity Increased by 10 Times. In: China Natl. Adm. GNSS Appl. http://en.chinabeidou.gov.cn/c/1278.html. Accessed 29 Jul 2019

China Satellite Navigation Office (2012) BeiDou navigation satellite system signal in space interface control document open service signal B1I (Version 1.0). China Satellite Navigation Office, pp 1-89.

Cocard M, Bourgon S, Kamali O, Collins P (2008) A systematic investigation of optimal carrier-phase combinations for modernized triple-frequency GPS. J Geod 82:555–564

Cocard M, Bourgon S, Kamali O, Collins P (2008) A systematic investigation of optimal carrier-phase combinations for modernized triple-frequency GPS. Journal of Geodesy, Volume 82, pp 555–564.

Collins JP (1999) Assessment and development of a tropospheric delay model for aircraft users of the global positioning system. MSc Thesis, University of New Brunswick, pp 9-46.

Collins P, Bisnath S (2011) Issues in ambiguity resolution for Precise Point Positioning. In: Proceedings of the 24th International Technical Meeting of the Satellite Division of The Institute of Navigation (ION GNSS 2011). pp 679–687.

Collins P, Lahaye F, Bisnath S (2012) External ionospheric constraints for improved PPP-AR initialisation and a generalised local augmentation concept. In: Proceedings of the 25th International Technical Meeting of the Satellite Division of The Institute of Navigation (ION GNSS 2012). pp 3055–3065.

Collins P, Lahaye F, Heroux P, Bisnath S (2008) Precise point positioning with ambiguity resolution using the decoupled clock model. In: Proceedings of the 21st international technical meeting of the satellite division of the Institute of Navigation (ION GNSS 2008). pp 1315–1322.

Cozzens T (2018) u-blox F9 platform designed for high-precision mass market. In: GPS World. https://www.gpsworld.com/u-blox-f9-platform-designed-for-high-precision-mass-market/. Accessed 24 Apr 2019.

Crews M, Betz J (2019) GPS III: The Next Big Step in GPS Modernization. In: GNSS. https://insidegnss.com/gps-iii-the-next-big-step-in-gps-modernization/. Accessed 22 Jul 2019.

Crosta P, Watterton T (2018) Introducing the Galileo PVT App: from Assisted GNSS to NeQuick model in Android, pp 1-22.

CSNO TARC (2018) System basic information. In: China Satell. Navig. Syst. Manag. Off. Test Assess. Res. Cent. Test Assess. Res. Cent. China Satell. Navig. Off. http://www.csno-tarc.cn/system/basicinfo. Accessed 12 Jun 2018.

Cueto, M., Cezon, A., Pineda, S., Sardon, E. (2007) "Ionospheric Analysis in the Equatorial Region: Impact on GNSS Performances," Proceedings of the 20th International Technical Meeting of the Satellite Division of The Institute of Navigation (ION GNSS 2007), Fort Worth, TX, September 2007, pp. 2324-2336.

Cui Y, Meng X, Chen Q, Gao Y, Xu C, Roberts S, Wang Y (2017) Feasibility analysis of low-cost GNSS receivers for achieving required positioning performance in CAV applications. In: 2017 Forum on Cooperative Positioning and Service (CPGPS）. IEEE, Harbin, China, pp 355–361

Defraigne P, Bruyninx C (2007) On the link between GPS pseudorange noise and day-boundary discontinuities in geodetic time transfer solutions. GPS Solutions Volume 11, pp 239–249. doi: 10.1007/s10291-007-0054-z.

Department of Space (2011) 12th five-year plan of Department of Space: Report of working group (WG-14). Indian Government, New Delhi.

Dickson P (2003). Sputnik: The Shock of the Century., illus., notes, bibl., index. New York: Walker & Company, 2001. pp 364. Isis. 94. 766-767. 10.1086/386485.

Diggelen F van, Khider M (2018) GPS measurement tools. In: Github. https://github.com/google/gps-measurement-tools/tree/master/GNSSLogger. Accessed 27 Apr 2019.

Do T (2018) List of Smartphones Powered by Qualcomm Snapdragon 835 Processor. In: TechWalls. https://www.techwalls.com/qualcomm-snapdragon-835-smartphones/. Accessed 6 Jun 2019.

Edwards B (2018) The Golden Age of PDAs. In: Gold. Age PDAs. https://www.pcmag.com/feature/364985/the-golden-age-of-pdas. Accessed 22 Apr 2018.

EGSA (2018) World's First Dual-Frequency GNSS Smartphone Hits the Market. In: Eur. Glob. Navig. Satell. Syst. Agency. Accessed 22 Mar 2019.

Eissfeller B, Ameres G, Kropp V, Sanroma D (2007) Performance of GPS, GLONASS and Galileo. In: Photogrammetric Week. pp 185–199.

Elsobeiey M (2014) Precise Point Positioning using Triple-Frequency GPS Measurements. Journal of Navigation, pp. 1–13. doi: 10.1017/S0373463314000824.

Elsobeiey, M., El-Rabbany, A. (2009) "Effect of Second-Order Ionospheric Delay on GPS Orbit and Precise Point Positioning," Proceedings of the 22nd International Technical Meeting of the Satellite Division of The Institute of Navigation (ION GNSS 2009), Savannah, GA, September 2009, pp. 2489-2495.

European GNSS Agency (2015) Report on the Performance and Level of Integrity for Safety and Liability Critical Multi-Applications. https:// www.gsa.europa.eu/ sites/ default/files/calls_for_proposals/Annex%202.pdf.

European GNSS Agency (2017) Constellation Information. In: Eur. GNSS Serv. Cent. https://www.gsc-europa.eu/system-status/Constellation-Information. Accessed 6 Mar 2017.

European GNSS Agency (2018) GNSS User Technology report, 2nd edition. European GNSS Agency, Luxembourg, pp 1-92.

European GNSS Supervisory Authority (2017) GNSS market report. European GNSS Agency, Issue 5, 2017, pp 1-100.

European Space Agency (2015) Sixth Galileo satellite reaches corrected orbit. In: Launching Galileo. http:// www.esa.int/ Our_Activities/ Navigation/ The_future_-_Galileo/ Launching_Galileo/ Sixth_Galileo_ satellite_ reaches _corrected_ orbit. Accessed 15 Mar 2015.

European Space Agency (2019) Galileo navigation program: FOC (Full Operational Capability) Galileo navigation program: FOC (Full Operational Capability). In: EoPortal Dir. https:// directory.eoportal.org/ web/eoportal/satellite-missions/content/-/article/galileo. Accessed 22 Jul 2019.

Fairhurst P, Glueckert U, Richter B (2001) The New Leica Viva GNSS Receiver. In: Proceedings of the 23rd International Technical Meeting of The Satellite Division of the Institute of Navigation (ION GNSS 2010). pp 1386–1394.

Federal Space Agency (2015) GLONASS constellation status. In: Inf.-Anal. Cent. https://www.glonass-iac.ru/en/GLONASS/index.php. Accessed 15 Mar 2015.

Feng Y (2008) GNSS three carrier ambiguity resolution using ionosphere-reduced virtual signals. J Geod 82:847–862.

Fernández-Hernández I, Rijmen V, Seco-Granados G, Simon J (2016) A Navigation Message Authentication Proposal for the Galileo Open Service: NMA proposal for Galileo OS. Navigation, Volume 63, pp 85–102. doi: 10.1002/navi.125.

Fernandez-Hernandez I, Vecchione G, Díaz-Pulido F, European Commission (2018) Galileo Authentication: A Programme and Policy Perspective. Bremen, Germany, pp 1-5.

Gayatri A, Reddy PVN, Hazarathaiah A (2016) Handling the Biases for Improved Triple-Frequency Carrier-Phase Ambiguity Resolution PPP Convergence for GNSS, Proceedings of National Conference on Trends in Engineering & Technology - 2K15 (NCTET-2K15), pp 158-165.

Ge M, Douša J, Li X, Ramatschi M (2012) A Novel Real-time Precise Positioning Service System: Global Precise Point Positioning with Regional Augmentation. J Glob Position Syst, Volume 11, pp 2–10. doi: 10.5081/jgps.11.1.2

Gendt G (1998) IGS combination of tropospheric estimates–experience from pilot experiment. In: Proceedings of 1998 IGS Analysis Center Workshop, JM Dow, J. Kouba and T. Springer, Eds. IGS Central Bureau, Jet Propulsion Laboratory, Pasadena, CA. pp 205–216

Geng J (2010) Rapid integer ambiguity resolution in GPS precise point positioning. PhD Dissertation, University of Nottingham, pp 11-51.

Geng J, Bock Y (2013) Triple-frequency GPS precise point positioning with rapid ambiguity resolution. J Geod Volume 87, pp 449–460. doi: 10.1007/s00190-013-0619-2

Geo++ GmbH (2018) Logging of GNSS Raw Data on Android. In: Geo++. http://www.geopp.de/logging-of-gnss-raw-data-on-android/. Accessed 27 Apr 2019

Gill M (2018) GNSS Precise Point Positioning using low-cost GNSS receivers. MSc Thesis, York University, pp 32-91.

Gill M, Bisnath S, Aggrey J, Seepersad G, "Precise Point Positioning (PPP) using Low-Cost and Ultra-Low-Cost GNSS Receivers," Proceedings of the 30th

International Technical Meeting of the Satellite Division of The Institute of Navigation (ION GNSS+ 2017), Portland, Oregon, September 2017, pp. 226-236.

GPS World Staff (2018) Japan's QZSS service now officially available. In: GPS World. https://www. gpsworld. com/ japans- qzss -service- now -officially-available/. Accessed 29 Jul 2019

GPS.gov (2017) Space Segment. In: Curr. Future Satell. Gener. http://www.gps.gov/systems/gps/space/#generations. Accessed 6 Mar 2017

Gurtner W, Estey L (2007) RINEX-The Receiver Independent Exchange Format-Version 3.00. Astron Inst Univ Bern UNAVCO Bolulder Colorado, pp 7-20.

Hackman C, Guerova G, Byram S, Dousa J, Hugentobler U (2015) International GNSS Service (IGS) Troposphere Products and Working Group Activities. In: FIG Working Week, pp 1-14.

Hadas T, Bosy J (2015) IGS RTS precise orbits and clocks verification and quality degradation over time. GPS Solutions Volume 19, pp 93–105. doi: 10.1007/s10291-014-0369-5.

Hatch R (2006) A new three-frequency, geometry-free technique for ambiguity resolution. In: Proceedings of ION GNSS. pp 26–29.

Hein G (2005) Development and Design of Galileo. Proceedings of ION GPS, Cambridge, MA, St Annu Meet pp 4-9.

Hein G (2017) Codeless Code Tracking. In: GNSS. https://insidegnss.com/codeless-code-tracking/. Accessed 22 Jul 2019.

Henkel P, Günther C (2010) Reliable integer ambiguity resolution with multi-frequency code carrier linear combinations. J Glob Position Syst Volume 9, pp 90–103.

Hernández-Pajares M, Juan JM, Sanz J, Aragon-Angel A, Garcia-Rigo A, Salazar D, Escudero M (2011) The ionosphere: effects, GPS modeling and the benefits for space geodetic techniques. J Geod Volume 85, pp 887–907.

Héroux, P., Gao, Y., Kouba, J., Lahaye, F., Mireault, Y., Collins, P., Macleod, K., Tétreault, P., Chen, K. (2004) "Products and Applications for Precise Point Positioning - Moving Towards Real-Time," Proceedings of the 17th

International Technical Meeting of the Satellite Division of The Institute of Navigation (ION GNSS 2004), Long Beach, CA, September 2004, pp. 1832-1843.

Héroux P, Gao Y, Kouba J, Lahaye F, Mireault Y, Collins P, Macleod K, Tétreault P, Chen K (2001) Products and applications for Precise Point Positioning-Moving towards real-time. In: Proceedings of the 17th International Technical Meeting of the Satellite Division of The Institute of Navigation (ION GNSS 2004). pp 1832–1843

Hofmann-Wellenhof B, Lichtenegger H, Wasle E (2007) GNSS–global navigation satellite systems: GPS, GLONASS, Galileo, and more. Springer Science & Business Media, pp 105-160.

Humphreys TE, Murrian M, Diggelen F van, Podshivalov S, Pesyna K (2016) On the feasibility of cm-accurate positioning via a smartphone's antenna and GNSS chip. In: 2016 IEEE/ION Position, Location and Navigation Symposium (PLANS). pp 232–242.

Humphreys T, Pesyna K, Shepard D, Murrian M, Gonzalez C, Novlan T (2016) Precise Positioning for the Mass Market, GNSS Futures IGS Workshop, pp 47.

IGS (2017) BeiDou. In: IGS MGEX. http:// mgex.igs.org/IGS_MGEX_Status_BDS .html. Accessed 6 Mar 2017

Inaba, N., "Quasi-Zenith Satellite System Program Update," Proceedings of the 22nd International Technical Meeting of the Satellite Division of The Institute of Navigation (ION GNSS 2009), Savannah, GA, September 2009, pp. 3411-3436.

Indian Space Research Organization (2017) Indian Regional Navigation Satellite System Signal in Space ICD for standard Positioning services. ISRO Satelite Centre, Banglore, India.

Inside GNSS (2016) u-blox Launches Automotive-Grade Positioning and Connectivity Modules. In: GNSS. https://insidegnss.com/u-blox-launches-automotive-grade-positioning-and-connectivity-modules/. Accessed 6 Jun 2019.

Ishijima Y, Inaba N, Matsumoto A, Terada K, Yonechi H, Ebisutani H, Ukawa S, Okamoto T (2009) Design and development of the first Quasi-Zenith Satellite

attitude and orbit control system. In: 2009 IEEE Aerospace conference. IEEE, Big Sky, MT, USA, pp 1–8.

Jan S-S (2010) Vertical guidance performance analysis of the L1-L5 dual-frequency GPS/WAAS user avionics sensor. Sensors 10:2609–2625.

Jin S, Park JU, Wang JL, Choi BK (2006) Electron Density Profiles Derived From Ground-Based GPS Observations. J Navig 59: 395–401. https: //doi.org/ 10.1017/ S0373463306003821.

Kaplan ED, Hegarty C (2017) Understanding GPS/GNSS: Principles and applications. Artech House, Third Edition, pp 86-273.

Karimi HA (2011) Universal navigation on smartphones, 1st Ed. Springer Science & Business Media, Springer Science & Business Media, pp 7-51.

Katsumoto T, Takaoka K, Takanohashi K, Youssef M (2017) "GNSS System Design and Evaluation for IoT Applications," Proceedings of the 30th International Technical Meeting of the Satellite Division of The Institute of Navigation (ION GNSS+ 2017), Portland, Oregon, September 2017, pp. 3566-3572.

Kazmierski K, Hadas T, Sośnica K (2018) Weighting of Multi-GNSS Observations in Real-Time Precise Point Positioning. Remote Sens 10:84. doi: 10.3390/rs10010084.

Kim M, Seo J, Lee J (2014) A Comprehensive Method for GNSS Data Quality Determination to Improve Ionospheric Data Analysis. Sensors 14:14971–14993. doi: 10.3390/s140814971.

Kirkko-Jaakkola M, Söderholm S, Honkala S, Koivula H, Nyberg S, Kuusniemi H (2015) "Low-Cost Precise Positioning Using a National GNSS Network," Proceedings of the 28th International Technical Meeting of the Satellite Division of The Institute of Navigation (ION GNSS+ 2015), Tampa, Florida, September 2015, pp. 2570-2577.

Klobuchar JA (1987) Ionospheric time-delay algorithm for single-frequency GPS users. IEEE Trans Aerosp Electron Syst pp 325–331.

Klobuchar JA (1996) Ionospheric effects on GPS. Glob Position Syst Theory Appl 1:485–515.

Kouba J, Héroux P (2001) Precise point positioning using IGS orbit and clock products. GPS Solut 5:12–28.

Kubo Y (2018) G-RitZ Logger. In: Google Play. https://play. google.com/ store/apps/ details?id=com.kubolab.gnss.gnssloggerR&hl=en. Accessed 27 Apr 2019

Laurichesse D (2015) Handling the biases for improved triple-frequency PPP convergence. GPS World April, https://www.gpsworld.com/innovation-carrier-phase-ambiguity-resolution/. Accessed: 28 August 2019.

Laurichesse D, Blot A (2016) Fast PPP Convergence Using Multi-Constellation and Triple-Frequency Ambiguity Resolution. In: Proceedings of the 29th International Technical Meeting of The Satellite Division of the Institute of Navigation (ION GNSS+ 2016). pp 2082–2088

Laurichesse D, Mercier F, Berthias J, Broca P, Cerri L (2009) "Integer Ambiguity Resolution on Undifferenced GPS Phase Measurements and Its Application to PPP and Satellite Precise Orbit Determination", *NAVIGATION, Journal of The Institute of Navigation*, Vol. 56, No. 2, Summer 2009, pp. 135-149

Leandro, R. F. (2009). Precise Point Positioning with GPS: A New Approach for Positioning, Atmospheric Studies, and Signal Analysis. Ph.D. dissertation, Department of Geodesy and Geomatics Engineering, Technical Report No. 267, University of New Brunswick, Fredericton, New Brunswick, Canada, pp 232 .

Leandro RF, Santos MC, Langley RB (2011) Analyzing GNSS data in precise point positioning software. GPS Solut 15:1–13. doi: 10.1007/s10291-010-0173-9.

Leather A (2019) Intel Aims to Conquer 5G in 2019 With XMM 8160 Multi-Mode Single Chip. In: Forbes. https:// www.forbes.com/ sites/antonyleather/ 2019/02/26/intel- aims-to-conquer-5g-in-2019 -with-xmm-8160-multi-mode-single-chip/#3112c98223a4. Accessed 24 Apr 2019.

Li J, Yang Y, He H, Guo H (2016) An analytical study on the carrier-phase linear combinations for triple-frequency GNSS. J Geod. doi: 10.1007/s00190-016-0945-2.

Li J, Yang Y, Xu J, He H, Guo H (2013a) GNSS multi-carrier fast partial ambiguity resolution strategy tested with real BDS/GPS dual- and triple-frequency observations. GPS Solut 19:5–13. doi: 10.1007/s10291-013-0360-6

Li, X (2012) "Improving Real-time PPP Ambiguity Resolution with Ionospheric Characteristic Consideration," Proceedings of the 25th International Technical Meeting of the Satellite Division of The Institute of Navigation (ION GNSS 2012), Nashville, TN, September 2012, pp. 3027-3037.

Li X, Ge M, Zhang H, Wickert J (2013b) A method for improving uncalibrated phase delay estimation and ambiguity-fixing in real-time precise point positioning. J Geod 87:405–416. doi: 10.1007/s00190-013-0611-x.

Liu J (2013) BeiDou: China's rapidly emerging GNSS. Novatel's Thought Leadership Series, Inside GNSS, pp 30–31.

Liu T, Yuan Y, Zhang B, Wang N, Tan B, Chen Y (2017) Multi-GNSS precise point positioning (MGPPP) using raw observations. J Geod 91:253–268. doi: 10.1007/s00190-016-0960-3

Liu Z, Li Y, Guo J, Li F (2016) Influence of higher-order ionospheric delay correction on GPS precise orbit determination and precise positioning. Geod Geodyn 7:369–376. doi: 10.1016/j.geog.2016.06.005

Lou Y, Zheng F, Gu S, Wang C, Guo H, Feng Y (2016) Multi-GNSS precise point positioning with raw single-frequency and dual-frequency measurement models. GPS Solut 20:849–862. doi: 10.1007/s10291-015-0495-8

Lu C, Chen X, Liu G, Dick G, Wickert J, Jiang X, Zheng K, Schuh H (2017) Real-Time Tropospheric Delays Retrieved from Multi-GNSS Observations and IGS Real-Time Product Streams. Remote Sens 9:1317. doi: 10.3390/rs9121317

Lu, Yu, Cheng, Jingrong, Farrell, Jay A. (2005) "A New Method to Enhance GPS SNR and its Application in Fast Signal Acquisition," Proceedings of the 61st Annual Meeting of The Institute of Navigation (2005), Cambridge, MA, June 2005, pp. 535-542.

Lucas-Sabola, V., Seco-Granados, G., López-Salcedo, J.A., García-Molina, J.A., Crisci, M. (2017) "Efficiency Analysis of Cloud GNSS Signal Processing for IoT Applications," Proceedings of the 30th International Technical Meeting of the Satellite Division of The Institute of Navigation (ION GNSS+ 2017), Portland, Oregon, September 2017, pp. 3843-3852.

Ma X, Tang C, Wang X (2019) The evaluation of IRNSS/NavIC system's performance in its primary and secondary service areas–data quality, usability and single point positioning. Acta Geod Geophys 54:55–70

Mannucci A, Wilson B, Yuan D, Ho CH, Lindqwister UJ, Runge TF (1998) A global mapping technique for GPS-derived ionospheric total electron content measurements. Radio Sci 33:565–582

Markowitz M (2018) STMicroelectronics Launches World's First Multi-Band GNSS Receiver with Autonomous-Driving Precision and Automotive Safety Compliance. In: STMicroelectronics. https:// www.st.com/ content/st_com/en/ about/media-center/press-item.html/p4017.html#. Accessed 24 Apr 2018

Mervart L, Lukes Z, Rocken C, Iwabuchi T (2008) "Precise Point Positioning with Ambiguity Resolution in Real-Time," Proceedings of the 21st International Technical Meeting of the Satellite Division of The Institute of Navigation (ION GNSS 2008), Savannah, GA, September 2008, pp. 397-405.

Michelon, J., Bouchired, S (2003) "Integration of a SBAS-Based Positioning Architecture into a Satellite Digital Radio Broadcasting (S-DB) LBS Platform," Proceedings of the 16th International Technical Meeting of the Satellite Division of The Institute of Navigation (ION GPS/GNSS 2003), Portland, OR, September 2003, pp. 726-735.

Misra P, Enge P (2006) Global Positioning System: Signals, Measurements and Performance, 2nd edition. Ganga-Jamuna Press, Massachusetts, pp 561.

Mongredien C, Doyen J, Strom M, Ammann D (2016) Centimeter-level positioning for UAVs and other mass-market applications. In: Proceedings of the 29th International Technical Meeting of the Satellite Division of The Institute of Navigation (ION GNSS+ 2016). Portland, Oregon, pp 1441-1454.

Montenbruck O, Hauschild A, Steigenberger P, Hugentobler U, Teunissen P, Nakamura S (2012) Initial assessment of the COMPASS/BeiDou-2 regional navigation satellite system. GPS Solut 17:211–222. doi: 10.1007/s10291-012-0272-x

Montenbruck O, Hugentobler U, Dach R, Steigenberger P, Hauschild A (2011) Apparent Clock Variations of the Block IIF-1 (SVN62) GPS Satellite. GPS Solut 16:303–313. doi: 10.1007/s10291-011-0232-x

Montenbruck O, Steigenberger P, Prange L, Deng Z, Zhao Q, Perosanz F, Romero I, Noll C, Sturze A, Weber G, Schmid R, MacLeod K, Schaer S (2017) The Multi-GNSS Experiment (MGEX) of the International GNSS Service (IGS) – Achievements, prospects and challenges. Adv Space Res. doi: 10.1016/j.asr.2017.01.011

Murai Y (2014) Project Overview Quasi-Zenith Satellite System. In: Proceedings of the 27th International Technical Meeting of The Satellite Division of the Institute of Navigation (ION GNSS+ 2014). pp 8–12

Murfin T (2017) Big news from Broadcom: 30-cm positioning for consumers. In: GPS World. https:// www.gpsworld.com /big-news-from- broadcom -30-cm-positioning -for- consumers/. Accessed 24 Apr 2019

Nadarajah N, Khodabandeh A, Teunissen PJG (2015) Assessing the IRNSS L5-signal in combination with GPS, Galileo, and QZSS L5/E5a-signals for positioning and navigation. GPS Solut. doi: 10.1007/s10291-015-0450-8

Nadarajah N, Khodabandeh A, Wang K, Choudhury M, Teunissen PJG (2018) Multi-GNSS PPP-RTK: From Large- to Small-Scale Networks. Sensors 18: 1078. https:// doi.org/ 10.3390/ s18041078

NASA (2017) Navstar 2A-01. In: NASA Space Sci. Data Coord. Arch. https://nssdc.gsfc.nasa.gov/nmc/spacecraftDisplay.do?id=1990-103A. Accessed 6 Mar 2017

National Coordination Office for Space-Based Positioning, Navigation, and Timing (2019) Official U.S. government information about the Global Positioning System (GPS) and related topics. In: Space Segm. https:// www.gps.gov/systems/ gps/space/. Accessed 22 Jul 2019

Neri A, Salvatori P, Stallo C, Coluccia A (2018) "A Multi-sensor Autonomous Integrity Monitoring Approach for Railway and Driver-less Cars," Proceedings of the 31st International Technical Meeting of the Satellite Division of The Institute of Navigation (ION GNSS+ 2018), Miami, Florida, September 2018, pp. 1605-1621.

Newcomb D (2013) From hand-cranked maps to the cloud: Charting the history of in-car navigation. In: Wired. https://www.wired.com/2013/04/history-in-car-navigation/. Accessed 27 Apr 2019

Nielsen J, Dehghanian V (2014) "Accurate Positioning of Autonomous Vehicles in Adverse Visibility Conditions," Proceedings of the 27th International Technical Meeting of the Satellite Division of The Institute of Navigation (ION GNSS+ 2014), Tampa, Florida, September 2014, pp. 1931-1940.

Nottingham Scientific Ltd (2018) NSL launches a new free Android app as part of FLAMINGO – Discover rinexON. In: Flamingo GNSS. https:// www. flamingognss.com /rinexon. Accessed 27 Apr 2019

Odijk D (2003) Ionosphere-free phase combinations for modernized GPS. Journal of Surveying Engineering Volume 129, pp 165–173.

Odijk D (2002) Fast precise GPS positioning in the presence of ionospheric delays. PhD Thesis, Delft University of Technology, Netherlands Geodetic Commission, pp 240.

Odijk D, Teunissen P, Zhang B (2011) PPP-RTK platform performance based on single-frequency GPS data. In: 32nd Asian Conference on Remote Sensing 2011, ACRS 2011. pp 2113–2118.

Odijk D, Zhang B, Khodabandeh A, Odolinski R, Teunissen P (2016) On the estimability of parameters in undifferenced, uncombined GNSS network and PPP-RTK user models by means of S -system theory. J Geod 90:15–44. doi: 10.1007/s00190-015-0854-9.

Odolinski R, Teunissen PJG (2017) Low-cost, 4-system, precise GNSS positioning: a GPS, Galileo, BDS and QZSS ionosphere-weighted RTK analysis. Meas Sci Technol 28:125801. doi: 10.1088/1361-6501/aa92eb

Odolinski R, Teunissen PJG (2019) An assessment of smartphone and low-cost multi-GNSS single-frequency RTK positioning for low, medium and high ionospheric disturbance periods. J Geod 93:701–722. doi: 10.1007/s00190-018-1192-5

Øvstedal O (2002) Absolute positioning with single-frequency GPS receivers. GPS Solutions, Volume 5, pp 33–44.

Pathak V, Thornwall S, Krier M, Rowson S, Poilasne G, Desclos L (2003) Mobile handset system performance comparison of a linearly polarized GPS internal antenna with a circularly polarized antenna. In: IEEE Antennas and Propagation Society International Symposium. Digest. Held in conjunction

with: USNC/CNC/URSI North American Radio Sci. Meeting (Cat. No.03CH37450). IEEE, Columbus, OH, USA, pp 666–669

Pengfei C, Wei L, Jinzhong B, Li W, Wen H, Yanhui C, Hua W (2011) Performance of Precise Point Positioning (PPP) Based on Uncombined Dual-Frequency GPS Observables. Surv Rev 43:343–350. https: // doi.org /10.1179/ 003962611 X13055561708588

Pesyna KM, Heath RW, Humphreys TE (2014) Centimeter positioning with a smartphone-quality GNSS antenna. In: Proceedings of the ION GNSS+ Meeting. Tampa, FL, pp 1568–1577

Ray JK, Cannon ME, Fenton P (2001) GPS code and carrier multipath mitigation using a multiantenna system. Aerosp Electron Syst IEEE Trans On 37:183–195

Riddle A (2013) Are smartphones essential? (review of "essentials of mobile handset design"; naha, a. and whale, p.; 2012) [book/software reviews]. IEEE Microw Mag 14:124–126. https://doi.org/10.1109/MMM.2013.2270094

Riley S, Landau H, Gomez V, Mishukova N, Lentz W, Clare A (2018) Positioning with Android:GNSS observables. GPS World 29:14

Rispoli, F, Enge P, Neri A, Senesi F, Ciaffi M, Razzano E (2018) "GNSS for Rail Automation & Driverless Cars: A Give and Take Paradigm," Proceedings of the 31st International Technical Meeting of the Satellite Division of The Institute of Navigation (ION GNSS+ 2018), Miami, Florida, September 2018, pp. 1468-1482.

Rizos, C., Montenbruck, O., Weber, R., Weber, G., Neilan, R., Hugentobler, U. (2013) "The IGS MGEX Experiment as a Milestone for a Comprehensive Multi-GNSS Service," Proceedings of the ION 2013 Pacific PNT Meeting, Honolulu, Hawaii, April 2013, pp. 289-295.

Robustelli U, Baiocchi V, Pugliano G (2019) Assessment of Dual Frequency GNSS Observations from a Xiaomi Mi 8 Android Smartphone and Positioning Performance Analysis. Electronics 8:91. doi: 10.3390/electronics8010091

Rovira-Garcia, A., Juan, J. M., Sanz, J. (2014) "A Real-time World-wide Ionospheric Model for Single and Multi-frequency Precise Navigation," Proceedings of the 27th International Technical Meeting of the Satellite Division of The Institute of Navigation (ION GNSS+ 2014), Tampa, Florida, September 2014, pp. 2533-2543.

Schaer S (1999) Mapping and predicting the Earth's ionosphere using the Global Positioning System. Institut für Geodäsie und Photogrammetrie, Eidg. Technische Hochschule Zürich, Geod.-Geophys. Arb. Schweiz, Vol. 59.

Schaer S, Gurtner W, Feltens J (1998) IONEX: The ionosphere map exchange format version 1. In: Proceedings of the IGS AC Workshop, Darmstadt, Germany, pp 1-12.

Schönemann E, Becker M, Springer T (2011) A new approach for GNSS analysis in a multi-GNSS and multi-signal environment. J Geod Sci 1:204–214.

Schuler T (2001) On ground-based GPS tropospheric delay estimation. Dr Thesis Stud Geodsie Geoinformation Univ Buundeswehr Munchen 73, pp 364.

Seepersad G (2012) Reduction of initial convergence period in GPS PPP data processing. MSc Thesis, York University, Canada, pp 153.

Seepersad G, Aggrey J, Bisnath S (2017) Do We Need Ambiguity Resolution in Multi-GNSS PPP for Accuracy or Integrity? In: Proceedings of the 30th International Technical Meeting of The Satellite Division of the Institute of Navigation (ION GNSS+ 2017). pp 2204–2218.

Seepersad G, Bisnath S (2012) "Reduction of Precise Point Positioning Convergence Period," Proceedings of the 25th International Technical Meeting of the Satellite Division of The Institute of Navigation (ION GNSS 2012), Nashville, TN, September 2012, pp. 3742-3752.

Seepersad G, Bisnath S (2014a) Reduction of PPP convergence period through pseudorange multipath and noise mitigation. GPS Solut 19:369–379. doi: 10.1007/s10291-014-0395-3.

Seepersad G, Bisnath S (2014b) Challenges in Assessing PPP Performance. Journal of Applied Geodesy Volume 8, pp 205–222.

Seepersad GG (2018) Improving Reliability and Assessing Performance of Global Navigation Satellite System Precise Point Positioning Ambiguity Resolution, York university, Toronto, Canada, PhD Dissertation, pp 185.

Seynat C, Kealy A, Zhang K (2004) A Performance Analysis of Future Global Navigation Satellite Systems. J Glob Position Syst 3:232–241. doi: 10.5081/jgps.3.1.232.

Shi C, Gu S, Lou Y, Ge M (2012) An improved approach to model ionospheric delays for single-frequency Precise Point Positioning. Adv Space Res 49:1698–1708. doi: 10.1016/j.asr.2012.03.016.

Shuangqing L (1996) Carrier Rockets of the World: Tsyklon (Russia/CIS). National Air Intelligence Center Wright-Patterson AFB OH, pp 12.

Stansell TA (1978) The Transit: Navigation Satellite System: Status, Theory, Performance, Applications. Magnavox, pp 83.

STMicroelectronics (2019) STMicroelectronics Introduces Safe, Real-Time Microcontrollers for Next-Generation Automotive Domain Architectures. In: Glob. News Wire. https:// www.globenewswire.com/ news-release/ 2019/02/21/ 1739396/0/ en/STMicroelectronics-Introduces-Safe-Real-Time-Microcontrollers-for-Next-Generation-Automotive-Domain-Architectures.html. Accessed 6 Jun 2019

Sullivan M (2012) A brief history of GPS. In: PCWorld. https:// www.pcworld.com/ article/2000276/a-brief-history-of-gps.html. Accessed 23 Apr 2019

Sun F, Liu S, Zhu X, Men B (2012) Research and progress of Beidou satellite navigation system. Sci China Inf Sci 55:2899–2907. doi: 10.1007/s11432-012-4724-2

Sunkevic M (2017) Using GNSS Raw Measurements on Android Devices – Tutorial part I. Eur GNSS Agency 99. doi: 10.2878/449581.

Synopsys (2019) Synopsys establishes center of excellence with STMicroelectronics to speed development of automotive electronic systems. In: Automot. World. https://www.automotiveworld.com/news-releases/synopsys-establishes-center-of-excellence-with-stmicroelectronics-to-speed-development-of-automotive-electronic-systems/. Accessed 6 Jun 2019

Tang W, Deng C, Shi C, Liu J (2014) Triple-frequency carrier ambiguity resolution for Beidou navigation satellite system. GPS Solut 18:335–344. doi: 10.1007/s10291-013-0333-9

Tegedor J, Øvstedal O (2014) Triple carrier precise point positioning (PPP) using GPS L5. Surv Rev 46:288–297. doi: 10.1179/1752270613Y.0000000076

Tegedor J, Øvstedal O, Vigen E (2014) Precise orbit determination and point positioning using GPS, Glonass, Galileo and BeiDou. J Geod Sci 4:. doi: 10.2478/jogs-2014-0008.

Teunissen P, Khodabandeh A (2015) Review and principles of PPP-RTK methods. J Geod Volume 89; pp 217–240.

Teunissen PJ, Odijk D, Zhang B (2010) PPP-RTK: Results of CORS network-based PPP with integer ambiguity resolution. J Aeronaut Astronaut Aviat Ser A 42:223–230.

Tijero, ED, Pons EC, Calle JDC, Fernández LM, Madrid PFN, Varo CM, Sáenz MA (2017) "Advanced GNSS Algorithms for Safe Autonomous Vehicles," Proceedings of the 30th International Technical Meeting of the Satellite Division of The Institute of Navigation (ION GNSS+ 2017), Portland, Oregon, September 2017, pp. 655-664.

Tobias G, Garcia C, Mozo A, Navarro P (2011) Filling in the gaps of RTK with Regional PPP. In: Proceedings of the 24th International Technical Meeting of The Satellite Division of the Institute of Navigation (ION GNSS 2011), Portland, OR. pp 2193–2201.

Tomatis A, Cataldi P, Pau G, Mulassano P, Dovis F (2008) Cooperative LBS for Secure Transport System. Proceeding of ION GNSS 2008, Savannah, Georgia (USA), pp 6.

Tu R, Zhang R, Lu C, Zhang P, Liu J, Lu X (2017) A Unified Model for BDS Wide Area and Local Area Augmentation Positioning Based on Raw Observations. Sensors 17:507. doi: 10.3390/s17030507

Ublox (2011) Meizu high-definition smartphone for China includes u-blox GPS. In: Ublox Positioing Technol. https://www.u-blox.com/en/press-release/meizu-high-definition-smartphone-china-includes-u-blox-gps. Accessed 6 Jun 2019

Ublox (2013) Longsung smartphones integrate u-blox positioning technology. In: Ublox Positioing Technol. https:// www.u-blox.com/ en/press-release/ longsung-smartphones- integrate-u-blox-positioning-technology. Accessed 6 Jun 2019

U-blox (2019) Product summary of ZED-F9P: u-blox F9 high precision GNSS module,https://www.u-blox.com/sites/default/files/ZED-F9P_Product Summary_%28UBX-17005151%29.pdf, pp 2.

Urlichich, Y., Subbotin, V., Stupak, G., Dvorkin, V., Povaliaev, A., Karutin, S., "GLONASS Developing Strategy," Proceedings of the 23rd International Technical Meeting of the Satellite Division of The Institute of Navigation (ION GNSS 2010), Portland, OR, September 2010, pp. 1566-1571.

Urlichich Y, Subbotin V, Stupak G, Dvorkin V, Povalyaev A, Karutin S, Bakitko R (2011) GLONASS modernization. GPS World 22:34–39

Urquhart, L. (2009). An Analysis of Multi-Frequency Carrier Phase Linear Combinations for GNSS. Senior technical report, Department of Geodesy and Geomatics Engineering Technical Report No. 263, University of New Brunswick, Fredericton, New Brunswick, Canada, pp 71.

U.S. Coast Guard Navigation Center (2015) Notice Advisory to GPS Users. In: Navig. Cent. http:// www.navcen.uscg.gov/ ?Do=gps Show Nanu&num=2014090. Accessed 15 Mar 2015.

US DoD (2001) Global positioning system standard positioning service performance standard. Assist Secr Def Command Control Communication Intelligence, 4th edition, pp 160.

Varela MR, Patrício AR, Anderson K, Broderick AC, DeBell L, Hawkes LA, Tilley D, Snape RTE, Westoby MJ, Godley BJ (2019) Assessing climate change associated sea-level rise impacts on sea turtle nesting beaches using drones, photogrammetry and a novel GPS system. Glob Change Biol 25:753–762.

Viken A (2010) The history of Personal Digital Assistants 1980 – 2000. In: Agile Mobil. https:// web.archive.org/ web/ 20131030153659/ http:// agile mobility.net/ 2009/04/ the- history -of- personal- digital- assistants1/. Accessed 23 Apr 2019.

Vollath U, Birnbach S, Landau L, Fraile-Ordonez JM, Marti-Neira M (1999) Analysis of Three-Carrier Ambiguity Resolution Technique for Precise Relative Positioning in GNSS-2. Navigation 46:13–23.

Vydhyanathan, A, Braasch MS., de Haag MU (2007) "Multi-Sensor Integration for Autonomous Vehicle Relative Navigation," Proceedings of the 20th International Technical Meeting of the Satellite Division of The Institute of Navigation (ION GNSS 2007), Fort Worth, TX, September 2007, pp. 587-595.

Wang B (2018) High end smartphones later in 2018 should use Broadcom chip enables centimeter accurate GPS. In: Big Future. https:// www.nextbigfuture.com/

2018/04/high-end-smartphones-later-in-2018-should-use-broadcom-chip-enables-centimeter-accurate-gps.html. Accessed 6 Jun 2019.

Wang K, Rothacher M (2013) Ambiguity resolution for triple-frequency geometry-free and ionosphere-free combination tested with real data. J Geod 87:539–553. doi: 10.1007/s00190-013-0630-7.

Wang W, Chi T, Wu Q, Cheng W, Deng Z, Zhang F, Lv C, Song L (2015) On Beidou's Short Message Service-Based Data Transmission Solution. J Comput Theor Nanosci 12:2556–2565.

Wells, D. E., N. Beck, D. Delikaraoglou, A. Kleusberg, E. J. Krakiwsky, G. Lachapelle, R. B. Langley, M. Nakiboglu, K. P. Schwarz, J. M. Tranquilla, and P. Vanicek (1986). Guide to GPS Positioning. Department of Geodesy and Geomatics Engineering Lecture Note No. 58, University of New Bnmswick, Fredericton, New Brunswick, Canada, pp 291.

Wienia RJ (2008) Use of global ionospheric maps for precise point positioning. MSc Thesis, TU Delft, Aerospace Engineering, Mathematical Geodesy and Positioning, pp 146.

Xie X, Geng T, Zhao Q, Liu J, Wang B (2017) Performance of BDS-3: Measurement Quality Analysis, Precise Orbit and Clock Determination. Sensors 17:1233. doi: 10.3390/s17061233.

Xu Y, Wu C, Li L, Yan L, Liu M, Wang S (2018) GPS/BDS Medium/Long-Range RTK Constrained with Tropospheric Delay Parameters from NWP Model. Remote Sens 10:1113. doi: 10.3390/rs10071113

Yao Y, Zhang R, Song W, Shi C, Lou Y (2013) An improved approach to model regional ionosphere and accelerate convergence for precise point positioning. Adv Space Res 52:1406–1415. doi: 10.1016/j.asr.2013.07.020

Yoon D, Kee C, Seo J, Park B (2016) Position accuracy improvement by implementing the DGNSS-CP algorithm in smartphones. Sensors 16:910

Zak A (2019) Deployment of the GLONASS constellation. In: Russ. Space Web. http://www.russianspaceweb.com/glonass_deployment.html. Accessed 22 Jul 2019

Zavoli W, Bloch G (1990) Etak Navigator Modification. U.S. Army Corps of Engineers, California, https://apps.dtic.mil/dtic/tr/fulltext/u2/a238937.pdf, pp 238.

Zhang B, Teunissen PJG, Odijk D (2011) A Novel Un-differenced PPP-RTK Concept. J Navig 64:S180–S191. https://doi.org/10.1017/S0373463311000361

Zhang H, Gao Z, Ge M, Niu X, Huang L, Tu R, Li X (2013) On the Convergence of Ionospheric Constrained Precise Point Positioning (IC-PPP) Based on Undifferential Uncombined Raw GNSS Observations. Sensors 13:15708 – 15725. https:// doi.org/ 10.3390/ s131115708

Zhang X, Li P (2016) Benefits of the third frequency signal on cycle slip correction. GPS Solut 20:451–460

Zhang X, Tao X, Zhu F, Shi X, Wang F (2018) Quality assessment of GNSS observations from an Android N smartphone and positioning performance analysis using time-differenced filtering approach. GPS Solut 22:. https://doi.org/10.1007/s10291-018-0736-8

Zhang, Y., Lee, S., Chen, C (2008) "Achieving 30 cm Autonomous Positioning Accuracy with Nexteq Single-Frequency GPS Receivers," Proceedings of the 21st International Technical Meeting of the Satellite Division of The Institute of Navigation (ION GNSS 2008), Savannah, GA, September 2008, pp. 1210-1216.

Zumberge JF, Heflin MB, Jefferson DC, Watkins MM, Webb FH (1997) Precise point positioning for the efficient and robust analysis of GPS data from large networks. J Geophys Res Solid Earth 1978–2012 102:5005–5017